

UNIVERSITÉ DE NANTES
FACULTÉ DES SCIENCES ET DES TECHNIQUES

ÉCOLE DOCTORALE 3MPL

Année 2011

N° attribué par la bibliothèque



Transport électronique aux différentes échelles de matériaux composites C-LiFePO₄/Carboxymethyl cellulose utilisés dans les batteries au lithium.

THÈSE DE DOCTORAT
Discipline : Science des matériaux
Spécialité : Chimie du solide

*Présentée
et soutenue publiquement par*

KALID AHMED SEID

Le 24 octobre 2011, devant le jury ci-dessous

Rapporteurs	M. Sylvain FRANGER, Maître de conférences • ICCMO-Université d'Orsay, Paris M. Renaud BOUCHET, Maître de conférences • Université d'Aix-Marseille I, II et III, M ^{me} Claire HEROLD, Directeur de recherche • LCSM, Université Henri Poincaré, Nancy
Examinateurs	M. Jean-Claude BADOT, Ingénieur de Recherche • Chimie-ParisTech, Paris M. Olivier CHAUVET, Professeur • IMN, Université de Nantes, Nantes M. Dominique GUYOMARD, Directeur de recherche • IMN, Université de Nantes, Nantes M. Bernard LESTRIEZ, Maître de conférences • IMN, Université de Nantes, Nantes M. Maxime BLANGERO, Docteur Ingénieur • Umicore Korea LTD

Directeur de thèse : M. Dominique GUYOMARD

Co-directeur de thèse : M. Jean-Claude BADOT

Encadrant : M. Bernard LESTRIEZ

Co-encadrant : M. Olivier DUBRUNFAUT

Acknowledgments

During this PHD thesis I have worked with many colleagues for whom I have great regard, and I wish to extend my warmest thanks to those who have helped me with my work at the Institut des Materiaux Jean Rouxel university of Nantes, École Nationale Supérieure de Chimie de Paris (Chimie Paris-Tech) at UPMC, Laboratoire de Génie Electrique de Paris (LGEP) under Ecole Supérieure D'électricité and of course Umicore Cobalt and Speciality Materials Belgium.

I would like to express my deep and sincere gratitude to my supervisor, Bernard Lestriez (PhD), IMN, for his consistent intellectual input, support, guidance and encouragement through out the span of the thesis. His belief in me was an extra drive to go forward during challenging times in my work. His exemplary hard work, vision and ability for multi tasking have always been a great motivation for me. Thank you.

I would also like to express my sincere gratitude to my supervisor, Jean-Claude Badot (Phd), Chimie Paris-tech, for his invaluable scientific contribution, humour and kindness through the PHD. I learned most of the things I know about the principal technique used from him. His systematic thinking and vast experience has been a valuable asset for the success of my work. thank you.

The same goes to Olivier Dubrunfaut (Phd); for his professional input to this work specially in the instrumentation Aspect. He was very patient during the difficult period were I had to learn a new technique; he has always been willing to help and explain things repeatedly.

I am also deeply grateful to my thesis director Dominique Guyomard (PHD), for his contribution, wisdom and guidance. He has been kind, understanding and a good leader.

I am also grateful to Stephane Levasseur , Maxime Blangero and Randy de Palma form Umicore for supplying the materials needed , financial support and participating in our meeting during which they often enriched our work with their suggestions.

My heartfelt gratitude goes to the whole ST2E group at IMN with whom I spend a great three years. Because of you I have grown up in many ways during those years despite the challenges. Special thanks goes to my fellow Master trainees, PHD students and Post docs of ST2E. To mention few ,Nathalie Delpuech, Pierre-Emanuel Delannoy, Audrey bouvree,

Magali Gauthier, Margaud Lecuyer, Lenaic Madec, Marine cassinier, Driss mazouzi, Jean-batiste Ducros, florian dianaux, Mohamed, Angelique jarry, yassine oumelal, Nahn Nguyen, Philippe Mongondry, Azmach Geremew, Zongli wang, Theresa Jardiel and many more. You all have been great colleagues and office mates. You have been instrumental in creating a relaxed yet professional working environment. If I have to write about each one of you it is going to take few dozen pages so I will summarize it in a sentence, I do not have enough words to thank you all. Please do know that I do recognize and appreciate you all.

Further more, all the permanent staff that provided me with valuable suggestions during my work and group meeting are appreciated. I am sure I forgot many individuals and I apologize in advance as I have written this acknowledgment in a hurry. Thank you all.

Alexander Garreau, Elodie Creton, Cedric Michelet, Victor le Nadar, Jean-mark Lorry, Karim Makaoui, Philippe Wagner, Frederic Reisdorffer, Abedlaziz el Mel, Marie Buffiere, khadija, Tilak das and many more deserve a special credit for all the good times we have spent together, Wednesday night football session, Friday night out, relaxing coffee breaks, card games were all helpful during a difficult “life” of a PHD student and I would not have made it without you guys, thank you all.

Arkadiusz Karpiniski and Zulfikar Ali Umrani deserve a special mention for those special coffee breaks, long discussions, adventures and legendary weekends. We have made a lot of life time history from the beginning to the end. Thank you so much.

Eric Gautron and Nicolas Gautier from CMC-TEM deserve a mention as well, not only for being always willing to help but also for their humour which made it easier to communicate and work with them.

I would also like to thank the administration and support staff of the IMN without whom the institute would be crippled. A Special mention goes to Catherine Rochas, Guylaine Nicolas, and Mauricette Chabot for their will to go the extra distance to help me in the administrative processes through out my period of stay.

Finally I would not finish without a special gratitude to my parents, Ahmed Seid and Tiruwork Aragaw, for raising me with values, good will and confidence not to mention their unreserved support all the way. I would not have been the person I am today without them. In

addition I would like to thank my Brother, Anwar Ahmed and my Sisters, Semira Ahmed, Hanan Ahmed, and Sitra Ahmed for everything. You guys are wonderful.

Once again, my sincere apology goes to those I failed to mention here. Thank you all anyway.

October 24th 2011, Nantes, France

Section1: Résumé Français

Table des matières

Chapitre 1.....	1
1. La Spectroscopie Diélectrique Large bande (BDS).....	1
1.1. Présentation	1
1.2. Aspects théoriques et phénoménologiques de la technique.	1
1.3. Aspects expérimentaux	9
2. Références bibliographiques.....	13
Chapitre 2.....	14
1. Introduction	14
2. Résultats et discussion.....	17
2.1. Morphologie et analyse des échantillons	17
2.2. Les mesures électriques: identification des différentes relaxations et leurs attributions (les mécanismes de conductivité électronique).....	21
2.3. Détermination de la conductivité réelle aux différentes échelles de loi C-LiFePO ₄	36
3. Conclusions	37
4. Partie expérimentale	38
5. Références bibliographiques.....	40

Section 2: English

Table of contents

General Introduction	43
Chapter 1: Background.....	48
1. Introduction	48
2. The Broadband Dielectric Spectroscopy (BDS).....	48
2.1. Introduction	48

2.2. Theoretical and phenomenological aspect of the technique	49
2.3. Experimental aspects	58
2.4. Previous works performed using the BDS	64
3. Conduction mechanisms in carbon (hopping)	66
5. State of the art about the understanding of the electronic properties of composite electrodes for lithium batteries.....	67
6. Conclusion.....	70

Chapter 2: Binary Systems..... 71

1. Introduction	71
2. Results and discussion.....	73
2.1. Morphology and analysis of the LiFePO ₄ materials	73
2.2. The Sample preparation for BDS measurements	80
2.3. Electrical measurements: identification of the different relaxations and their attributions (the electronic conductivity mechanisms).	83
2.4. Determination of the true conductivities at the different scales of C-LiFePO ₄	97
2.5. Calculation of the bulk permittivity of LiFePO ₄	100
3. Conclusions	101

Chapter 3: Ternary systems 103

1. Introduction	103
2. Results and discussion.....	105
2.1. Sample preparation and analysis of their morphology.....	106
2.2. Electrical measurements.....	110
2.3. Analysis of the effect of ball-milling in water	114
2.4. Analysis of the effect of the binder on the bulk properties (ε_{∞} and σ_{sp2e})	

2.5. Analysis of the effect of the binder on the coating properties and cluster conductivity	115
2.6. Analysis of the binder effect on the inter-clusters contacts and samples conductivities.....	124
2.7. Analysis of the binder effect on the interface sample/current collector	
130	
2.8. The true conductivities at the different scales of the C-LiFePO ₄ /CMC composites	132
3. Conclusion	135
General Conclusion and perspectives.....	136
Appendices	140
Appendix 1: Material characterizations.....	140
Appendix 2: Effect of the sample thickness on the reproducibility and measured parameters	143
Appendix 3: DC conductivity measurements as a function of the temperature using a four probes technique.....	146

Chapitre 1

1. La Spectroscopie Diélectrique Large bande (BDS)

1.1. Présentation

La spectroscopie diélectrique est l'étude de l'interaction d'un matériau avec un champ électrique variable dans le temps. La réponse ou polarisation, qui en résulte, est exprimée par la permittivité et la conductivité complexes dépendantes de la fréquence. Cette polarisation caractérise l'amplitude et l'échelle de temps des fluctuations de densité de charge à l'intérieur du matériau. Pour des fréquences inférieures à 10^{11} Hz, de telles fluctuations proviennent de la réorientation de dipôles permanents, de mouvements locaux de charges liées et de la présence éventuelle d'interfaces internes (joints de grains, interfaces,...) bloquant quasiment les charges dans les matériaux polycristallins. Ces phénomènes sont alors décrits par des relaxations diélectriques dont les échelles de temps correspondent aux temps de relaxation.

Debye a été le premier à élaborer une théorie sur les moments dipolaires des molécules. Son premier mémoire, paru en 1911, a été suivi par beaucoup d'autres jusque dans les années 1950. Cette théorie phénoménologique, à la base des conceptions de diélectriques et de la mesure des moments dipolaires, va devenir un puissant moyen de détermination des structures moléculaires. En 1929, P. Debye a expliqué les valeurs importantes de la permittivité statique dans certains liquides (eau, alcool,..) en supposant que les molécules possèdent des moments dipolaires permanents susceptibles de s'écartier de leur orientation d'équilibre, leur retour vers celle-ci étant caractérisé par un temps de relaxation τ .

2.2. Aspects théoriques et phénoménologiques de la technique.

Lorsqu'un champ électrique statique est appliqué à un matériau conducteur non magnétique, il crée en son sein une densité de courant électrique et/ou une polarisation. En notant χ la susceptibilité électrique du milieu étudié, et ϵ , la permittivité relative du milieu, la polarisation est directement reliée au champ électrique par la relation :

$$\vec{P} = \epsilon_0 \chi \vec{E} = \epsilon_0 (\epsilon - 1) \vec{E} \quad 1.1$$

Or, le vecteur déplacement électrique s'écrit :

$$\vec{D} = \epsilon_0 \vec{E} + \vec{P} \quad 1.2$$

Ainsi, le vecteur déplacement électrique est relié au champ électrique par la relation :

$$\vec{D} = \epsilon_0 \epsilon \vec{E} \quad 1.3$$

La densité de courant \vec{J} est reliée au champ électrique via la conductivité statique du milieu σ_{dc} par la loi d'Ohm :

$$\vec{J} = \sigma_{dc} \vec{E} \quad 1.4$$

Si le champ électrique est variable avec le temps, la densité de courant et le vecteur déplacement électrique sont reliés via la loi de Maxwell-Ampère :

$$\vec{J}_D = \frac{\partial \vec{D}}{\partial t} \quad 1.5$$

Dans le cadre d'un régime harmonique et d'un matériau non-magnétique, nous utiliserons des grandeurs complexes telles que :

- la permittivité complexe $\varepsilon(\omega) = \varepsilon' - i\varepsilon''$ 1.6

- la conductivité complexe $\sigma(\omega) = \sigma' + i\sigma''$ 1.7

La partie imaginaire ε'' de la permittivité est également appelée « pertes diélectriques ». Quant aux relations précédentes, elles deviennent :

- relation de Maxwell-Ampère : $\vec{J}_D = i\omega \vec{D}$ 1.8

- loi d'Ohm : $\vec{J}_D = \sigma(\omega) \vec{E}$ 1.9

- déplacement électrique : $\vec{D} = \varepsilon_0 \varepsilon(\omega) \vec{E}$ 1.10

L'utilisation de la relation de Maxwell-Ampère avec les deux autres équations conduit à :

$$\sigma(\omega) = i\omega \varepsilon_0 \varepsilon(\omega)$$

Pour une fréquence tendant vers 0, la conductivité se stabilise à une valeur de σ_{dc} lorsque le matériau est conducteur.

En diminuant la fréquence, il existe quatre types principaux de polarisation dans un solide : la polarisation électronique, la polarisation ionique, la polarisation d'orientation et la polarisation interfaciale. La polarisation électronique est due à des contributions électroniques telles que les transitions interbandes dans les semi-conducteurs et la déformation des nuages électroniques présents autour des noyaux. Les fréquences typiques de ces phénomènes résonants sont situées dans le domaine UV-Visible. Puis à une échelle plus grande, des oscillations de réseau dues aux phonons optiques, se traduisent par des résonances dans le domaine infrarouge IR.

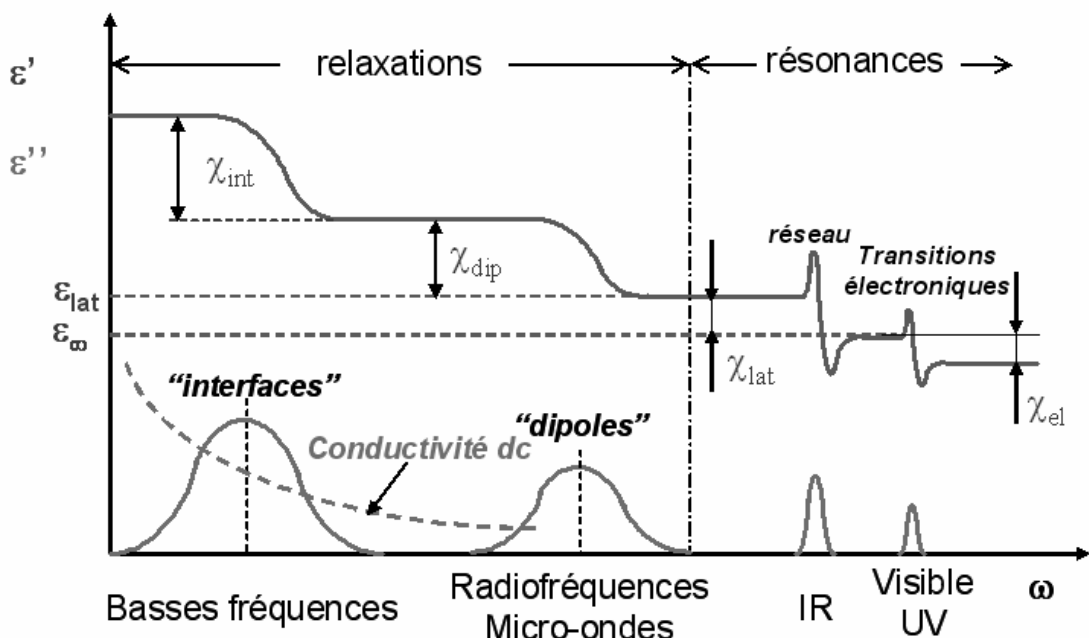


Figure 1. Evolution de la permittivité réelle et des pertes diélectriques en fonction de la fréquence.

A l'échelle moléculaire et interatomique, la polarisation d'orientation est due à des rotations de dipôles dans les liquides (par exemple, rotation de molécules polaires) ou à des mouvements locaux de charges (par exemple, sauts de charges sur quelques Angströms) dans le domaine des radiofréquences et des micro-ondes. Ces phénomènes sont visibles en spectroscopie diélectrique. Enfin, sur des distances plus grandes, le matériau peut présenter des polarisations interfaciales. Par interfaces, on peut désigner les joints de grains ou de façon plus générale, la zone de jonction entre grains, par définition, monocristallins. Si les grains sont assemblés en agrégats (ou clusters), une interface différente des joints de grains existe

entre agrégats. Enfin, une interface existe entre la pastille et les électrodes de contact utilisées pour réaliser la mesure. Ces types de polarisation sont visibles en basses fréquences et accessibles en spectroscopie diélectrique pour peu que l'appareil utilisé puisse descendre assez bas en fréquence. Les fréquences caractéristiques de ces différents phénomènes observables en spectroscopie diélectriques sont classables en fonction de l'échelle caractéristique à laquelle on les regarde. Plus la taille caractéristique est grande et plus la fréquence caractéristique est petite (Fig 2).

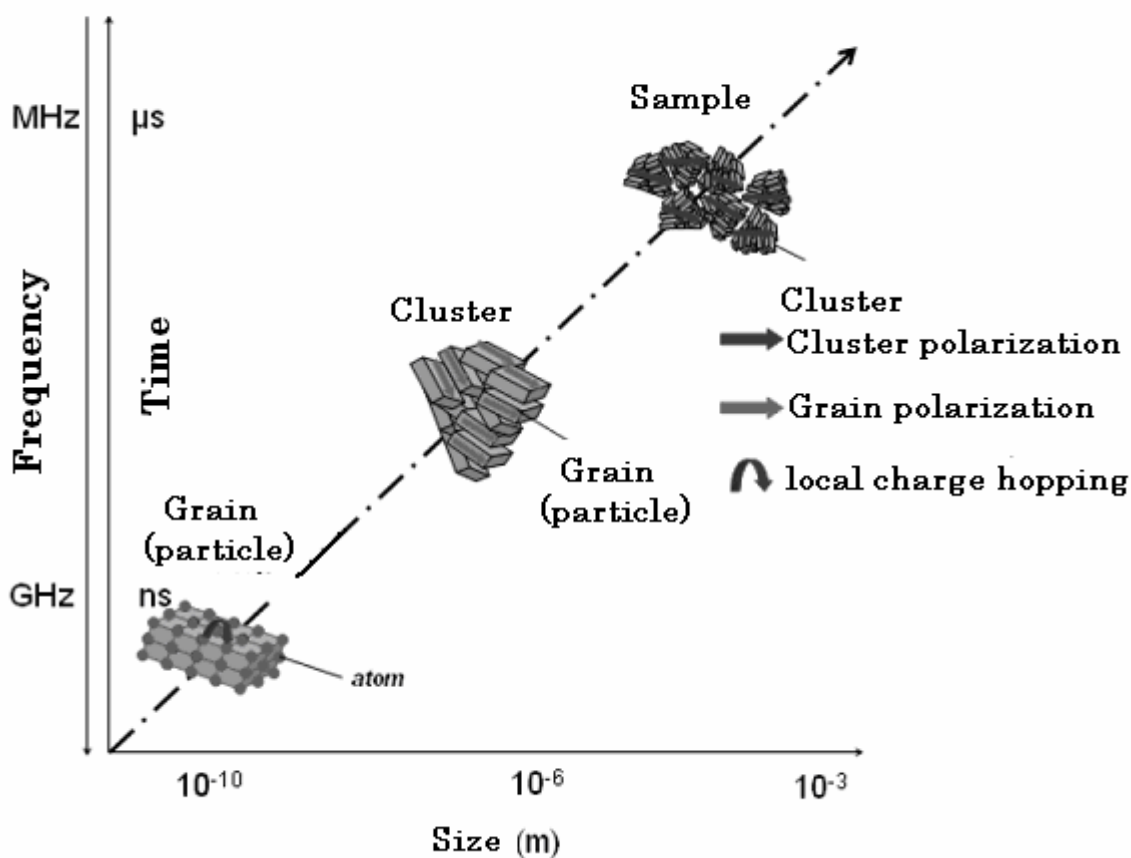


Figure 2. Analyse multi-échelle de la polarisation électrique dans un matériau conducteur [1].

Cette observation sera utilisée directement pour la répartition des différents assouplissements ??? en raison principalement d'électrons dans C-LiFePO₄. Ces phénomènes

sont modélisables de façon générale à l'aide de la fonction de relaxation empirique de Cole-Cole [2] :

$$\varepsilon(\omega) = \varepsilon_{HF} + \frac{\varepsilon_{LF} - \varepsilon_{HF}}{1 + (i\omega\tau)^{1-\alpha}} \quad 1.11$$

où τ est le temps de relaxation, la fréquence de relaxation étant $v_r = (2\pi\tau)^{-1}$. α est un paramètre compris entre 0 et 1 et signifie l'existence d'une distribution de temps (ou fréquences) de relaxation centrée en τ (ou en v_r). Lorsque $\alpha = 0$, nous avons la loi de Debye pour laquelle le temps (fréquence) de relaxation est unique. ε_{BF} et ε_{HF} sont les permittivités limites de la relaxation lorsqu'on a respectivement $\omega\tau \ll 1$ et $\omega\tau \gg 1$. L'incrément de permittivité $\Delta\varepsilon$ conséquent à une relaxation est égal à $\varepsilon_{HF} - \varepsilon_{BF}$. Cette loi de Cole-Cole se matérialise dans le plan de Nyquist par un demi-cercle coupant l'axe des abscisses en ε_{HF} et

en ε_{BF} et centré au point de coordonnées $\left[\frac{\varepsilon_{HF} + \varepsilon_{BF}}{2}; -\frac{\Delta\varepsilon}{2} \tan\left((1-\alpha)\frac{\pi}{2}\right) \right]$. 1.12

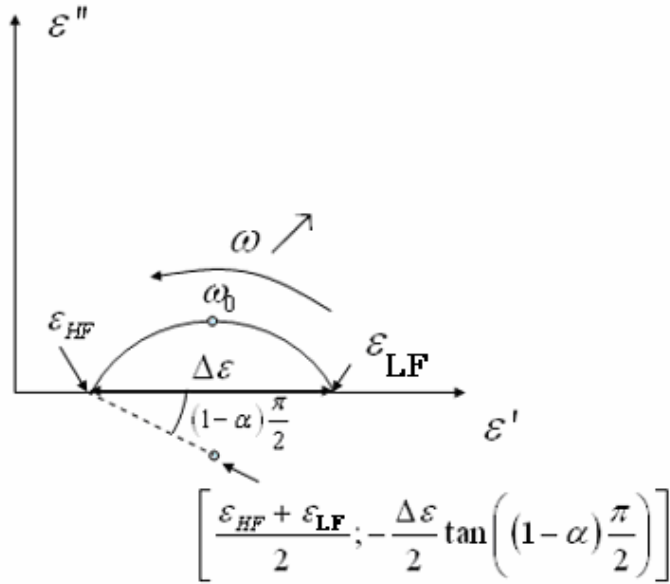


Figure 3. Diagramme de Nyquist de la permittivité suivant la loi de Cole-Cole.

Nous avons pu noter que ces différents types de polarisations sont dépendants de la fréquence. Ainsi, si nous sommes les différentes polarisations dues aux différents phénomènes présents et explicités plus haut, nous obtenons :

$$\vec{D} = \varepsilon_0 \cdot \left(1 + \sum_i \chi_{elec_i}(\omega) + \sum_i \chi_{ion_i}(\omega) + \sum_i \chi_{dip_i}(\omega) + \sum_i \chi_{int_i}(\omega) \right) \cdot \vec{E} \quad 1.13$$

Dans la gamme de fréquences étudiées dans ce travail, les contributions électroniques et ioniques de la polarisation ne sont pas visibles mais sont comptabilisées dans une constante de permittivité hautes fréquences ϵ_{lat} (ou permittivité de réseau dans cristal) du fait que les fréquences étudiées sont inférieures aux fréquences caractéristiques de l'observation de ces phénomènes. L'équation précédente devient :

$$\vec{D} = \epsilon_0 \cdot \left(\epsilon_{lat} + \sum_i \chi_{dip_i}(\omega) + \sum_i \chi_{int_i}(\omega) \right) \cdot \vec{E} \quad 1.14$$

Avec

$$\epsilon_{lat} = 1 + \sum_i \chi_{elec_i} + \sum_i \chi_{ion_i} \quad 1.15$$

Lorsqu'un matériau est conducteur, il faut considérer sa conductivité σ_{dc} comme une contribution supplémentaire à sa permittivité complexe. Ainsi, le vecteur déplacement électrique s'écrit :

$$\vec{D} = \epsilon_0 \cdot \left(\epsilon_{lat} + \sum_i \chi_{dip_i}(\omega) + \sum_i \chi_{int_i}(\omega) + \frac{\sigma_{dc}}{i\omega\epsilon_0} \right) \cdot \vec{E} \quad 1.16$$

L'expression de la permittivité complexe s'écrit alors:

$$\epsilon(\omega) = \epsilon_{lat} + \sum_i \chi_{dip_i}(\omega) + \sum_i \chi_{int_i}(\omega) + \frac{\sigma_{dc}}{i\omega\epsilon_0} \quad 1.17$$

Le diagramme en coordonnées complexes attendu pour la permittivité est donc la somme de différentes contributions qui pourront être décorrélées par soustraction de chaque contribution. Le plus simple généralement est de commencer par les basses fréquences car les contributions sont bien plus importantes en termes de $\Delta\epsilon$ qu'aux hautes fréquences.

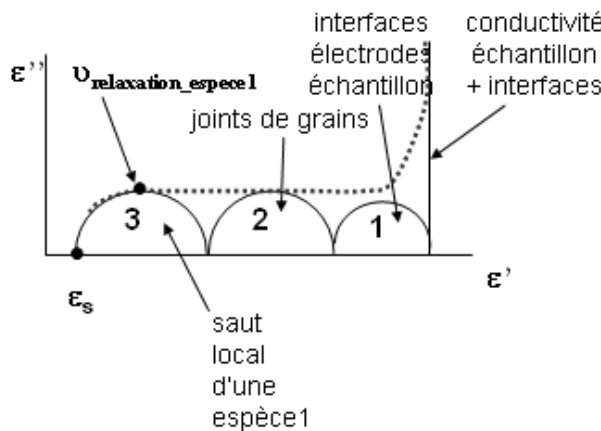


Figure 4. Diagramme de résistivité complexe d'un matériau conducteur.

Les fréquences caractéristiques des relaxations observées sont directement interprétables comme des fréquences caractéristiques de mouvements locaux de charge pour les polarisations dipolaires. En ce qui concerne les polarisations interfaciales, l'étude des fréquences permet de situer les différentes échelles d'analyse (joint de grain, agrégats,...) et permet aussi de comparer les phénomènes entre eux sur différents échantillons.

Les données de permittivité complexe $\varepsilon(\omega)$ peuvent être transformées en données de conductivité complexe $\sigma(\omega)$ ou résistivité complexe $\rho(\omega)$ à l'aide des relations :

$$\sigma(\omega) = i\omega\varepsilon_0\varepsilon(\omega) \quad 1.18$$

$$\rho(\omega) = \frac{1}{\sigma(\omega)} \quad 1.19$$

Avec ε_0 la permittivité du vide

Le diagramme de résistivité complexe révèle les différentes résistances qui sont rencontrées dans les chemins de conduction à travers l'échantillon. Il s'agit de la résistance lorsque le courant traverse un grain de matériau de part en part mais il s'agit aussi de résistances de contact entre entités, comme résistances de contact entre grains, entre agrégats de grains ou encore entre l'échantillon et les électrodes d'argent utilisées pour la mesure. Chaque contribution est modélisable par une loi de Cole-Cole similaire à celle utilisée en permittivité :

$$\rho(\omega) = \rho_{HF} + \frac{\rho_{BF} - \rho_{HF}}{1 + (i\omega\tau)^{1-\alpha}} \quad 1.20$$

où τ est le temps de relaxation, la fréquence de relaxation étant $v_r = (2\pi\tau)^{-1}$. α est un paramètre compris entre 0 et 1 et signifie l'existence d'une distribution de temps (ou fréquences) de relaxation centrée en τ (ou en v_r). Lorsque $\alpha = 0$, nous avons la loi de Debye pour laquelle le temps (fréquence) de relaxation est unique. ρ_{BF} et ρ_{HF} sont les permittivités limites de la relaxation lorsqu'on a respectivement $\omega\tau \ll 1$ et $\omega\tau \gg 1$. L'incrément de résistivité dû à la relaxation $\Delta\rho$ est égal à $\rho_{HF} - \rho_{BF}$.

Cette loi de Cole-Cole se matérialise dans le plan de Nyquist par un demi-cercle coupant l'axe des abscisses en ρ_{BF} et ρ_{HF} et centré au point de coordonnées

$$\left[\frac{\rho_{HF} + \rho_{BF}}{2}; -\frac{\Delta\rho}{2} \tan\left((1-\alpha)\frac{\pi}{2}\right) \right]. \quad 1.21$$

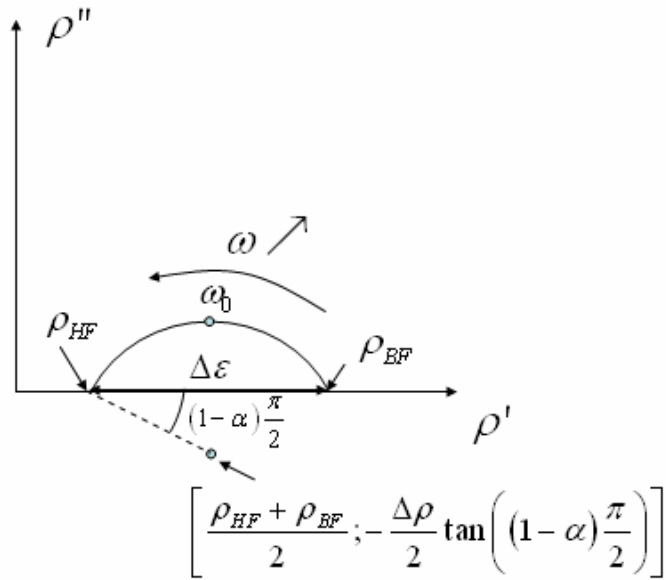


Figure 5. Représentation d'une relaxation dipolaire de permittivité par la loi de Cole-Cole.

Le sommet du cercle est atteint à la fréquence de relaxation caractéristique de l'échantillon et le centre du cercle est situé sous l'axe des abscisses.

Du fait de la mise en série de ces différentes résistances rencontrées le long d'un chemin de conduction, le diagramme en coordonnées complexes attendu pour la résistivité est la somme de différentes contributions qui pourront être décorrelées par soustraction. Le plus simple généralement est de commencer par les basses fréquences car les contributions sont bien plus importantes en termes de $\Delta\rho$ qu'aux hautes fréquences.

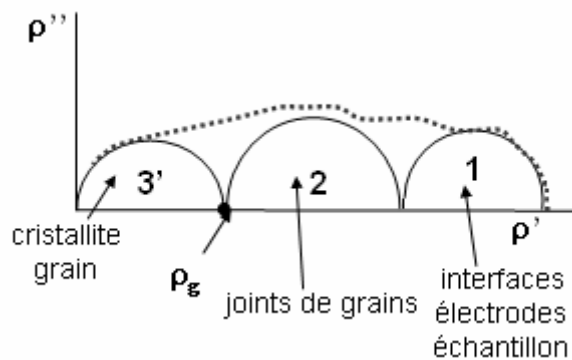


Figure 6. Diagramme de résistivité complexe d'un matériau conducteur.

Le seul but de l'utilisation de ces diagrammes dans ce travail est la recherche de la résistivité du grain ρ_g , point d'intersection de la partie basses fréquences de la dernière composante de résistivité avec l'axe des abscisses comme stipulé dans la Fig.6.

Les diagrammes de conductivité complexe ont pu être eux utilisés dans ce même but. La procédure d'obtention de σ_g est différente. Dans un diagramme de conductivité complexe, la partie hautes fréquences est particulièrement accentuée par rapport à la partie basses fréquences. La dernière contribution visible en résistivité étant un demi-cercle passant par 0, ceci est équivalent en conductivité à une droite oblique. En conséquence, une droite oblique est recherchée dans le diagramme de conductivité complexe. L'extrapolation à basses fréquences permet d'atteindre la valeur de σ_g lors de l'intersection de cette droite avec l'axe des abscisses. Un diagramme de conductivité complexe typique est présenté en Fig.7.

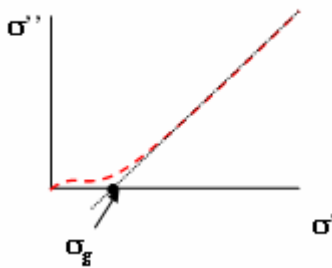


Figure 7. Diagramme de conductivité complexe typique montrant la droite permettant l'obtention de la conductivité de grain σ_g

1.3. Aspects expérimentaux

L'expérience consiste à étudier l'interaction d'une onde électromagnétique de fréquence comprise entre 40 Hz et 10 GHz et une pastille de poudre compactée à analyser. Cette onde est émise à l'aide d'un analyseur de réseaux ou bien d'impédance par le biais d'une sortie coaxiale. L'interaction est matérialisée par l'étude du coefficient de réflexion de l'onde lorsque la pastille est placée en bout d'une ligne coaxiale terminée par un court-circuit (montage dit « en réflexion »).

Méthode expérimentale: la théorie

Une onde électromagnétique (transverse électromagnétique TEM) est émise par un analyseur de réseaux ou d'impédance via une sortie coaxiale. Cette onde TEM se propage dans un guide

coaxial. L'interaction onde/échantillon est décrite par le coefficient de réflexion de l'onde TEM lorsque l'échantillon est placé au bout d'une ligne coaxiale terminée par un court-circuit. La figure 8 montre la cellule de mesure pour déterminer les paramètres électriques d'un échantillon en fonction de la fréquence.

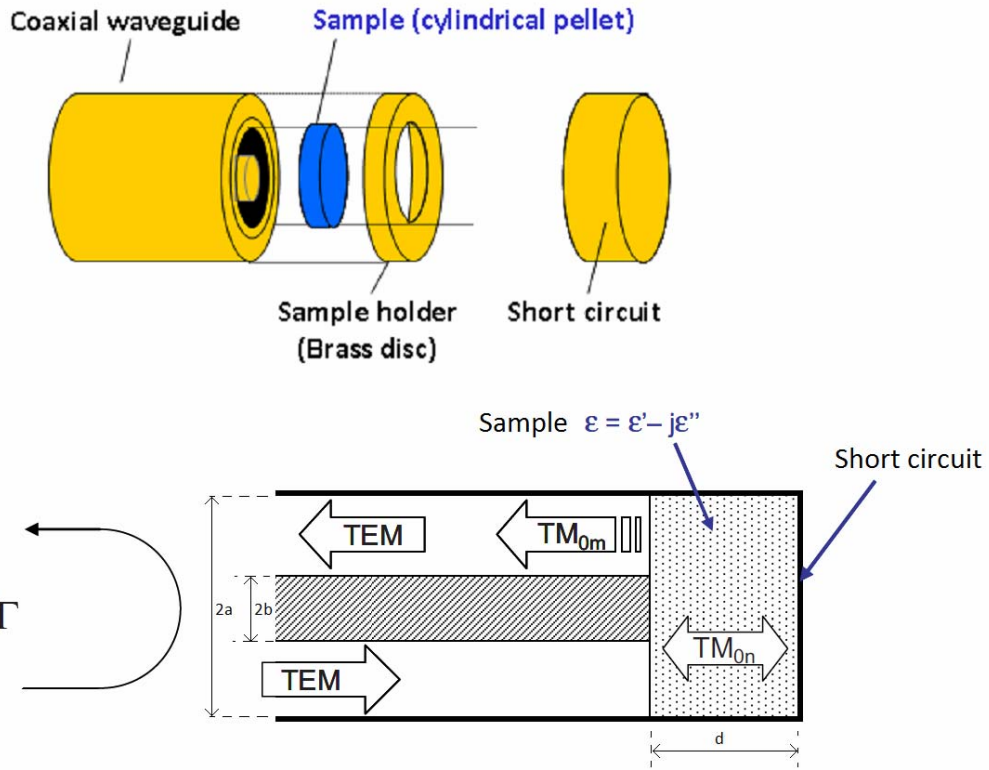


Figure 8. Schémas 3D et 2D de la cellule de mesure en mode réflexion. TM_{0m} ou n sont les modes Transverse Magnétique (voir le texte).

Ces paramètres sont calculés à partir du coefficient de réflexion Γ . Ce calcul a été résolu par N.E. Belhadj-Tahar et al [2]. Il a montré que l'onde incidente TEM génère, à l'interface du guide d'onde coaxial / échantillon, une onde réfléchie TEM et des ondes transverses magnétiques (TM_{0n} ou TM_{0m}) dans le guide coaxial et dans l'échantillon. Avec ce modèle, l'admittance Y_s à l'interface guide coaxial/ échantillon est donnée par:

$$Y_s = Y_0 \frac{jk_0 \epsilon_r}{\ln \frac{b}{a}} \cdot \sum_{n=1}^{\infty} \frac{2J_0^2(k_{Bn}a) \coth \left[\sqrt{k_{Bn}^2 - k_0^2 \epsilon_r} d \right]}{\sqrt{k_{Bn}^2 - k_0^2 \epsilon_r} [k_{Bn} b J_1(k_{Bn} b)]^2} \cdot \left[1 - a \sum_{m=1}^{\infty} \frac{A_m}{A_0(1+\Gamma)} \cdot \frac{Z_1(k_{Am}a)}{\left(\frac{k_{Am}}{k_{Bn}} \right)^2 - 1} \right] \quad 1.22$$

où a et b sont respectivement les rayons des conducteurs interne et externe, ϵ_r la permittivité complexe (relative), k_0 la constante de propagation dans l'air. k_{Am} et k_{Bn} sont respectivement les constantes de coupure des modes TM_{0m} et TM_{0n} dans la cellule. Y_0 est l'admittance caractéristique du guide d'ondes coaxial (0.02 S), A_0 l'amplitude de l'onde TEM incidente, A_m l'amplitude des ondes TM_{0m} . J_0 et J_1 sont les fonctions de Bessel de première espèce et Z_1 une combinaison de fonctions de Bessel de première et deuxième espèces:

$$Z_1(k_{Am}a) = J_1(k_{Am}a) + \left[\frac{-J_0(k_{Am}a)}{N_0(k_{Am}a)} N_1(k_{Am}a) \right] \quad 1.23$$

Le coefficient de réflexion Γ , l'impédance Z_s , et l'admittance $Y_s = G + jB$ sont reliés par l'expression suivante:

$$Z_s(\omega) = Z_0 \frac{1 + \Gamma(\omega)}{1 - \Gamma(\omega)} = \frac{1}{Y_s(\omega)} \quad 1.24$$

où Z_0 est l'impédance caractéristique de la ligne coaxiale (50 Ω). Les mesures ont été effectuées avec des guides coaxiaux de type APC7-mm ($2a = 7$ mm, figure 8). Les premiers modes d'ordres supérieurs (TM ou TE) commencent à se propager dans le câble coaxial à partir de 19,6 GHz, cette dernière fréquence étant la fréquence maximale de notre système de mesure (en fait 18 GHz, afin d'avoir une marge de sécurité). Notons qu'une bonne précision des mesures est assurée jusqu'à 10 GHz, car le dispositif contient de nombreuses transitions.

Dispositif expérimental

Les mesures du coefficient de réflexion en fonction de la fréquence sont faites sur une large bande de fréquences, de 40 Hz à 10 GHz, à l'aide de trois appareils : un analyseur de réseaux aux hautes fréquences (Agilent PNA E8364B de 10 MHz à 10 GHz), un analyseur d'impédance aux moyennes fréquences (Agilent 4291 de 1 MHz à 1,8 GHz) et un analyseur d'impédance aux basses fréquences (Agilent 4294 de 40 Hz à 110 MHz). Un commutateur

(switch) permet d'utiliser successivement ces analyseurs sans démontage de la cellule, ce qui est très important lors de mesures en fonction de la température.

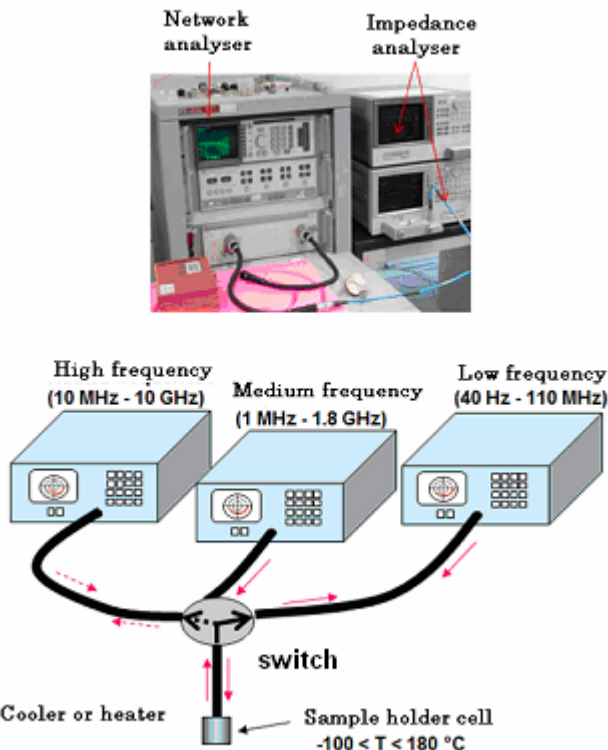


Figure 9. Dispositif expérimental montrant l'utilisation des trois analyseurs.

Etalonnage

La première étape expérimentale consiste à calibrer les analyseurs. Cela signifie qu'on mesure différentes charges connues. Ces références sont les suivantes :

- un circuit ouvert (capacité $C = 89 \text{ fF}$) caractérisé par $|\Gamma(\omega)| = 1$,
- un court-circuit caractérisé par $\Gamma(\omega) = -1$,
- une charge de 50Ω appelée « charge adaptée » caractérisée par $\Gamma(\omega) = 0$.

Une fois les appareils étalonnés, l'impédance mesurée dans le plan P, plan d'étalement, c'est-à-dire le plan perpendiculaire à l'axe de la ligne coaxiale à l'interface ligne coaxiale / pastille, est calculable à partir du coefficient de réflexion par la formule suivante :

$$Z_p(\omega) = Z_0 \frac{1 + \Gamma(\omega)}{1 - \Gamma(\omega)} \quad 1.26$$

Avec Z_0 l'impédance caractéristique de la ligne coaxiale (soit 50Ω). Cette impédance est convertie en admittance dans le fichier issu directement de l'expérience selon la relation classique :

$$Y_s(\omega) = \frac{1}{Z_s(\omega)} = G_s + iB_s \quad 1.27$$

La partie réelle de l'admittance est appelée conductance et la partie imaginaire la susceptance. Une fois que les analyseurs de réseaux ou d'impédance sont étalonnés, l'impédance (ou le coefficient de réflexion) de la cellule contenant l'échantillon sous test peut être mesuré dans le plan d'étalonnage.

2. Références bibliographiques

¹ J.C. Badot, E. Ligneel, O. Dubrunfaut, D. Guyomard, B. Lestriez, *Adv. Funct. Mater.*, 19 (2009) 2749

² N.E. Belhadj-Tahar and A. Fourrier-Lamer, *IEEE Trans. Microwave Theory Tech.*, 34 (1986) 346

Chapitre 2

1. Introduction

Il existe une forte demande pour le développement de nouvelles batteries avec des performances améliorées par rapport à l'état de l'art technologique de la batterie au lithium ion. Pour atteindre cet objectif, une meilleure compréhension fondamentale des facteurs qui limitent les performances électrochimiques est nécessaire. À ce jour, ces dernières sont généralement décrites en utilisant des modèles macroscopiques qui supposent que les électrodes sont homogènes, isotropes et sans défaut. [1] Toutefois, les électrodes composites sont des architectures hiérarchiques avec différents niveaux. [2,3] Il y a eu un certain nombre d'efforts de modélisation récents visant à inclure des informations plus détaillées microstructurales. [4,5,6,7] Tous ces modèles bénéficieraient de données microstructurales directes. Mais de nouvelles techniques doivent être développées pour cela. [8,9,10,11].

La conductivité électronique est l'une des deux principales propriétés (l'autre étant la conductivité ionique) de l'électrode composite au regard de son comportement électrochimique. [12] Cependant, il n'y a pas de modélisation de cette propriété, car seule la conductivité, σ_{DC} , a été mesurée à ce jour. σ_{DC} est une valeur moyenne macroscopique qui donne une information incomplète sur les propriétés de transport électrique des matériaux granulaires, tels que les électrodes composites, constituées de clusters de particules (éventuellement) et de particules séparées par des barrières résistives et capacitives (par exemple les frontières entre clusters ou particules), qui limitent les transports de charge dans le matériau. Nous avons récemment proposé la technique de spectroscopie diélectrique à large bande (BDS) (40 à 10^{10} Hz) pour révéler le transport électronique à toutes les échelles de l'architecture d'une électrode composite, des distances inter-atomiques aux dimensions macroscopiques. [13]

La réponse électrique d'un matériau est due à des fluctuations de densité de charge, quand il est soumis à un champ électrique dépendant du temps. Cette réponse peut être décrite soit par la densité courant dépendante du temps $j(t)$ ou par le moment dipolaire dépendant du temps $\mu(t)$. L'échelle de temps (ou temps de relaxation) des fluctuations dépend généralement de l'échelle géométrique à laquelle ils surviennent. Dans le domaine des fréquences, ces fluctuations sont soit exprimées par la permittivité complexe $\epsilon(\omega)$, la conductivité complexe $\sigma(\omega)$ ou la résistivité complexe $\rho(\omega)$, qui sont liés par,

$$\sigma(\omega) = [\rho(\omega)]^{-1} = i \varepsilon \omega \varepsilon_0(\omega) \quad (2.1)$$

où ε_0 est la permittivité du vide, et $\omega = 2\pi v$ la pulsation exprimée en rad.s⁻¹ (v étant la fréquence exprimée en Hz). Des fréquences optiques aux basses fréquences, la polarisation électrique d'un échantillon est la somme des polarisations élémentaires différentes, soit électronique, atomique, polarisations dipolaires et interfaciales. [14,15] De ce fait, il est démontré que pour les fréquences inférieures à 10¹¹ Hz, les spectres diélectriques des composés solides sont la somme de plusieurs relaxations diélectriques et sont donc données par

$$\varepsilon(\omega) = \varepsilon_\infty + \sum_j \chi_j(\omega) = \varepsilon_\infty + \sum_j \frac{\varepsilon_{j,L} - \varepsilon_{j,H}}{1 + (i\omega\tau_{j,\varepsilon})^{1-\alpha_{j,\varepsilon}}} \quad (2.2)$$

où ε_∞ est la permittivité de réseau, χ_j correspondent aux susceptibilités des différents mécanismes (polarisations dipolaires et interfaciales) et sont souvent décrits par la fonction de relaxation Cole-Cole (appelé ci-après CC-fonctions). L'intensité de la relaxation est $\Delta\varepsilon_j = (\varepsilon_{j,L} - \varepsilon_{j,H})$ et correspond à une susceptibilité dipolaire ou interfaciale électrique. $\tau_{j,\varepsilon}$ sont les temps moyen de relaxation correspondants avec des fréquences de relaxation $\nu_{j,\varepsilon} = (2\pi\tau_{j,\varepsilon})^{-1}$. $\alpha_{j,\varepsilon}$ sont des paramètres variant entre 0 et 1 qui expriment l'écart avec la réponse idéale de Debye. Les différents mécanismes de polarisation surviennent aux différentes échelles avec des fréquences caractéristiques distinctes peuvent ainsi être séparés et traités individuellement. De même, les spectres de résistivité sont décrits par une somme de fonctions de relaxation, chacun d'entre eux donnée par,

$$\rho_j(\omega) = \rho_{j,H} + \frac{\rho_{j,L} - \rho_{j,H}}{1 + (i\omega\tau_{j,\rho})^{1-\alpha_{j,\rho}}} \quad (2.3)$$

$\rho_{j,L}$ et $\rho_{j,H}$ sont respectivement les limites basse et haute fréquences de la résistivité et $\tau_{j,\rho}$, un temps de relaxation. La fonction de Cole-Cole est généralement due à l'existence d'une distribution continue des temps de relaxation.

Après la démonstration de son activité électrochimique par Padhi *et al.* il y a quinze ans [16], LiFePO₄ est maintenant commercialisé comme matériau actif d'électrode positive de la

nouvelle génération lithium-ion. LiFePO₄ est un conducteur mixte qui peut avoir un mouvement coopératif des ions lithium et polarons. [17] La conductivité électronique est connue pour être de type transfert de petits polarons (trous) [18] ; ces porteurs de charge étant piégés par les sites de lithium vacants. Les polarons sont des électrons localisés dans le solide, piégés par le réseau ionique du simple fait de la polarisation qu'il induit autour de lui. L'électron et la polarisation qui l'accompagne peuvent être traités comme une pseudo-particule appelée polaron. On distingue petit (conduction par saut thermiquement activé à haute température, et de bande / effet tunnel à basse température) et grand (conduction de bande à toute température) polarons, selon que la polarisation induite par l'électron s'étend sur des distances inférieures ou supérieures à la distance intersite.

Les valeurs précédemment publiées pour la conductivité électronique de LiFePO₄ sont comprises entre 10^{-7} à 10^{-8} S/m [19] et la conductivité ionique est mesurée comme étant dans la même gamme. [20] LiFePO₄ est habituellement enveloppé par un enrobage de carbone. Celui-ci est un film de carbone amorphe qui contient de petits domaines de carbone hybridés sp² (longueur de corrélation dans le plan de 1-4 nm) liés par des atomes de carbone hybridés sp³, avec quelques groupes fonctionnels (hydroxyles, aldéhydes, cétones...) adsorbés à sa surface. [21,22] La structure la plus probable est celle dans laquelle les sites sp² sont organisés en grappes compactes de couches graphitiques délimitée par les sites sp³. [23] D'autres travaux théoriques suggèrent que le carbone hybridé sp² a plutôt tendance à former des structures en chaîne avec une dimension fractale comprise entre 1 et 2, mais pour des films de carbone contenant une majorité de carbone hybridé sp³. [24] L'enrobage en carbone augmente la conductivité du matériau, fournit sans doute de meilleurs contacts électroniques entre les particules submicroniques dans les gros clusters, et donc améliore les performances électrochimiques. [25,26] La teneur en carbone doit être assez élevée pour assurer un enrobage complet et homogène des particules, mais les enrobages trop épais (avec une épaisseur moyenne de 5-10 nm) montrent un effet de détérioration de la performance électrochimique, reflétant probablement une entrave cinétique au passage des ions lithium. [27,28] Il est généralement observé une augmentation de la conductivité électrique et une diminution de l'énergie d'activation lorsque la teneur en sp² augmente. [29,30,31,32] La plupart des études expérimentales indiquent que le transport électronique, en particulier près de la température ambiante et à bas champs électriques ($<10^4$ V.cm⁻¹), se fait par saut (*hopping*) ou par conduction tunnel entre les domaines du sp². [33] Dans des travaux précédents, les performances électrochimiques des électrodes composites à base de LiFePO₄ ont été étroitement corrélées à la conductivités macroscopique

(d'échantillon) de la matière active. [34,35] Des capacités de décharge supérieures et une meilleure tenue en puissance d'électrodes composites LiFePO₄ sont directement corrélés avec une teneur accrue de domaines de carbone sp² (vs- sp³) telle que déterminée par spectroscopie Raman ; une tendance qui peut être interprétée en termes de quantité croissante de plus grands clusters de graphène dans l'enrobage de carbone désordonné.

À ce jour, aucune mesure directe de la conductivité de l'enrobage de carbone n'a pu être réalisée en raison de l'absence de technique appropriée. Seules des relations indirectes entre la conductivité de pastilles macroscopique pressées ou frittées de C-LiFePO₄ et la teneur en carbone sp² ont été proposées. [29,34,35] Ici, nous utilisons la spectroscopie diélectrique à large bande des basses fréquences (quelques Hz) aux micro-ondes (quelques GHz), ce qui permet de mesurer les propriétés électriques (la permittivité, la résistivité et la conductivité) par rapport à la fréquence, donc à différentes échelles de nanocomposites C-LiFePO₄.

2. Résultats et discussion

2.1. Morphologie et analyse des échantillons

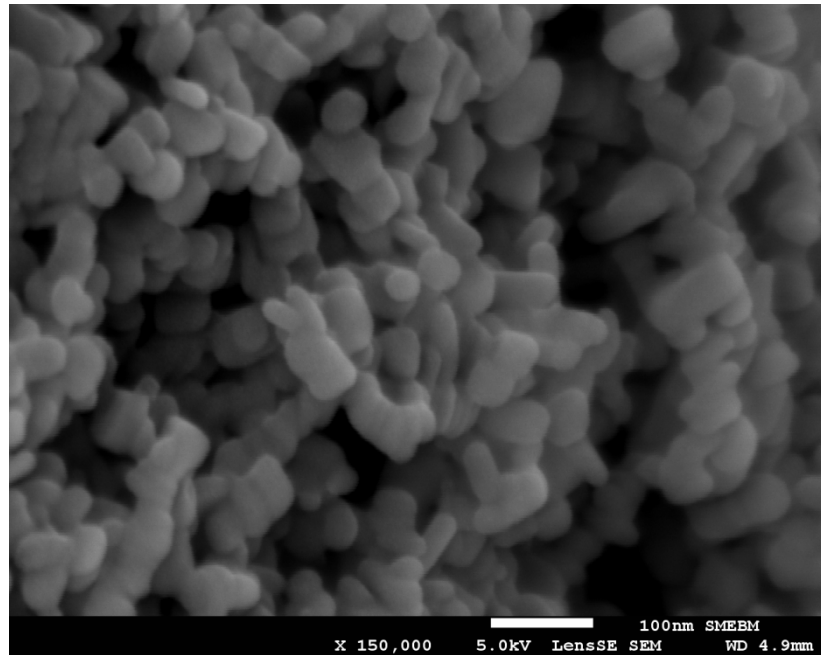
Le composé de base LiFePO₄ et trois différents échantillons de C-LiFePO₄ ont été étudiés avec la taille moyenne des particules variant de 50 à 150nm (Tableau 1).

Tableau 1. Caractéristiques des différents échantillons : taille des particules selon Umicore, épaisseur de l'enrobage de carbone déterminée par MET, %sp² dans l'enrobage déterminée à partir des mesures XPS.

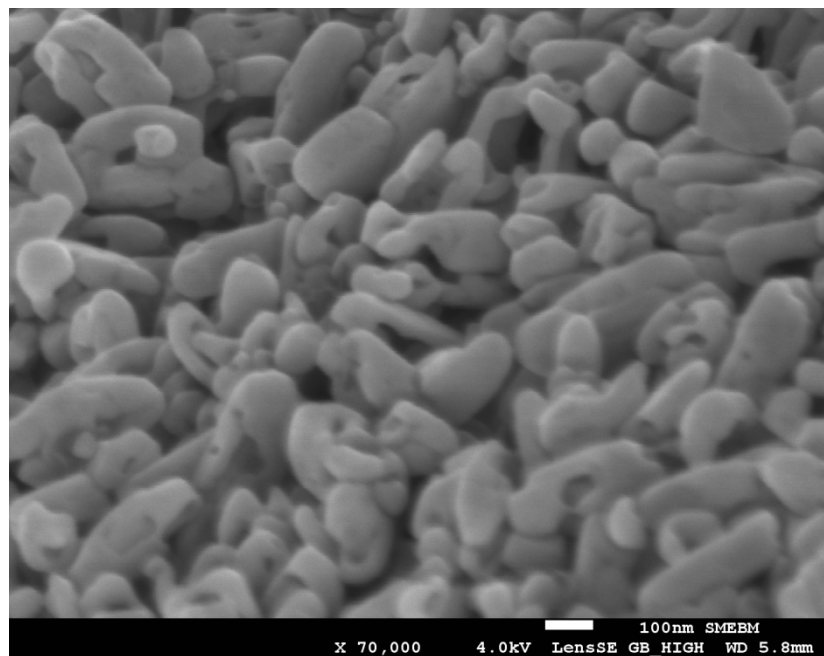
Echantillon	Taille de particule (nm)	Epaisseur de l'enrobage (nm)	%sp ² dans l'enrobage	Porosité de la pastille ϕ_p (%)	Fraction volumique de carbone par cluster ϕ_{cc}
LFP	150	-	-	47	-
CLFP1	50	3.00	64	45	3.8x10 ⁻²
CLFP2	150	2.80	52	40	3.0x10 ⁻²
CLFP3	150	4.60	70	48	3.6x10 ⁻²

Les clichés MEB mettent en évidence des clusters (particules agglomérées par l'enrobage de carbone) (Figure 1a-b). Un enrobage en carbone homogène et continu a été observé autour des particules dans tous les cas (figure 1c). Des domaines graphitiques sp² sont observés

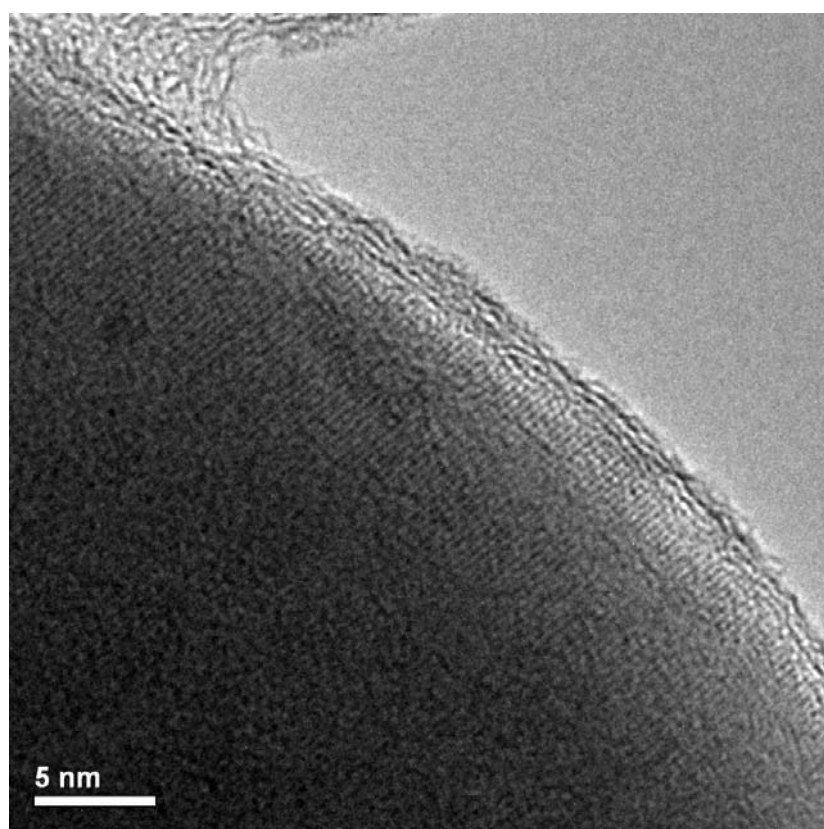
parallèlement à la particule au bord plutôt que près de l'interface particule-enrobage. En outre, il est clair que les zones sp^2 sont séparées par des zones amorphes (non sp^2) ici et là. Dans les spectres EELS, l'existence d'un pic fin à 284eV (transition 1s- π^*) indique une hybridation principalement sp^2 dans nos matériaux. [36] Le deuxième pic à 291eV (transition 1s- σ^*) correspond à une hybridation de type sp^3 . [36] L'absence de trois pics caractéristiques habituellement associés au graphite (100% d'hybridation de type sp^2) qui sont souvent dans la gamme d'énergie entre 295 et 310 eV est aussi évidente. [37] La combinaison de toutes ces informations indique l'existence d'hybridations multiples dans notre système, complétant les résultats TEM. La quantification des teneurs en sp^2 et sp^3 dans le revêtement a été réalisée en utilisant la technique XPS (figure 1E) par décomposition de l'énergie de liaison de cœur (BE) du C1s. Les états d'hybridation sp^2 et sp^3 ont été fittés à 284.74eV et 285.63eV. [38,39] Trois pics supplémentaires ont été introduits dans la décomposition des spectres C1s pour tenir compte des oxydations dues à l'environnement. Soit : CO, C=O et COO de 286.78eV, 288.31eV et 289.4eV respectivement. Des procédures analogues ont été suivies dans d'autres travaux. [40] Le pourcentage en sp^2 a été calculé en tenant compte de toutes les contributions, plutôt que simplement sp^2 et sp^3 . Les résultats sont rapportés dans le Tableau 1.



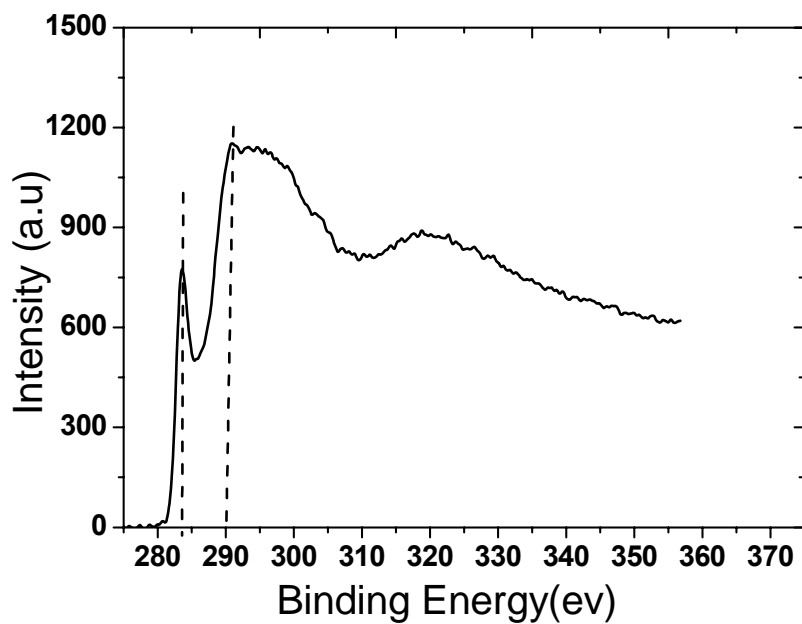
(a)



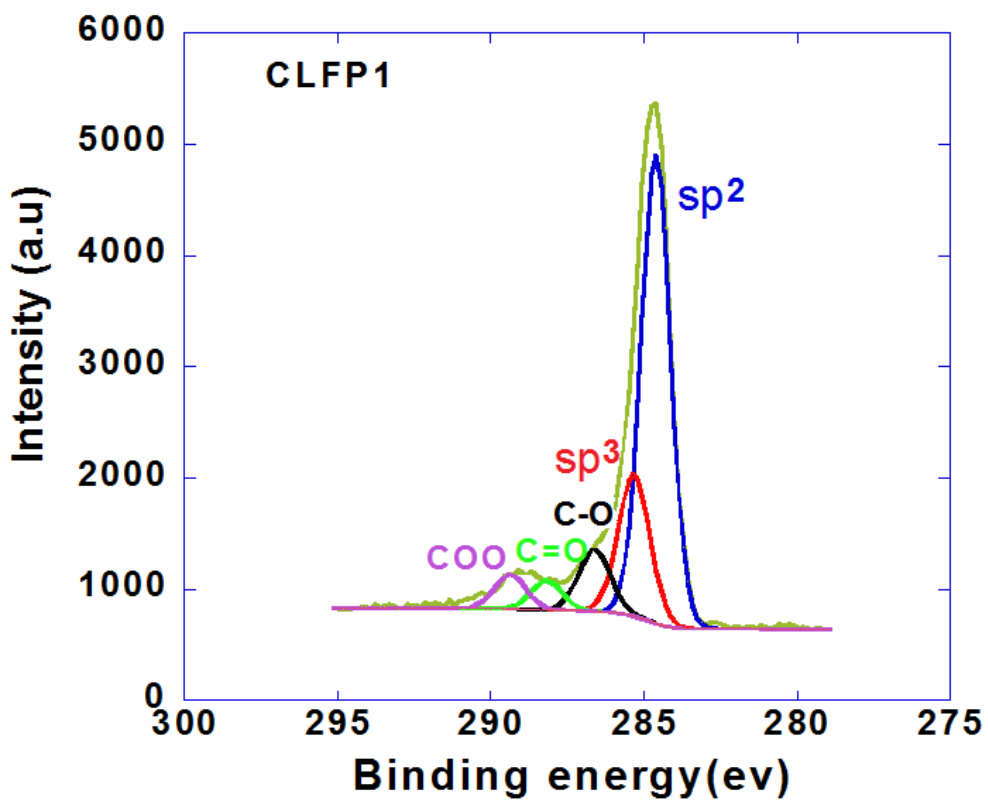
(b)



(c)



(d)



(e)

Figure 1. Clichés (a) MEB de CLFP1. (b) MEB de CLFP3. (c) MET de CLFP3. (d) Spectre EELS type de CLFP3. (e) Spectre XPS (300-275 eV) type dans la région de C1s de CLFP1.

2.2. Les mesures électriques: identification des différentes relaxations et leurs attributions (les mécanismes de conductivité électronique).

Les spectres complexes de la résistivité et la permittivité ont été enregistrés sur une large plage de fréquences de 40 à 10^{10} Hz (Fig. 2). Les échantillons ont été métallisés avec un laque d'argent afin d'assurer de bons contacts entre les échantillons et le dispositif de mesure. Cependant, puisque ce métal est une électrode bloquante pour les ions lithium, la conductivité DC que nous mesurons ici sera seulement due aux transferts d'électrons, avec cependant une accumulation d'ions lithiums aux électrodes d'argent.

La dépendance en fréquence de la partie réelle de la conductivité et de la permittivité de LiFePO₄ (LFP) à la température ambiante est montrée dans les figures 2a et 2b, respectivement. La plus basse valeur mesurée pour la conductivité est environ 10^7 S.m⁻¹ à 40Hz et l'absence de plateau à basse fréquence montre que notre dispositif ne permet pas l'accès à la très faible valeur de la conductivité DC pour ce matériau. La Figure 2b montre également l'existence d'une relaxation diélectrique à environ 10² Hz (à température ambiante), car la valeur ϵ' baisse de 40 à une valeur constante égale 4 à fréquences plus élevées (au-dessus 10⁶ Hz). Cette relaxation pourrait être attribuée aux contacts entre clusters ou à l'interface laque d'argent / l'échantillon. Au dessus de 10⁵ Hz, la dépendance en fréquence de la conductivité de LiFePO₄ suit une loi de puissance:

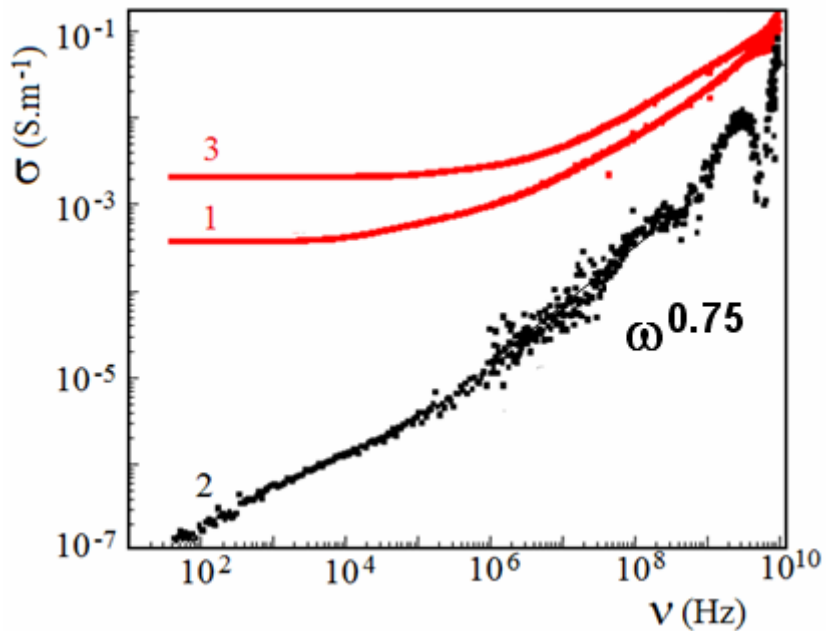
$$\sigma = A \omega^s \quad (2.4)$$

A et s sont des constantes. La valeur de l'exposant s = 0.75 est typique d'un mécanisme de conduction électrique dans les systèmes désordonnés et dans les réseaux cristallins à faible teneur en sites localisés distribués au hasard (ici les lacunes de lithium [18]). [41]

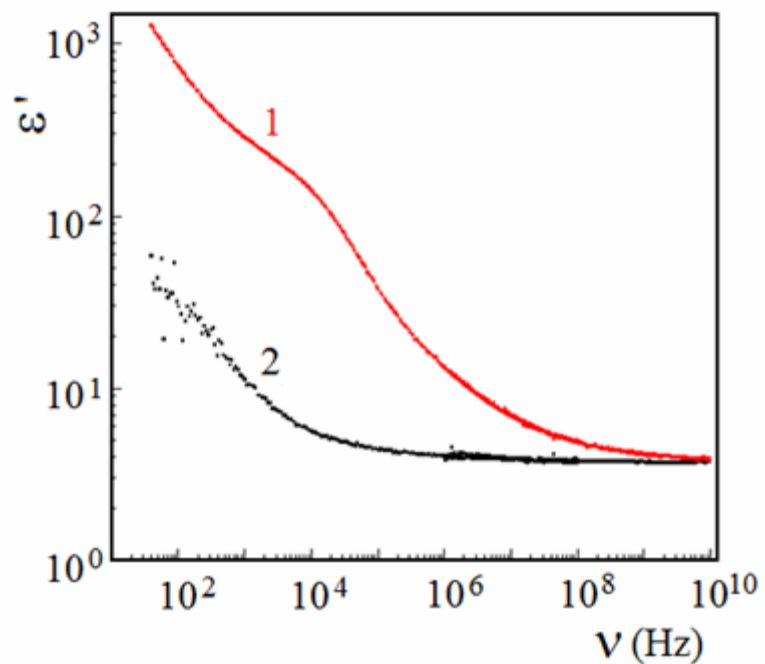
L'enrobage de carbone dans C-LiFePO₄ augmente considérablement la conductivité électrique dans la gamme de fréquences (figures 2a). A 298K, au dessous de 10⁵ Hz, la conductivité DC, σ_s , de l'échantillon a une valeur de plus de 10⁻⁴ S.m⁻¹ et la conductivité à haute fréquence atteint près 10⁻¹ S.m⁻¹ dans la région des GHz. Ce type de dépendance en fréquence de la conductivité montre que dans le composite C-LiFePO₄ l'enrobage de carbone constitue est percolant dans tout l'échantillon. [42] Cette situation résulte de la morphologie cœur-couronne du matériel LiFePO₄ et son enrobage de carbone. [43,44] La disparition de l'évolution en loi de puissance dans l'échantillon CLFP3 ainsi que l'existence d'un ou plusieurs

domaines de relaxation-dessus 0.1MHz confirment le rôle dominant de l'enrobage de carbone sur la conductivité dans les composite C-LiFePO₄ (fig. 2a). La Figure 2b montre l'existence d'une relaxation à basse fréquence (environ 10⁴ Hz) pour CLFP3. A plus hautes fréquences, les permittivités de C-LiFePO₄ et LiFePO₄, ϵ_{∞} , convergent vers une valeur résiduelle indépendante de la fréquence, correspondant à la permittivité effective de LiFePO₄ (LFP). En effet, dans CLFP3, la fraction volumique en carbone dans l'échantillon est trop faible pouvoir jouer de manière significative sur la permittivité résiduelle ϵ_{∞} .

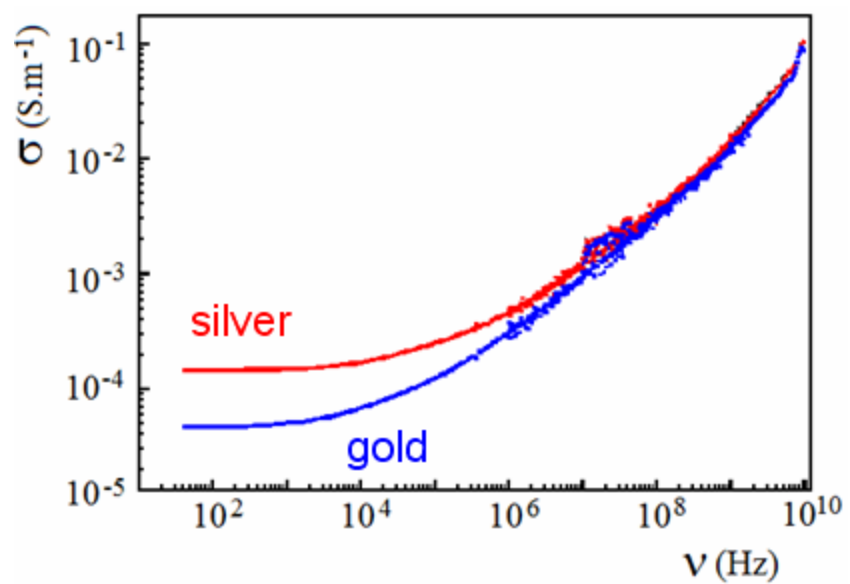
Le type de métallisation (i.e. laque d'argent ou d'or) affecte les spectres aux fréquences inférieures à 10⁶ Hz (Fig. 2c et 2d), probablement en raison d'une différence entre les fonctions de travail des métaux et celle de l'enrobage de carbone amorphe recouvrant les particules LFP. Comme les fonctions de travail de l'argent et du carbone amorphe sont presque similaires, la métallisation argent est plus favorable pour les mesures électriques de C-LiFePO₄. [45]



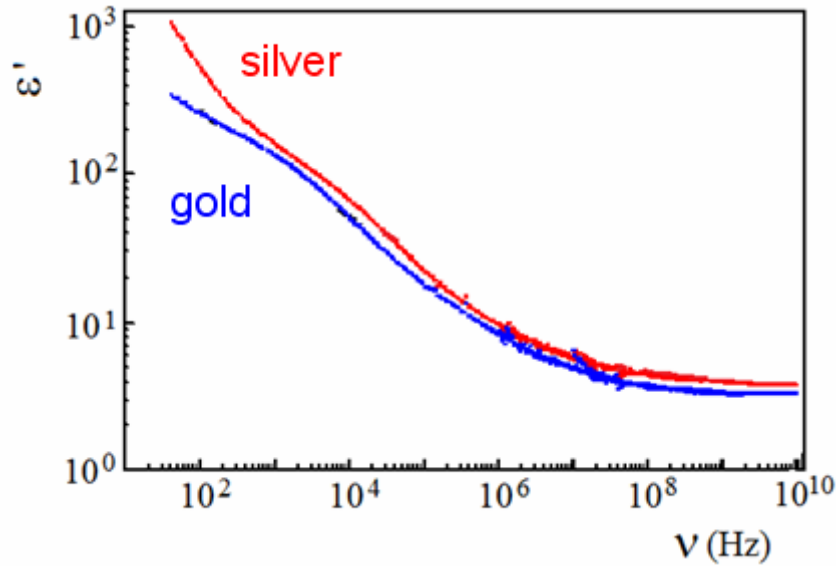
(a)



(b)



(c)



(d)

Figure 2. Parties réelle de la conductivité (a) et de la permittivité (b) en fonction de la fréquence pour les deux échantillons avec et sans enrobage de carbone, c'est à dire CLFP3 (courbe 1) et LFP (courbe 2), à 298K. En (a), la partie réelle de la conductivité est également donnée à 398K pour CLFP3. Parties réelle de la conductivité (c) et de la permittivité (d) en fonction de la fréquence et la métallisation, pour CLFP3 (courbe 3), à 298K

Dans la gamme des basses fréquences, les propriétés électriques de l'échantillon sont donc affectés par l'interface échantillon / métal. Par contre, pour les fréquences supérieures 10^6 Hz, les spectres diélectriques correspondent aux propriétés intrinsèques de l'échantillon, car ils sont invariants avec la nature de la métallisation. Dans le cas de CLFP3, la relaxation diélectrique, qui apparaît autour de 10^4 Hz à la température ambiante est donc due à la polarisation interfaciale résultant du contact métal / échantillon. Aux plus hautes fréquences, l'évolution négligeable de la conductivité vs la température indiquerait un comportement quasi-métallique dans l'enrobage carbone (fig. 2a).

Comme les relaxations diélectriques possibles ne sont pas clairement visibles dans la représentation dépendant de la fréquence, il est plus approprié d'utiliser les représentations de Nyquist qui offrent une plus grande facilité de décomposition des spectres diélectriques. Comme toutes les polarisations (relaxations) aux différentes échelles sont additives en raison de leur caractère vectoriel, leurs contributions peuvent donc être révélées par une procédure de décomposition des tracés de Nyquist (ϵ "vs ϵ'). [14] Cette décomposition, qui est réalisée sur les données enregistrées à l'aide d'un logiciel fait-maison (non commercial), est obtenue

par soustractions successives des différentes contributions des faibles aux hautes fréquences, en utilisant les fonctions Cole-Cole (appelé ci-après CC-fonction).

La figure 3a montre l'ensemble du tracé de Nyquist (Cole-Cole), à savoir ϵ'' vs ϵ' pour CLFP3 dans la partie basse fréquence du spectre diélectrique à 300 K. La première polarisation ou relaxation (D1) est représentable avec une bonne précision par une droite, ce qui correspond à une dépendance avec la fréquence en v^{n-1} de la permittivité complexe avec un exposant n d'environ 0.14 quel que soit l'échantillon et la température. Après soustraction de cette contribution à basse fréquence, un domaine de relaxation D2 (Fig. 3b) est mis en évidence et correctement représentable par un arc de cercle correspondant à une relaxation diélectrique décrite par la CC-fonction (Eq. 2). Le domaine de relaxation D3 (Fig. 3c) est défini sans ambiguïté après soustraction de la contribution et D2 est également décrit par la CC-fonction. Par la même procédure, la relaxation D4 relaxation (Fig. 3d) est obtenue.

Dans les autres échantillons (sauf LFP), la décomposition des tracés permet aussi d'identifier quatre phénomènes diélectriques de D1 à D4 (dont trois relaxations D2 à D4). Les différentes valeurs des paramètres α (α_1 , α_2 , α_3 et α_4), l'intensité des relaxations ($\Delta\epsilon_2$, $\Delta\epsilon_3$ et $\Delta\epsilon_4$), les fréquences de relaxation, (v_2 , v_3 et v_4) et leurs pré-facteurs (v_{02} , v_{03} et v_{04}) sont récapitulés dans le Tableau 2.

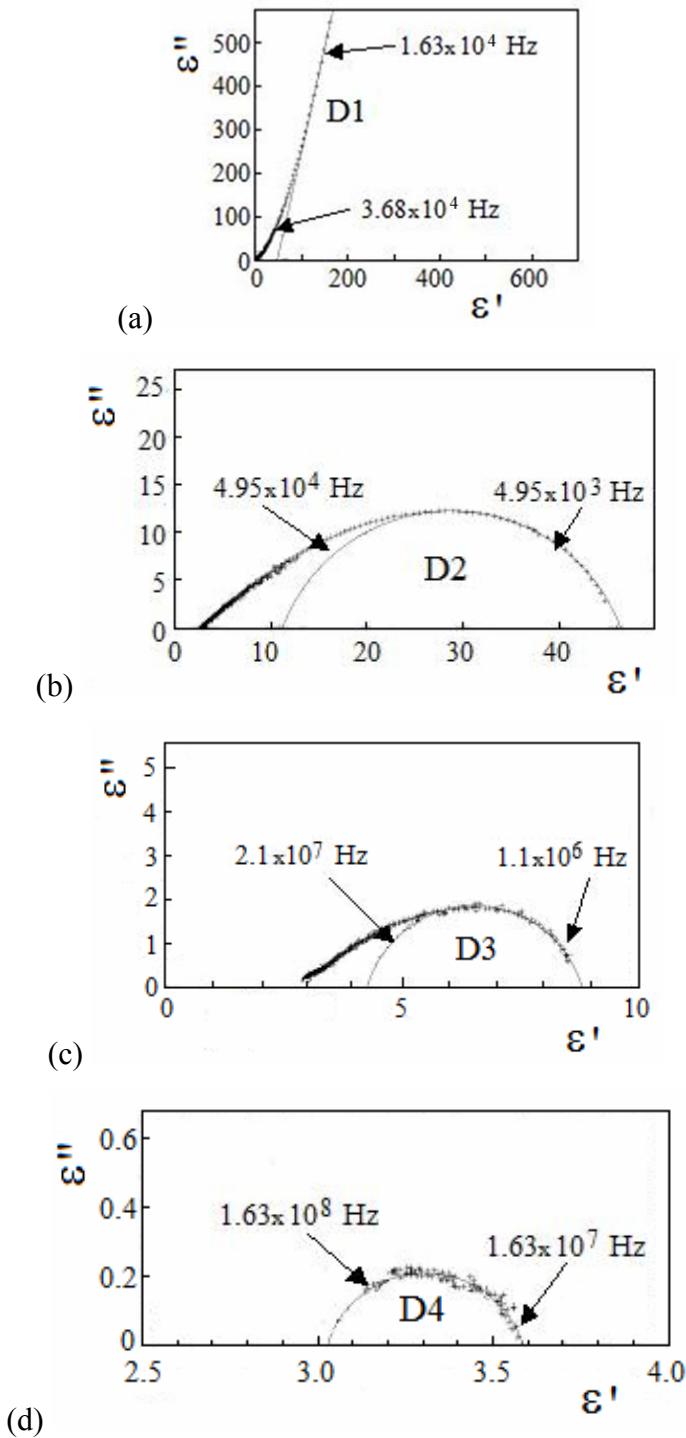


Figure 3. (a) à (d) Représentation Cole-Cole donnant la partie imaginaire $\epsilon''(v)$ vs. la partie réelle $\epsilon'(v)$ de la permittivité complexe à 298 K pour CLFP3: (a) tracé de 40 à 1010 Hz : seule la contribution (D1) due à la conductivité à basse fréquence représentée par une droite est visible, (b) Tracé obtenu après soustraction de la contribution D1 révélant la relaxation D2; (c) Tracé obtenu après soustraction de la contribution D2 révélant la relaxation D3; (d) Tracé obtenu après soustraction de la contribution D3 révélant la relaxation D4.

Tableau 2. Conductivité σ_i , énergie d'activation E_i , fréquence de relaxation diélectrique v_i à la température ambiante, pré-facteur v_{0i} , intensité des relaxations diélectriques $\Delta\epsilon_i$, et paramètres α_i associés aux différentes origines de polarisations au sein des différents échantillons: polarisations de saut (*hopping*) entre les domaines de carbone sp^2 (D4), de clusters (D3), et interfaciale (D2).

	Polarisation interfaciale D2	Polarisation des Clusters D3	Domaines sp^2 (<i>hopping</i>) D4	Permittivité résiduelle	Conductivité (S.m ⁻¹)		
Echantillon	v_2 (Hz) v_{02} (Hz) E_2 (eV)	v_3 (Hz) v_{03} (Hz) E_3 (eV)	v_4 (Hz) v_{04} (Hz) E_4 (eV)	ϵ_∞	Echantillon σ_S E_S (eV)	Cluster a) σ_{CLE} E_{CL} (eV)	sp^2 a) σ_{sp2e}
	$\Delta\epsilon_2$ α_2	$\Delta\epsilon_3$ α_3	$\Delta\epsilon_4$ α_4				
CLFP1	6.0×10^4 1.5×10^8 0.20	2.0×10^6 1.2×10^8 0.12	3.5×10^7 2×10^8 0.04	3.28	4.5×10^{-4} 0.19	1.2×10^{-2} 0.18	38
	84 0.09	7 0.18	2 0.26				
CLFP2	1.7×10^4 6×10^7 0.21	2.7×10^5 2.0×10^8 0.16	1.5×10^7 2×10^8 0.05	3.40	1.3×10^{-3} 0.19	1.0×10^{-2} 0.20	32
	6.90 0.01	4.5 0.2	1.08 0.18				
CLFP3	1.7×10^4 3×10^8 0.22	5×10^6 2×10^8 0.09	1.5×10^8 5×10^8 0.03	3.05	9.1×10^{-4} 0.16	2.5×10^{-2} 0.16	41
	39 0.24	4.5 0.18	0.58 0.10				

Toutes les fréquences de relaxation v_i ($i = 2, 3$ et 4) ont un comportement activé thermiquement,

$$v_i = v_{0i} \exp\left(-\frac{E_i}{kT}\right) \quad (2.5)$$

v_{0i} est le pré-facteur de fréquence, E_i l'énergie d'activation, k la constante de Boltzmann ($k = 1.38 \times 10^{-23} \text{ JK}^{-1}$) et T la température (figure 4a). Le tableau 2 récapitule l'énergie d'activation qui caractérise chaque relaxation diélectrique dans les différents échantillons.

Les Dispersions (D1) et (D2) se produisent à des fréquences inférieures à 10^6 Hz (à température ambiante) et dépendent de la métallisation, comme précédemment observé (figure 2c). (D2) est une relaxation diélectrique due à l'existence d'une polarisation

interfaciale à la jonction entre l'échantillon et la métallisation en argent, qui est souvent appelée par ailleurs une barrière de Schottky. La différence des fonctions de travail résulte en la formation d'une zone de déplétion chargée positivement dans l'échantillon (soit dans l'enrobage de carbone amorphe). La réponse de cette charge d'espace à un champ électrique alternatif est une relaxation diélectrique qui se produit généralement dans le domaine des basses fréquences. La fréquence de relaxation dépend de la largeur et la capacité de la barrière de Schottky. Par ailleurs, le domaine de dispersion (D1) décrit une dépendance en fréquence loi de puissance pour la permittivité, c'est à dire $\epsilon(\omega) = B(i\omega)^{-0.86}$, quelque soit la température., correspondant à une conductivité quasi DC. Ce comportement peut être expliqué par la rugosité de l'échantillon en raison de sa forte porosité (40 à 50%). Il en résulte un contact (échantillon / métallisation) plus petit que la surface géométrique de l'échantillon qui pourrait expliquer cette faible dépendance de fréquence.

Les relaxations (D3) et (D4) qui surviennent aux fréquences plus élevées sont ainsi des polarisations générées au sein de l'échantillon, car elles se produisent à des fréquences supérieures 10^6 Hz à température ambiante. Il est à noter que du point de vue de leur texture, les échantillons peuvent être vus comme des empilements de clusters dans lesquelles les particules sont liées/collés par la couche carbone amorphe (Fig. 1a-b). Cette couche mince forme un réseau continu au sein de chaque cluster et est constitué de domaines conducteurs sp^2 séparés par des défauts isolants sp^3 . En outre, il a été rapporté que le transport électronique dans les matériaux carbone amorphe avec des domaines de graphite désordonné est régi par sauts entre les domaines de carbone sp^2 . [31] Nous avons donc deux niveaux de polarisation dans les échantillons: (a) le premier (à grande échelle) étant le cluster et (b) le second (à plus petite échelle) impliquant la distance moyenne entre les domaines sp^2 . Comme il implique de plus longues distances pour le transport des charges, la polarisation du cluster se produit aux plus basses fréquences et donne donc lieu à la relaxation (D3).

La relaxation plus rapide (D4) est due à aux sauts entre domaines sp^2 séparés par des barrières SP^3 le long des particules. La fréquence de relaxation v_4 de (D4) a une énergie d'activation E_4 comprise entre 0,03 et 0,05 eV et un pré-facteur v_{04} avec une valeur moyenne autour de 3×10^8 Hz (tableau 2 et figure 4a). L'énergie d'activation E_4 de la fréquence v_4 est la barrière de saut entre deux domaines sp^2 séparé par un domaine SP^3 . Selon Mott et Davis [41], la fréquence

(ou probabilité) de saut d'un site occupé à un autre site inoccupé dépend du recouvrement des fonctions d'onde électroniques entre les deux sites. Cette fréquence est définie par

$$\nu = \nu_{ph} \exp(-2\alpha r) \exp\left(-\frac{E}{kT}\right) \quad (2.6)$$

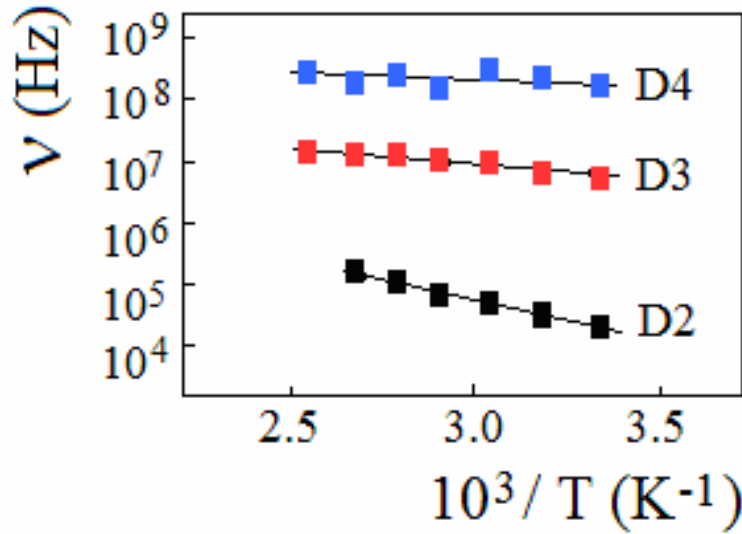
ν_{ph} est la fréquence ν phonons, r la séparation entre les domaines sp^2 , E la différence d'énergie (par exemple ici E_4) entre les sites localisés et α^{-1} est la longueur de localisation caractérisant l'extension spatiale de la fonction d'onde électronique. L'ordre de grandeur de la valeur moyenne du pré-facteur $\nu_0 = \nu_{ph} \exp(-2\alpha r) \approx 3 \times 10^8$ Hz peut être justifiée seulement si $\alpha^{-1} \ll r$. Ainsi, la valeur faible de ν_{04} pourrait être due à une localisation des électrons dans les domaines sp^2 . Le mécanisme de transport proposé entre les domaines sp^2 est similaire au mécanisme de transport par saut entre les régions mésoscopique métalliques (métaux granulaires [42]). L'énergie d'activation de ce mécanisme E_4 est donnée par l'énergie de charge,

$$E_4 = \frac{e^2}{4\pi\epsilon_0\xi} \left(\frac{1}{\epsilon_\infty} - \frac{1}{\epsilon_{LF}} \right) \quad (2.7)$$

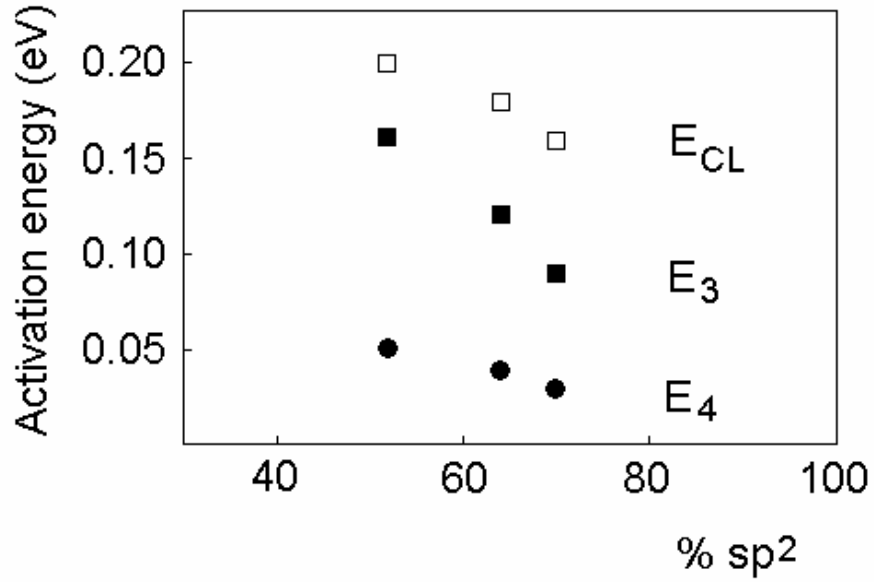
avec ξ la taille moyenne des domaines conducteur (ici sp^2), ϵ_{LF} est la permittivité statique à basse fréquence, et ϵ_∞ la permittivité à haute fréquence du nanocomposite C-LiFePO₄. Comme la fraction volumique en enrobage de carbone est négligeable, ϵ_∞ peut être identifiée à la permittivité de réseau de LiFePO₄. La permittivité statique $\epsilon_{LF} \gg \epsilon_\infty$ prend en compte la diminution d'énergie induite par la polarisation du milieu environnant (clusters). Considérant $\epsilon_\infty = 11,56$ calculé par M.S. Islam [47], $E_4 = 0,03$ à $0,05$ eV et $\epsilon_{LF} \gg \epsilon_\infty$, la taille moyenne des domaines sp^2 serait comprise entre 2,5 et 4 nm, en bon accord avec les observations de microscopie électronique en transmission haute résolution (HRTEM). [35]

E_3 est l'énergie d'activation de la fréquence caractéristique de polarisation des clusters. La figure 4b montre que les deux énergies d'activation E_3 et E_4 sont des fonctions décroissantes de la teneur en carbone sp^2 . L'énergie d'activation, E_3 plus élevé que E_4 , peut être associée à la barrière inter-particulaires pour le transport de charge dans l'enrobage à l'échelle du cluster. L'électron qui saute le long d'une particule par dessus une barrière E_4 peut également sauter

vers une autre particule par dessus une barrière E_3 . Cette énergie est plus élevée parce que la séparation entre les domaines sp^2 est plus grande entre deux particules voisines.



(a)



(b)

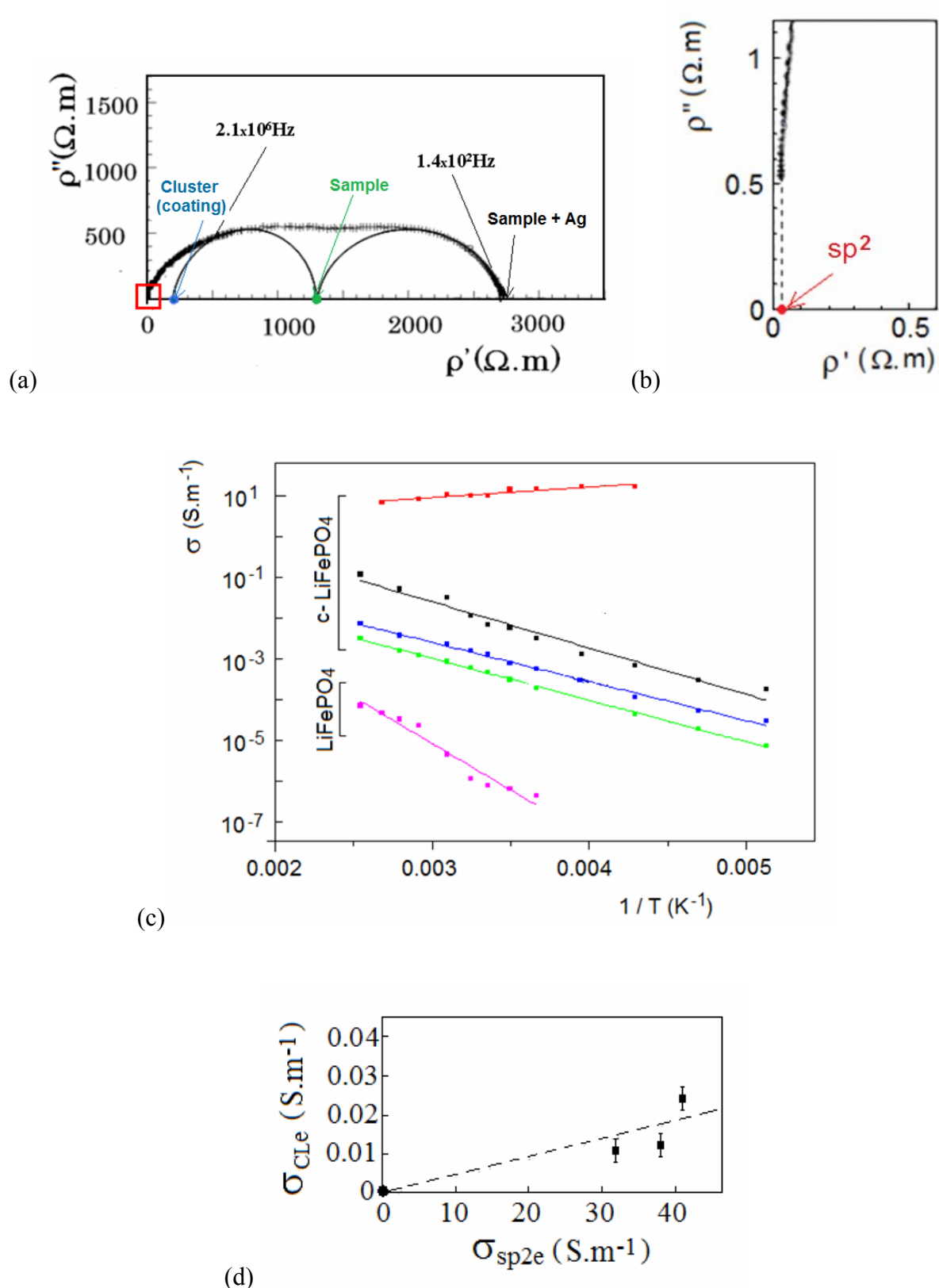
Figure 4. (a) Fréquences de relaxation des différentes polarisations (D2, D3 and D4) en fonction de l'inverse de la température pour CLFP3. (b) Energie d'activation E_{CL} , E_3 et E_4 vs. la teneur en carbone sp^2 content (% sp^2) dans l'enrobage pour la conductivité des clusters, la fréquence de relaxation des polarisations D3 (clusters) et D4 (hopping local entre domaines sp^2 domaines), respectivement.

Le diagramme de Nyquist de la résistivité (ρ "vs ρ') de CLFP3 à 300 K est représenté dans la Fig 5a. Pour extraire les différentes relaxations de résistivité, nous avons utilisé la même procédure de décomposition des tracés de Nyquist que pour la permittivité complexe. Le premier domaine de dispersion R1 est bien identifié par un arc de cercle dans la partie basse fréquence du tracé et ainsi décrite par la CC-fonction (Eq. 3). R1 coupe l'axe réel ρ' à ρ_s (limite haute fréquence) et ρ_{SM} (limite basse fréquence). Après soustraction du domaine R1, la contribution de fréquence plus élevée R2 est mise en évidence (figure 5a) et également décrite par un arc de cercle et une CC-fonction. R2 coupe l'axe réel à ρ_s (limite basse fréquence) et à ρ_{CLE} (limite haute fréquence). Les résistivités incrémentale $\Delta\rho_1$ et $\Delta\rho_2$ de R1 et R2 correspondent à l'interface échantillon / métallisation d'argent et aux résistances des jonctions entre clusters, respectivement. ρ_s et ρ_{CLE} correspondent aux résistivités d'échantillon et de cluster, respectivement. Par ailleurs, le zoom de la partie haute fréquence (GHz) du tracé de résistivité complexe permet de déterminer la résistivité effective des domaines sp^2 , ρ_{sp2e} (Fig. 5b). Cette dernière hypothèse est entièrement supportée par le comportement de type métallique observé dans cette gamme de fréquences (fig. 2a).

Des diagrammes de la résistivité similaires ont été obtenus pour tous les échantillons et toutes les températures, dans la gamme de 180 à 300K. Le tableau 2 résume l'ensemble des valeurs de conductivité à température ambiante. $\sigma_s = (\rho_s)^{-1}$ est la conductivité de l'échantillon, $\sigma_{CLE} = (\rho_{CLE})^{-1}$ correspond à la conductivité effective de cluster et $\sigma_{sp2e} = (\rho_{sp2e})^{-1}$ correspond à la conductivité effective des domaines sp^2 . Toutes les valeurs σ_{CLE} et σ_{sp2e} sont effectives car elles dépendent de la fraction volumique, sauf σ_s .

- Figure 5, page suivante -

Figure 5. (a) diagramme de Nyquist de la partie imaginaire $\rho''(v)$ vs la partie réelle $\rho'(v)$ de la résistivité complexe à 298 K pour CLFP3 (C-LiFePO₄), (b) zoom sur la partie haute fréquence du tracé (détermination de la conductivité effective des domaines sp^2). (c) Conductivités vs l'inverse de la température pour CLFP2 (d'échantillon avec sa métallisation d'argent ■, d'échantillon ■, de cluster ■ et de domaine sp^2 ■) et pour LFP (d'échantillon ■). (d) Conductivité effective des clusters vs conductivité effective des domaines sp^2 dans les différents échantillons.



La dépendance avec la température des différentes conductivités σ_s , σ_{CLe} et σ_{sp2e} est montrée dans la figure 5c. La conductivité quasi-indépendante de la température (absence d'énergie d'activation) pour σ_{sp2e} reflète le comportement métallique attendu pour les domaines de carbone sp^2 . Le comportement linéaire de $\ln \sigma$ vs T^{-1} montre une activation thermique simple des conductions de cluster d'échantillon dans la gamme de température 200-400K (tableau 2). Malgré les différentes valeurs de conductivités, les énergies d'activation sont similaires, $E_{CL} \approx E_s$ (**Table 2**). Cela indique que les porteurs de charge et les mécanismes de transport sont les mêmes depuis l'intérieur de l'enrobage jusqu'à l'ensemble de l'échantillon ; probablement parce que les contacts entre les clusters sont similaires à des goulets d'étranglement. Le transfert électronique au travers de l'échantillon résulte de saut (*hopping*) entre les domaines sp^2 de clusters adjacents, on observe en effet la même barrière de potentielle pour la conduction à l'échelle des clusters et de l'échantillon, mais le flux d'électrons y est limité en raison de la faible zone de contact entre les clusters.

En résumé, la Fig. 6a schématise la hiérarchie des chemins de conduction dans les échantillons de l'échelle sub-nanométrique (domaines sp^2) à l'échelle macroscopique (échantillon en contact avec le collecteur de courant) et les polarisations aux différentes échelles. La conductivité à l'échelle de l'échantillon est transport sur de très longues distance d'électrons sautant de domaine sp^2 en domaine sp^2 au-dessus des discontinuités sp^3 dans l'enrobage de carbone situé autour des grains de matière active et des clusters de grains. On a identifié aussi les goulets d'étranglement (impliquant des résistances de constriction et tunnel) aux jonctions inter-clusters. En complément (voir les explications plus loin), la Fig. 6b donne les limites hautes et basses des conductivités vraies aux différentes échelles.

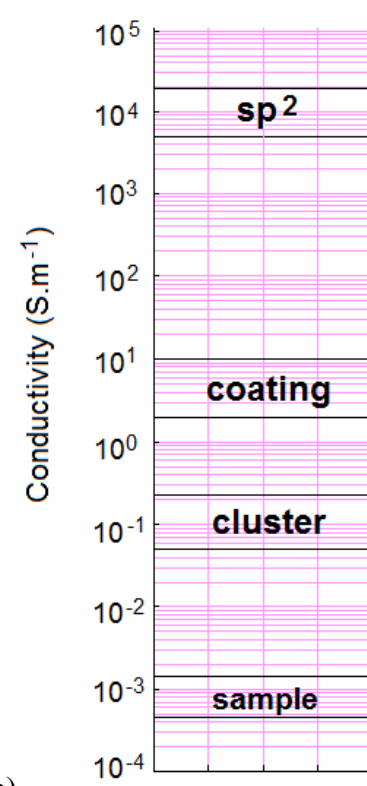
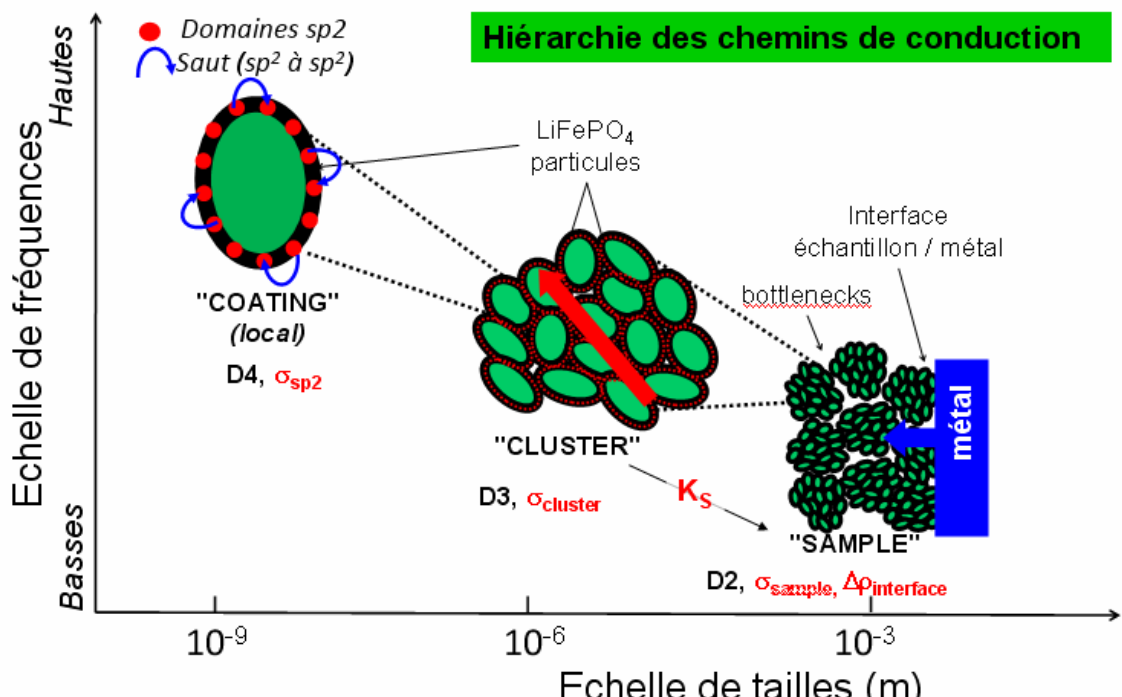


Figure 6. Description schématique (a) de l'architecture hiérarchique dans les échantillons donnant lieu à différentes sources de polarisations. (b) Les différents niveaux de conductivité vraie dans les matériaux nanocomposites C-LiFePO₄.

Nous pouvons considérer que la conductivité des clusters est régie par la conductivité σ_{CO} de l'enrobage car ce dernier est continu au sein des clusters. Leurs comportements électriques sont donc similaires, la conductivité de cluster correspondant à la valeur effective de la conductivité de l'enrobage, qui est principalement dépendant de la teneur en carbone sp^2 . De cette façon, la Fig. 5d montre une corrélation quasi-linéaire entre les conductivités (effectives) mesurées pour les clusters et les domaines sp^2 des différents échantillons à température ambiante (l'origine étant l'échantillon sans enrobage, c'est à dire avec une conductivité négligeable). Cette corrélation est donnée par

$$\sigma_{CLE} = C\sigma_{sp2e} \quad (2.8)$$

où σ_{sp2e} est la conductivité (effective) des domaines de carbone sp^2 , et C le coefficient de proportionnalité (la pente) avec une valeur d'environ 5×10^{-4} ($\pm 1 \times 10^{-4}$). Avec intuition, on remarque que ce paramètre C est égal à $\exp(-E_{CL}/kT)$ avec $E_{CL} \approx 0,19$ ($\pm 0,01$) eV, ce qui correspond à la valeur moyenne de l'énergie d'activation de la conductivité de cluster (tableau 2). L'équation (8) peut être réécrite ainsi de la manière suivante,

$$\sigma_{CLE} = \sigma_{sp2e} \exp\left(-\frac{E_{CL}}{kT}\right) \quad (2.9)$$

Comme déjà mentionné σ_{CLE} et σ_{sp2e} sont effectives. Par ailleurs, selon le résultat illustré à la figure 5c, un paramètre de $K_S < 1$ peut être introduit dans l'équation (9) pour définir la conductivité de l'échantillon σ_S par,

$$\sigma_S = K_S \sigma_{CLE} = K_S \sigma_{sp2e} \exp\left(-\frac{E_{CL}}{kT}\right) \quad (2.10)$$

$\sigma_S \ll \sigma_{CLE}$ et K_S rend compte de la baisse de conductivité en allant du microscopique (cluster) au macroscopique (échantillon) et caractérise les différents contacts entre les clusters avec leurs résistances de confection. [4] En bon accord, une valeur plus favorable de K_S est trouvée pour les échantillons avec une porosité plus faible, c'est à dire dans la situation où les contacts sont meilleurs entre les clusters (Tableau 2).

2.3. Détermination de la conductivité réelle aux différentes échelles de loi C-LiFePO₄.

Afin d'extraire les conductivités vraies à partir des valeurs effectives expérimentales, nous allons utiliser le modèle de *brick-layer* (BLM), qui est bien adapté pour décrire la structure des clusters dans les échantillons de C-LiFePO₄. Le BLM classique consiste à considérer des briques cubiques conductrices (correspondant aux cœurs des grains) entouré par un mortier résistif (correspondant aux joints de grains). De façon inverse, un cluster de C-LiFePO₄ se compose de particules résistives LiFePO₄ entourées par un enrobage de carbone conducteur. Dans ce cas, la conductivité vraie de cluster σ_{CL} est donnée par [48]

$$\sigma_{CL} = \left(1 - (1 - \phi_{cc})^{2/3}\right) \sigma_{CO} \quad (2.11)$$

σ_{CO} est la conductivité vraie de l'enrobage et ϕ_{cc} la fraction volumique de carbone. Comme $\phi_{cc} \ll 1$ (Tableau 1), l'équation (11) se simplifie à:

$$\sigma_{CL} = \frac{2}{3} \phi_{cc} \sigma_{CO} \quad (2.12)$$

Comme les échantillons étudiés sont poreux (tableau 1), il est donc nécessaire d'utiliser une loi de mélange pour exprimer la vraie valeur de la conductivité du cluster (soit σ_{CL}) à partir de la valeur mesurée (soit σ_{CLE}). La théorie générale des milieux efficaces moyennés (GEM) décrit comment calculer la conductivité d'un matériau poreux, c'est à dire composé d'une phase conductrice et de pores (isolants). La valeur effective de la conductivité de cluster σ_{CLE} peut être comparée à celui d'un milieu hypothétique compacte σ_{CL} (c'est à dire la vraie valeur de la conductivité du cluster):

$$\sigma_{CLE} = \sigma_{CL} \left(\frac{d - d_c}{1 - d_c} \right)^u \quad (2.13)$$

d est la fraction volumique de la phase conductrice (cluster), d_c est le seuil de percolation et u est un exposant critique. Pour les systèmes 3D (tridimensionnel), ϕ_c est généralement

comprise entre 0,10 et 0,40 et u entre 1,65 et 2. En utilisant les équations (12) et (13), la vraie valeur de la conductivité des domaines sp² (σ_{sp2}) peut être obtenue comme suit:

$$\sigma_{sp2} = \sigma_{sp2e} \frac{3}{2\phi_{cc}} \left(\frac{1-d_c}{d-d_c} \right)^u \quad (2.14)$$

σ_{sp2e} est la valeur effective des domaines sp² donnée dans le tableau 2. Considérant les valeurs moyennes $\phi_{cc} = 3.5 \times 10^{-2}$, $d = 0,56$ et $\sigma_{sp2e} = 37 \text{ S.m}^{-1}$, les valeurs limites inférieures et supérieures de la conductivité des domaines sp² sont $\sigma_{sp2} = 5 \times 10^3 \text{ S.m}^{-1}$ et $\sigma_{sp2} = 2.2 \times 10^4 \text{ S.m}^{-1}$ à température ambiante, respectivement. Ces valeurs sont un ordre de magnitude inférieures aux valeurs expérimentales rapportées pour la conductivité du graphite. [49] En utilisant l'équation (13) avec les mêmes paramètres, les valeurs inférieures et supérieures des limites de la vraie conductivité du cluster sont $\sigma_{CL} = 0,05 \text{ S.m}^{-1}$ et $\sigma_{CL} = 0,23 \text{ S.m}^{-1}$ à température ambiante, respectivement. De la même manière, les équations (12) et (13) donnent les valeurs inférieures et supérieures des limites de la conductivité vraie de l'enrobage σ_{CO} , qui sont égales à 2 et 0,1 S.m^{-1} à température ambiante, respectivement.

Les valeurs vraies de la conductivité aux différentes échelles sont reportées dans la figure 6b. Finalement, une expression peut être donnée pour décrire la conductivité de l'échantillon en combinant les équations (10) et (14), qui est

$$\sigma_s = K_s \left(\frac{d-d_c}{1-d_c} \right)^u \frac{2\phi_{CC}}{3} \sigma_{sp2} \exp \left(-\frac{E_{CL}}{kT} \right) \quad (2.15)$$

L'expression (15) donne une relation entre les niveaux macroscopique (l'échantillon) et microscopiques (domaines sp²) pour la conductivité et fait intervenir les paramètres décrivant la texture des échantillons.

3. Conclusions

La spectroscopie diélectrique à large bande (BDS) a été utilisée pour une caractérisation détaillée des propriétés électriques des matériaux nanocomposites C-LiFePO₄ utilisés dans les batteries au lithium. Lorsque la fréquence augmente, différentes relaxations diélectriques apparaissent dans l'ordre suivant: a) la polarisation de charge d'espace (basse fréquence

étendue) à l'interface entre l'échantillon et la couche conductrice métallique déposé sur celui-ci; b) Polarisation de clusters C-LiFePO₄ (échelles microniques et / ou submicroniques) en raison de l'existence de jonctions résistive entre eux; c) sauts d'électrons entre les domaines sp² (échelle nanométrique) dans l'enrobage de carbone autour des particules de LiFePO₄. L'utilisation du modèle *brick-layer* et de la théorie générale des milieux effectifs moyennés a permis de donner les ordres de grandeur pour les vraies valeurs de la conductivité aux différentes échelles des nanocomposites. Les résultats montrent que les limitations principales au transport électronique dans C-LiFePO₄ sont premièrement dues aux discontinuités sp³ dans l'enrobage de carbone où il est observé une chute de conductivité de trois ordres de grandeur. Deuxièmement, les contacts inter-cluster induisent une chute de conductivité de deux ordres de grandeur, (Fig. 6b). En raison de la percolation du revêtement de carbone au sein des clusters, la chute de la conductivité dans le cluster est minime, inférieure à un ordre de grandeur.

4. Partie expérimentale

Matériaux et des échantillons:

Des matériaux LiFePO₄ avec et sans enrobage de carbone (0-4% en %m en carbone), avec des tailles de particules entre 50 et 150nm ont été fournis par UMICORE Cobalt & Specialty Materials, en Belgique. Des pastilles cylindriques sont préparées par compaction des poudres de C- LiFePO₄ à 510 MPa en utilisant un pastilleur (Canaple Ets). Des contacts métalliques sont faits en appliquant une peinture conductrice d'argent ou d'or (Oxford Instruments) directement sur les deux faces de la pastille.

Caractérisation:

Des observations de microscopie électronique à balayage (MEB) ont été réalisées sur les pastilles après métallisation par pulvérisation à l'or-palladium en utilisant un appareil JEOL JSM 7600F. Des études de microscopie électronique à transmission haute résolution (HRTEM) ont été réalisées avec TEM (FEG) Hitachi HF2000 possédant un canon à émission de champ exploité à 200 kV, et les spectres ont été enregistrés en utilisant un détecteur modifié GATAN 666 parallèle, équipé d'une caméra CCD. Pour cela, les poudres ont été dispersées dans l'acétone, déposées sur une grille de carbone trouée, puis placées sur un porte

échantillon. Préalablement à son introduction dans le microscope, le porte-échantillon contenant la poudre a été placé sous vide à 80°C pendant une heure pour éliminer la contamination de surface. Un XPS (Kratos Axis Ultra DLD) a été utilisé pour quantifier les teneurs en carbone de type sp² et sp³. Pour cela, la poudre de l'échantillon a été déposée sur le porte-échantillon sur lequel un scotch de carbone est placé. Le traitement des données est effectué en utilisant le logiciel Casa. Les spectres pour le carbone de type sp² a été calibré à l'énergie de liaison de référence d'environ 284,5 et le fit sur le pic du carbone de type sp² est réalisé en utilisant une référence.

Mesures de Spectroscopie Diélectrique Large Bande (BDS) :

Les spectres de résistivité et de permittivité complexes ont été enregistrés sur une large plage de fréquences de 40 à 10¹⁰ Hz, en utilisant simultanément un analyseur d'impédance (Agilent 4294 de 40 à 1.1x10⁸ Hz) et un analyseur de réseau (HP 8510 à partir 4.5x10⁷ à 10¹⁰Hz). Le dispositif expérimental, entièrement décrit dans les travaux précédents, [51,52] est constitué d'une cellule coaxiale (APC7 standard) dans laquelle l'échantillon de forme cylindrique métallisé avec de l'argent sur ses deux faces est plaquée entre le conducteur interne et un court-circuit. L'échantillon a le même diamètre (7 mm) que celui du conducteur extérieur de la cellule coaxiale. Après un étalonnage pertinent de l'analyseur, la permittivité complexe de l'échantillon $\epsilon(\omega) = \epsilon'(\omega) - i\epsilon''(\omega)$ est calculé à partir de son admittance Ys. Les spectres diélectriques complets ont été faits à partir d'environ 400 mesures avec une précision d'environ 3 à 5% dans la gamme de fréquences expérimentales. Les mesures de température ont été faites sous un flux N₂ sec dans la gamme de 200 à 400 K.

5.Références bibliographiques

- ¹ V. Srinivasan, J. Newman, *J. Electrochem. Soc.* **151** (2004) A1517.
- ² D. Guy, B. Lestriez, D. Guyomard, *Adv. Mater. (Weinheim, Ger.)*, **16**, 553 (2004).
- ³ B. Lestriez, *C. R. Chimie* **13** (2010) 1341.
- ⁴ D. E. Stephenson, E. M. Hartman, J. N. Harb, and D. R. Wheeler, *J. Electrochem. Soc.*, **154**, A1146 (2007).
- ⁵ J-M. Atebamba, J. Moskon, S. Pejovnik, and Miran Gaberscek, *J. Electrochem. Soc.* **157** (2010) A1218.
- ⁶ Y.-H. Chen, C.-W. Wang, X. Zhang, A.M. Sastry, *J. Power Sources* **195** (2010) 2851.
- ⁷ S. Dargaville and T.W. Farrel, *J. Electrochem. Soc.* **157** (2010) A830.
- ⁸ M. Ender, J. Joos, T. Carraro, E. Ivers-Tiffée, *Electrochem. Commun.* **13** (2011) 166–168
- ⁹ J.R. Wilson, J.S. Cronin, S.A. Barnett, S.J. Harris, *J. Power Sources* **196** (2011) 3443.
- ¹⁰ Lei, J., McLarnon, F., Kostecki, R., *J. Phys. Chem. B* **109** 952-957 (2005)
- ¹¹ J. Liu, M. Kunz, K. Chen, N. Tamura, and T.J. Richardson, *J. Phys. Chem. Lett.* **2010**, **1**, 2120
- ¹² M. Park, X. Zhang, M. Chung, G.B. Less, A.M. Sastry, *J. Power Sources* **195** (2010) 7904
- ¹³ J.C. Badot, E. Ligneel, O. Dubrunfaut, D. Guyomard, B. Lestriez, *Adv. Funct. Mater.*, **19**, 2749 (2009).
- ¹⁴ A. von Hippel, *Dielectrics and Waves* (Wiley, New York, 1952).
- ¹⁵ C.F.J. Böttcher and P. Bordewijk, *Theory of electric polarization, Vol. II: Dielectric in time-dependent fields*, 3rd edition, Elsevier, 1996.
- ¹⁶ A. K. Padhi, K. S. Nanjundaswamy, J.B. Goodenough, *J. Electrochem. Soc.*, **144** (1997) 1188.
- ¹⁷ T. Maxish, F. Zhou, and G. Ceder, *Phys. Rev. B*, **73** (2006) 104301.
- ¹⁸ K. Zaghib, A. Mauger, J.B. Goodenough, F. Gendron, and C.M. Julien, *Chem. Mater.*, **19** (2007) 3740.
- ¹⁹ C. Delacourt, L. Laffont, R. Bouchet, C. Wurm, J.-B. Leriche, M. Morcrette, J.-M. Tarascon, and C. Masquelier, *J. Electrochem. Soc.* **152** (2005) A913.
- ²⁰ R. Amin, P. Balaya, J. Maier, *Electrochem. Solid-State Lett.* **9** (2007) A13
- ²¹ M.M. Doeff, Y. Hu, F. McLarnon, R. Kostecki, *Electrochem. Solid State Lett.*, **6** (2003) A207
- ²² A. Salah, A. Mauger, K. Zaghib, J. B. Goodenough, N. Ravet, M. Gauthier, F. Gendron, and C. M. Julien, *J. Electrochem. Soc.*, **153**, A1692 (2006).
- ²³ J. Roberston, E.P. O'Reilly, *Phys. Rev. B*, **35** (1987) 2946.

- ²⁴ N.A. Marks, D.R. McKenzie, B.A. Pailthorpe, M. Bernasconi, M. Parrinello, Phys. Rev. Lett., 76 (1996) 768.
- ²⁵ N. Ravet, A. Abouimrane, M. Armand, Nature Mater., 2 (2003) 702.
- ²⁶ Y. Hu Y, M.M. Doeff, R. Kostecki, R. Finones, J. Electrochem. Soc. 151 (2004) A1279
- ²⁷ R. Dominko, M. Bele, M. Gaberscek, M. Remskar, D. Hanzel, S. Pejovnik, J. Jamnik, J. Electrochem. Soc., 152 (2005) A607
- ²⁸ J. Mozkon, R. Dominko, M. Gaberscek, R. Cerc-Korosec, J. Jamnik, J. Electrochem. Soc., 153 (2006) A1805
- ²⁹ M. Maccario, L. Croguennec, B. Desbat, M. Couzi, F. Le Cras, L. Servant, J. Electrochem. Soc. 155 (2008) A879
- ³⁰ M. Koos, S.H.S. Moustafa, E. Szilagyi, I. Pocsik, Diamond. Relat. Mater., 8 (1999) 1919.
- ³¹ D.I. Jones and A.D. Stewart, Phil. Mag. B, 46 (1982) 423.
- ³² J.P. Sullivan, T.A. Friedman, *Electronic transport in amorphous carbon*, 1997 Dec 01, Report Number(s) SAND-97-1903C; CONF-9707129-, available at [ww.osti.gov/bridge/product.biblio.jsp?osti_id=555540](http://www.osti.gov/bridge/product.biblio.jsp?osti_id=555540)
- ³³ D. Dasgupta, F. Demichelis, A. Tagliaferro, Phil. Mag. B, 63 (1991) 1255.
- ³⁴ M.M. Doeff, J.D. Wilcox, R. Yu, A. Aumentado, M. Marcinek, R. Kostecki, J Solid State Electrochem., 12 (2008) 995
- ³⁵ J.D. Wilcox, M.M. Doeff, M. Marcinek, R. Kostecki, J. Electrochem. Soc. 154 (2007) A389
- ³⁶ S. Urbonaite, S. Wachtmeister, C. Mirquet, E. Coronel, W.Y. Zou, S. Csillag, G. Sevenson, Carbon 45 (2007) 2047
- ³⁷ P. Moreau, F. Boucher, G. Goglio, D. Foy, V. Mauchamp, and G. Ouvrard, Phys Rev B, 73 (2006) 195111
- ³⁸ E. Riedo, F. Comin, J. Chevrier, F. Schmithusen, S. Decossas, M. Sancrotti, Surf. Coat. Technol. 125 (2000) 124.
- ³⁹ J. Díaz, G. Paolicelli, S. Ferrer, F. Comin, Phys. Rev., B, 54 (1996) 8064.
- ⁴⁰ M. Raybachuk, J.M. Bell, Thin solid films, 515(2007)7855
- ⁴¹ Mott N. F.; Davis, E. A. In *Electronic Processes in Non-Crystalline Materials*, 2nd Ed.; Oxford University Press, Oxford, 1979.
- ⁴² R. Pelster, G. Nimtz, B. Wessling, Phys. Rev. B , 49 (1994) 12718
- ⁴³ C. Chiteme and D.S. McLachlan, Physica B 279 (2000) 69
- ⁴⁴ J. Mozkon, R. Dominko, R. Cerc-Korosec, M. Gaberscek, J. Jamnik, J. Power Sources, 174 (2007) 683

- ⁴⁵ B. Sun, P.E. Colarita, H. Kim, M. Lockett, M.S. Marcus, L.M. Smith, R.J. Hamers, Langmuir **2006**, 22, 9598.
- ⁴⁶ M-S. Cao, W-L. Song, Z-L. Hou, B. Wen, J. Yuan, Carbon 48 (2010) 788
- ⁴⁷ M.S. Islam, D.J. Driscoll, C.A.J. Fisher, and P.R. Slater, Chem. Mater., 17 (2005) 5085.
- ⁴⁸ S.M. ten Grotenhuis, M.R. Drury, C.J. Spiers, and C.J. Peach, J. Geophys. Res. 110 (2005) B12201
- ⁴⁹ X. Wang, L. Zhi, K. Mullen, Nano Lett. 8 (2008) 324.
- ⁵⁰ N.E. Belhadj-Tahar, A. Fourrier-Lamer, IEEE Trans. Microwaves Theory and Tech., 34 (1986) 346.
- ⁵¹ S. Berthumeyrie, J.C. Badot, J.P. Pereira-Ramos, O. Dubrunfaut, S. Bach, and Ph. Vermaut, J. Phys. Chem. C, 114 (2010) 19803.

General Introduction

A lithium-ion battery also known as Li-ion battery or LiB is a family of [rechargeable battery](#) types using no lithium metal at the negative electrode in which [lithium](#) ions move from the negative [electrode](#) to the positive electrode during discharge, and back when charging (Figure 1). Chemistry, performance, cost, and safety characteristics vary across LiB types. Unlike lithium [primary batteries](#) (which are disposable), lithium-ion [electrochemical cells](#) use an intercalation lithium compound as the electrode material instead of metallic lithium. Lithium-ion batteries are common in [consumer electronics](#). They are one of the most popular types of rechargeable batteries for [portable electronics](#), with one of the best [energy densities](#), no [memory effect](#), and a slow [loss of charge](#) when not in use. Beyond consumer electronics, LiBs are also growing in popularity for military, [electric vehicle](#), and [aerospace](#) applications. Research is yielding a stream of improvements to traditional LiB technology, focusing on energy density, durability, cost, and [intrinsic safety](#).

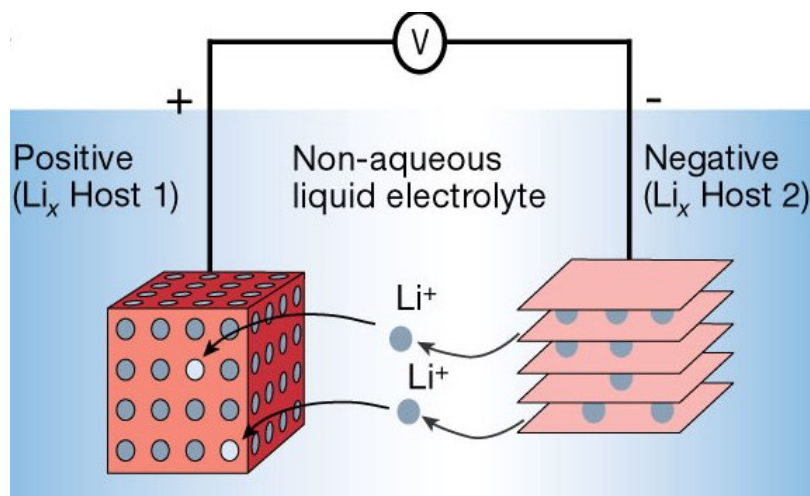


Figure 1. The operating principle of a lithium ion battery [1]

Positive electrodes for Li-ion and lithium metal batteries (also termed “cathodes”) have been under intense scrutiny since the advent of the Li-ion cell in 1991. This is especially true in the past decade. Early on, carbonaceous materials dominated the negative electrode and hence most of the possible improvements in the cell were anticipated at the positive terminal; on the other hand, major developments in negative electrode materials made in the last portion of the decade with the introduction of nanocomposite Sn/C/Co alloys and Si-C composites have demanded higher capacity positive electrodes to match. Much of this was

[1]. J.-M. Tarascon & M. Armand, Nature,(2001) 414, 359-367

driven by the consumer market for small portable electronic devices. There has been a step change in the approach to energy storage following the discovery of LiCoO₂ as a positive electrode, and the commercialization of the Li-ion battery by Sony [2,3]. Since then layered lithium transition metal oxides arguably represent the most successful category of positive electrode, comprising compounds with formula of LiMO₂ (M: Mn, Co, and Ni) that crystallize in a layered structure. This topology offers highly accessible ion diffusion pathways. Much more recently, there is a growing interest in developing Li-sulfur and Li-air batteries, which have the potential for vastly increased capacity and energy density that could reach levels needed in large-scale power systems [4]. However, considerable interest in a new class of transition metal phosphate materials was sparked by the introduction of LiFePO₄ as a cathode material about 10 years ago. After the demonstration of its electrochemical activity by Padhi *et al.* ten years ago [5], LiFePO₄ is now commercialized as a main active material of new generation lithium-ion batteries positive electrodes. Not only is the material (LiFePO₄) relatively inexpensive and available in nature, but it is also less toxic compared to cobalt, nickel, or manganese. In addition, the operating voltage of the electrode ~3.4 V vs. Li is ideal for maximizing energy while minimizing side reactions due to electrolyte decomposition. Finally, the high theoretical specific energy ~580 Wh/kg makes it a very attractive candidate as a positive electrode in cells. However, these positive aspects are counteracted by the low electronic conductivity of the material, which is thought to result in considerable ohmic drops within the electrode. In addition, it has been noted that the electrode displays limited high-rate capability, with considerable loss in utilization with increase in current, suggesting transport limitations. Various ideas have been proposed and tested to alleviate these two problems, with the most successful being the reduction of the particle size to reduce transport losses and the coating of the particles with a layer of carbon to improve the conductivity of the solid phase. Recently, efforts to introduce dopant ions into the lattice have been shown to be very successful for improving the conductivity, and consequently the performance, of the material [5].

[2]. Mitzushima, K. Jones, P. C. Wiseman, P. J. Goodenough, J. B. Mater. Res. Bull. 1980, 15, 783.

[3]. Nagaura, T. Tozawa, K. Prog. Batteries Sol. Cells 1990, 9, 209.

[4]. Brian L. Ellis, Kyu Tae Lee, and Linda F. Nazar, Chem. Mater. 2010, 22, 691–714.

[5]. A. K. Padhi, K. S. Nanjundaswamy, J.B. Goodenough, J. Electrochem. Soc., **144** (1997) 1188.

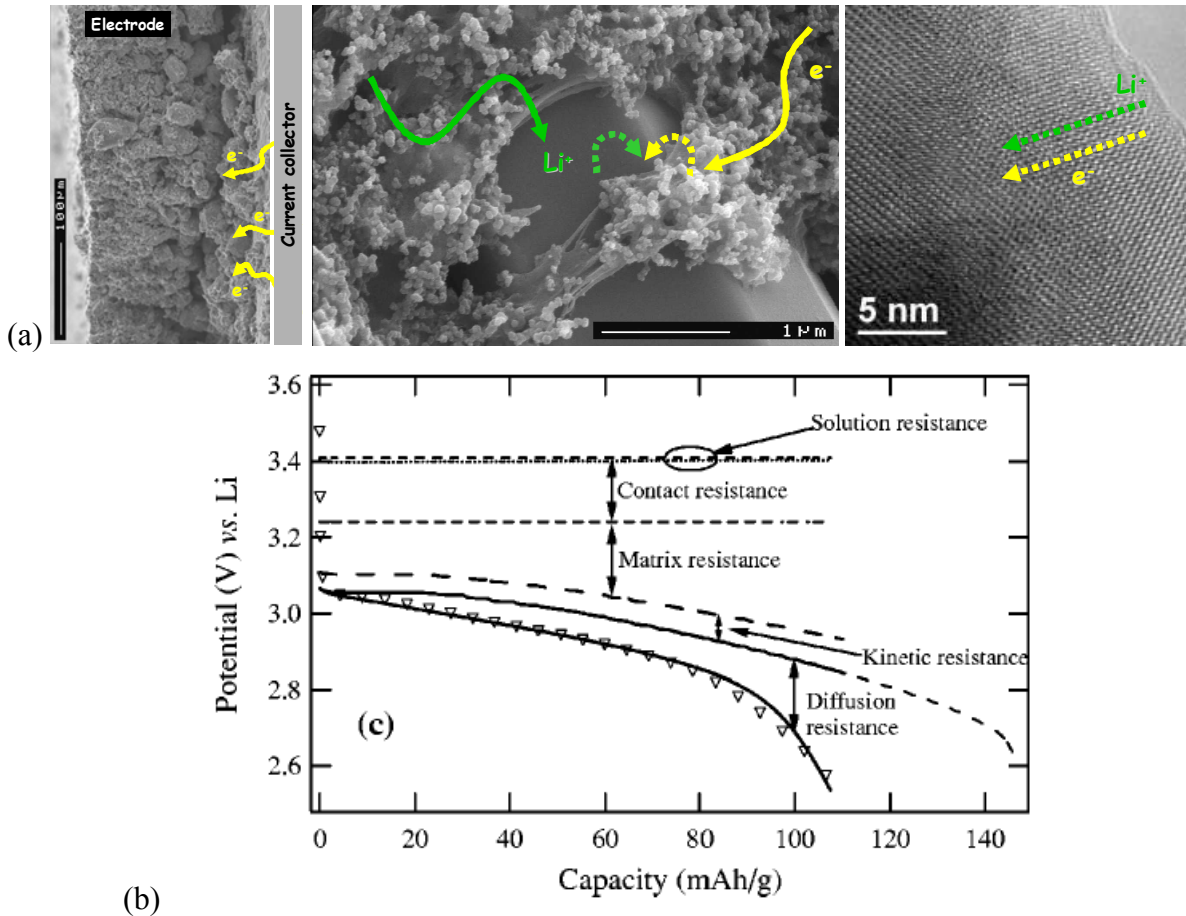


Figure 2. (a) SEM and TEM pictures of a composite electrode with its current collector highlighting the different scales and schematically all the different architectural features involved in the electronic transport as well as some involved in the ionic one: the current collector/composite electrode interface; the conductive additive/binder porous matrix impregnated by the liquid electrolyte; the active material/matrix interface; the solid-state mass transport. (b) Estimation of the potential drops in the iron-phosphate electrode at a current density of 2.6 mA/cm². The graph shows the contributions that result in the potential deviating from that of the open-circuit: the contact resistance at the current collector/composite electrode interface; the resistance of the conductive additive/binder porous matrix; the kinetic resistance at the active material/matrix interface; the diffusion resistance to solid-state mass transport [6].

Positive and negative electrodes are however composite electrodes. The composite electrode is a very complex medium obtained by mixing together the active material (AM) grains with non-electro active additives such as a conducting agent (C) and a polymeric binder (B) (Figure 2). For high rate performance this medium needs to bring very efficiently the ions and the electrons to the surface of the active material (AM) particles. The choice of the non-electroactive additives and the processing of the composite electrode are both very important to reach optimal performance of the composite electrode. For battery optimum

[6]. V. Srinivasan, and J. Newman, J. Electrochem. Soc, 151 (2004) A1517.

energy density, the amount per unit mass and volume of the non-electroactive additives need however to be minimized [7]. In order to meet the preset targets a very efficient active material (AM), an optimum formulation and a very good processing conditions are compulsory. The composition and architecture of the composite electrode should be able to allow an efficient electrical conductivity which enables sufficient cycle life for the battery especially for high rate applications like EV and HEVs (Figure 2).

As stated above, there exists a strong demand for the development of new batteries with improved performance with respect to state-of-the-art lithium-ion cell technology. To reach this goal, an increased fundamental understanding of the factors that limit electrochemical performance is required. This is very challenging, however, because these materials are composites and hierarchical structures [8,9]. In any type of composite material, the chemical composition and the microstructure (dispersion of active material, conductive additive and polymeric binder, porosity...) determine the global electrode performance (energy density, power, cyclability). To date, the effects of microstructure characteristics are usually described by effective macro-homogeneous models that assume electrodes are homogeneous, isotropic and flawless [6]. However, composite electrodes are hierarchical architectures with different levels: a) macroscopic (substructure of porous clusters); b) mesostructural (particles constituting the clusters); c) subnanometric (inside the particles or crystallites). The identification of the key parameters across all observed size scales is required. There has been a number of recent modelling efforts aimed at including more detailed microstructural information [10,11,12,13]. All these models would benefit from direct microstructural data. New techniques must be developed to reach this goal [14,15,16,17]. The electronic conductivity is one of the two major properties (the other one being ionic conductivity) of the composite electrode with respect to its electrochemical behaviour [18]. However, there is no modelling of the electronic conductivity within composite electrodes because the dc conductivity, σ_{dc} , has been the only measured quantity to

-
- [7]. B. Lestriez, C. R. Chimie 13 (2010) 1341.
 - [8]. D. Guy, B. Lestriez, D. Guyomard, Adv. Mater. (Weinheim, Ger.), **16**, 553 (2004).
 - [9]. B. Lestriez, C. R. Chimie 13 (2010) 1341.
 - [10]. D. E. Stephenson, E. M. Hartman, J. N. Harb, and D. R. Wheeler, J. Electrochem. Soc., **154**, A1146 (2007).
 - [11]. J-M. Atebamba, J. Moskon, S. Pejovnik, and Miran Gaberscek, J. Electrochem. Soc. **157** (2010) A1218.
 - [12]. Y.-H. Chen, C.-W. Wang, X. Zhang, A.M. Sastry, J. Power Sources **195** (2010) 2851.
 - [13]. S. Dargaville and T.W. Farrel, J. Electrochem. Soc. **157** (2010) A830.
 - [14]. M. Ender, J. Joos, T. Carraro, E. Ivers-Tiffée, Electrochim. Commun. **13** (2011) 166–168.
 - [15]. J.R. Wilson, J.S. Cronin, S.A. Barnett, S.J. Harris, J. Power Sources **196** (2011) 3443.
 - [16]. Lei, J. McLarnon, F.Kostecki, R. J. Phys. Chem. B **109** 952-957 (2005).
 - [17]. J. Liu, M. Kunz, K. Chen, N. Tamura, and T.J. Richardson, J. Phys. Chem. Lett. **2010**, **1**, 2120.
 - [18]. M. Park, X. Zhang, M. Chung, G.B. Less, A.M.Sastry, J. Power Sources **195** (2010) 7904.

date. σ_{dc} is a macroscopic averaged value which gives poor information on the electrical transport properties of granular materials, such as composite electrodes, constituted of clusters of particles (eventually) and particles separated by resistive and capacitive barriers (e.g. cluster or particle boundaries), that limit the charge transports in the material.

Hence, this PhD thesis is dedicated to the fundamental understanding of the electronic conductivity. The objective is to extract the electronic conductivity of a composite electrode at all the scales of its architecture (from inter atomic distances to macroscopic lengths), with the aim of pin pointing the limiting parameters and move on to systematic and rational manufacturing, processing and engineering practices for the better. To achieve our goal, we will use an original but pertinent technique, the broadband dielectric spectroscopy (BDS) to be discussed in a separate chapter 1. The variation of the electronic conductivity at all scales of a LiFePO₄ composites as function of the particle size, coating quantity and quality, binder loading and so on will be studied. The study will be carried out in such a way that a step by step approach is followed. Pellets of binary systems (LiFePO₄/carbon coating) will be studied first to establish the fundamental knowhow on the electrical properties of the different scales and the existing correlation between the scales of a compacted powder. Then follows the ternary systems (LiFePO₄/carbon coating/binder) in which we will try to establish the role of the binder and scales affected due to the introduction of the binder. Of course the correlation of the findings with the electrochemical properties is always the ultimate goal.

Chapter 1: Background

1. Introduction

This PhD manuscript is organized in three chapters of logical order. The first chapter will introduce the definition of the selected technique and will try to answer the question what is it like to use the dielectric spectroscopy as a technique to asses electrical properties. To facilitate easy understanding of results in the later chapters, the necessary theoretical, phenomenological and experimental aspect of the technique will be introduced. A summary of the already performed works implementing the technique is presented to show the scope and the kinds of information accessible. In addition, processes like conduction mechanisms in carbon which we will make use of in the later chapters, will be briefly introduced. To complete the picture, we will wrap up the chapter with a short summary on the State of the art about the understanding of the electronic properties of composite electrodes for lithium batteries.

2. The Broadband Dielectric Spectroscopy (BDS)

2.1. Introduction

The Broadband Dielectric Spectroscopy (BDS) is a technique to measure the [dielectric](#) properties of a medium as a function of [frequency](#) [19]. It is based on the interaction of an external electromagnetic field with the electric [dipole moments](#) of the sample, often expressed by [permittivity](#). This technique measures the [complex](#) permittivity of a system over a range of frequencies, and therefore the frequency response of the system, including the energy storage and dissipation properties, is revealed.

Relaxation is a process, which is strictly applied to linear systems whose response and stimulus are proportional to one another in equilibrium. Relaxation is a delayed response to a changing stimulus in such a system. The dielectric relaxation occurs in dielectrics that are in insulating materials with negligible or small electrical conductivity. The stimulus is almost always an electric field, the response a polarization. The time lag between field and polarization implies an irreversible degradation of free energy to heat.

[19]. F. Kremer, A. Schonhals, W. Luck, *Broadband Dielectric Spectroscopy*. – Springer-Verlag, 2002

When the dielectric relaxation of a given material has been measured the investigator is in a position of a man presented with a black box which has two terminals. He may apply alternating fields of various kinds and he may heat the box but he is not allowed to look inside and he finds that the box responds as if it contained a combination of capacitors and resistors. The reaction of our presenter to the puzzle presented by the black box will differ according to whether he is a mathematician, electrical engineer, physicist or chemist. The mathematician will be satisfied by a description in terms of differential equations and the engineer by an equivalent circuit. However the physicist and the chemist will want an interpretation in terms of the structure of the material whose response can be represented by the black box.

The structural interpretation of dielectric relaxation is a difficult problem in statistical thermodynamics. It can for many materials be approached by considering dipoles of molecular size whose orientation or magnitude fluctuates spontaneously, in thermal motion. Mechanisms of dielectric relaxation are often subtle and complicated. Most of the cases where satisfactory physical interpretations have been achieved, have in common that dielectric measurement were not used in isolation but were complemented by other physical or chemical techniques. Only in this way was it possible to decide between the multiplicities of physical models which might satisfy the dielectric data. Dielectric relaxation as a subject is neither self-contained nor self checking [20].

Before going further, we found it necessary to lay the necessary theoretical and phenomenological foundation in relation to the technique to show the potential of the technique and its justified application to the study of electronic transport in composites based on C-LiFePO₄.

2.2. Theoretical and phenomenological aspect of the technique.

When a static electric field is applied to a non-magnetic conductive material, an electric current density and / or polarization will be created within it. Denoting χ and ϵ the electric susceptibility and the relative permittivity of the medium, the polarization \vec{P} is directly related to the electric field \vec{E} by the relation.

$$\vec{P} = \epsilon_0 \chi \vec{E} = \epsilon_0 (\epsilon - 1) \vec{E} \quad (1.1)$$

[20]. V. Vera Daniel, Dielectric relaxation, Academic press, 1967

where $\epsilon_0 = 8.842 \times 10^{-12} \text{ F.m}^{-1}$ is the vacuum permittivity. However, the dielectric displacement is written as follows:

$$\vec{D} = \epsilon_0 \vec{E} + \vec{P} \quad (1.2)$$

where \vec{D} is the dielectric displacement that represents the component of an electric field associated solely with the presence of separated free electric charges, purposely excluding the contribution of bound electric charges in neutral atoms or molecules. Thus, the dielectric displacement is related to the electric field by the expression:

$$\vec{D} = \epsilon_0 \epsilon \vec{E} \quad (1.3)$$

On the other hand, the (static) current density \vec{J}_c is related to the electric field and the static conductivity of the medium σ_{dc} by Ohm's law:

$$\vec{J}_c = \sigma_{dc} \vec{E} \quad (1.4)$$

If the electric field is time-dependent, the total current density is given by:

$$\vec{J} = \vec{J}_c + \vec{J}_d \quad (1.5)$$

where $\vec{J}_d = \frac{\partial \vec{D}}{\partial t}$ (Maxwell-Ampère law).

In the frame of a harmonic excitation with a pulsation ω and a non-magnetic material, we can use complex quantities such as

- Permittivity: $\epsilon(\omega) = \epsilon' - i\epsilon'' \quad (1.6)$

- Conductivity: $\sigma(\omega) = \sigma' + i\sigma'' \quad (1.7)$

The imaginary part ϵ'' of the permittivity also known as "dielectric loss" corresponds to the dielectric absorption. As per the previous relationships, the total current density can be written as:

$$\vec{J} = \sigma_{dc}\vec{E} + i\omega\vec{D} = [\sigma_{dc} + i\omega\epsilon_0\epsilon(\omega)]\vec{E} = \sigma(\omega)\vec{E} \quad (1.8)$$

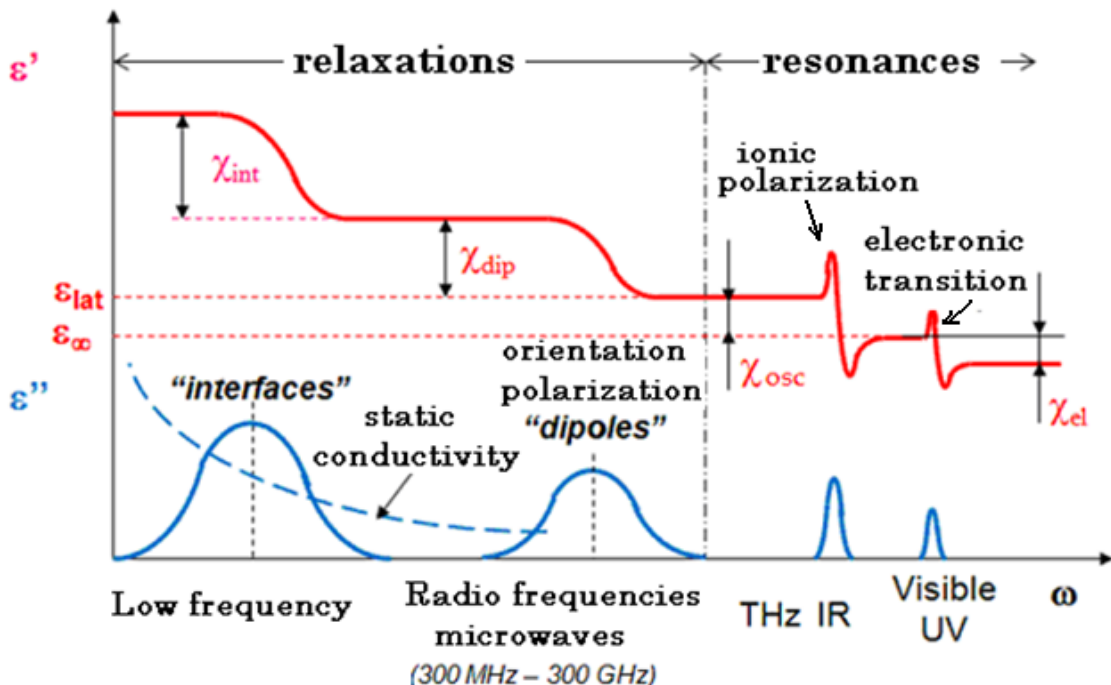
From the expression 1.8, the total complex conductivity is related to the permittivity by the following expression,

$$\sigma(\omega) = i\omega\epsilon_0\epsilon(\omega) + \sigma_{dc} \quad (1.9)$$

The frequency dependent conductivity (real part) is then given by

$$\sigma' = \sigma_{dc} + \omega\epsilon_0\epsilon''(\omega) = \sigma_{dc} + \sigma_{ac} \quad (1.10)$$

σ_{ac} is the alternating-current conductivity proportional to the dielectric losses. As the frequency approaches to 0, the conductivity stabilizes at a value of σ_{dc} when the material is conductive. Going from high to low frequencies, there are four major types of polarizations in inorganic solids: electronic polarization, ionic polarization, orientation polarization and interfacial polarization (Figure 1). The electronic polarization is due to contributions such as electronic interband transitions in semiconductors and the deformation of existing electron clouds around the nuclei. Typical frequencies of these resonant phenomena are located in the UV-visible range. At the larger scale, the ionic polarization is due to lattice oscillations (optical phonons) which give rise to resonances in the infrared (IR) range. In the region of radio frequencies and microwaves, orientation polarization can be due to dipole rotations (e.g. the rotation of water molecules in hydrates) and/or local movements of charges at the molecular and/or interatomic scales (e.g. charge transfer by hopping on interatomic distances or at the nanometer scale). These phenomena are generally visible by the BDS because they involve changes in local charge density. Finally, at the micro structural scale, a conducting polycrystalline material (compact powders, ceramics) presents interfacial polarizations. The interfaces are generally grain (particles) boundaries or more often, the contact area between the grains.



ϵ_{lat} = lattice permittivity

$$\epsilon_{\infty} = n^2$$

Figure 1. Typical evolution of the real and imaginary parts of the complex permittivity versus frequency for an inorganic solid [21].

If the grains (particles) are assembled into clusters (i.e. agglomerates), there exists a different interface between clusters. In addition, an interface exists between the sample and the electrodes contact (e.g., gold, silver) used for the measurement. These types of polarization are visible only at low frequencies. The characteristic frequencies of the different phenomena observed in dielectric spectroscopy are classifiable according to the characteristic scale at which they are observed. Furthermore, the larger characteristic size the smaller the characteristic frequency is (Figure 2).

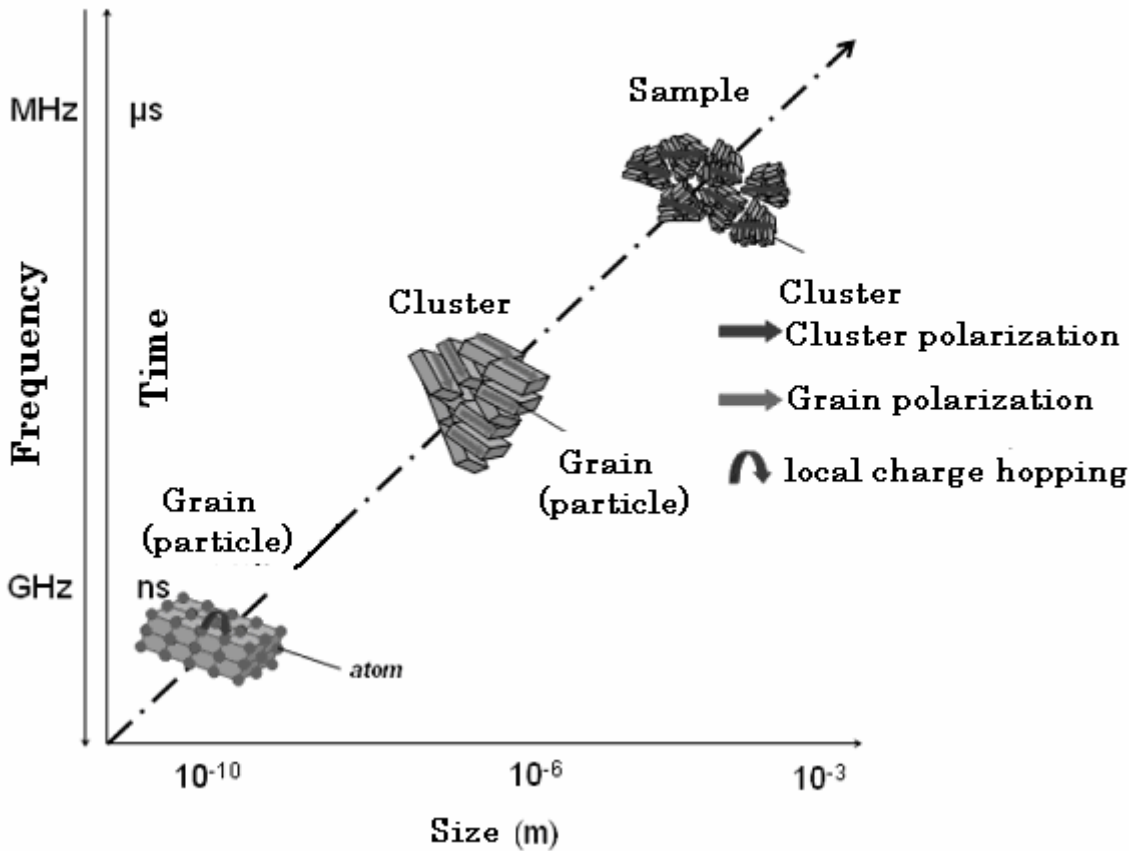


Figure 2. Multi-scale analysis of electric polarization in a conducting material [21].

This observation will be used directly for the allocation of different relaxations mainly due to electrons in C-LiFePO₄. These phenomena are generally described using the empirical Cole-Cole (CC) function. [22]

$$\varepsilon(\omega) = \varepsilon_{HF} + \frac{\varepsilon_{LF} - \varepsilon_{HF}}{1 + (i\omega\tau)^{1-\alpha}} \quad (1.11)$$

where τ is the relaxation time, the relaxation frequency being $v_r = (2\pi\tau)^{-1}$. α is a parameter between 0 and 1, which signifies the existence of a distribution of the relaxation time (frequency) centered at τ (or v_r). When $\alpha = 0$, the Debye function is obtained with a single relaxation time (frequency). ε_{LF} and ε_{HF} are the low- and high-frequency limits of the permittivity, i.e. when $\omega\tau \ll 1$ and $\omega\tau \gg 1$ respectively. The strength of the relaxation is

[21]. J.C. Badot, E. Ligneel, O. Dubrunfaut, D. Guyomard, B. Lestriez, Adv. Funct. Mater., 19 (2009) 2749
[22]. A. von Hippel, Dielectrics and Waves (Wiley, New York, 1952).

defined by $\Delta\epsilon = (\epsilon_{LF} - \epsilon_{HF})$. In the Nyquist plot as shown below in Figure 3, the CC-function is represented by a semicircle intersecting the x-axis at ϵ_{HF} and ϵ_{LF} , and centered at coordinates $\left[\frac{\epsilon_{HF} + \epsilon_{LF}}{2}, -\frac{\Delta\epsilon}{2} \tan((1-\alpha)\frac{\pi}{2})\right]$. The top of the circle is reached at the characteristic relaxation frequency (i.e. for $\omega\tau = 1$) of the sample and the center of the circle is located below the real-axis.

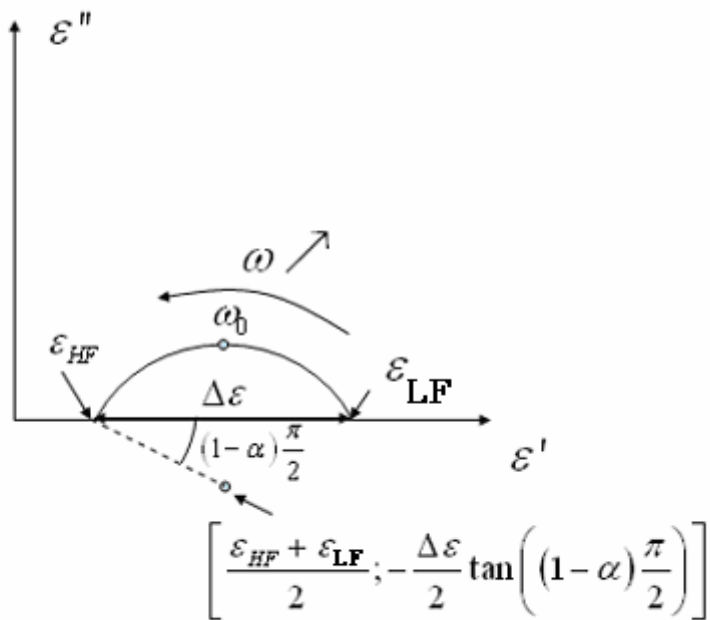


Figure 3. Complex permittivity Nyquist (Cole-Cole) plot for the Cole-Cole function.

It has been previously noted that the different types of polarizations are dependent on the frequency. So, if we sum the different polarizations due to the various phenomena presented and explained above, we obtain:

$$\vec{D} = \epsilon_0 \left(1 + \sum \chi_{elec_j}(\omega) + \sum \chi_{ion_j}(\omega) + \sum \chi_{dip_j}(\omega) + \sum \chi_{int_j}(\omega) \right) \vec{E} \quad (1.12)$$

In the studied frequency range (i.e. $\nu < 10^{11}$ Hz), the contributions of electronic and ionic polarizations are considered as constant, their sum being the high frequency permittivity ϵ_{lat} (i.e. the mean lattice permittivity of the crystal). This assumption is justified because the BDS frequencies are much lower than the optical frequencies. As the result, the equation 1.12 becomes:

$$\vec{D} = \epsilon_0 \left(\epsilon_{lat} + \sum_j \chi_{dip_j}(\omega) + \sum_j \chi_{int_j}(\omega) \right) \vec{E} \quad (1.13)$$

$$\text{with } \epsilon_{lat} = 1 + \sum_j \chi_{elec_j} + \sum_j \chi_{ion_j} \quad (1.14)$$

For a conducting material, the direct-current (long-range) conductivity σ_{dc} is considered as an additional contribution to the imaginary part of its complex permittivity. The dielectric displacement is thus written as:

$$\vec{D} = \epsilon_0 \left(\epsilon_{lat} + \sum_j \chi_{dip_j}(\omega) + \sum_j \chi_{int_j}(\omega) + \frac{\sigma_{dc}}{i\omega\epsilon_0} \right) \vec{E} \quad (1.15)$$

From the expression 1.15, the total complex permittivity is a function of the different contributions previously defined:

$$\epsilon(\omega) = \epsilon_{lat} + \sum_j \chi_{dip_j}(\omega) + \sum_j \chi_{int_j}(\omega) + \frac{\sigma_{dc}}{i\omega\epsilon_0} \quad (1.16)$$

The Nyquist plot (Cole-Cole plot) expected for the complex permittivity corresponds to the sum of different contributions (Eq. 1.16), which can be decorrelated by subtraction of each contribution. As an example in Figure 4, a representative permittivity plot for a conductive material is given.

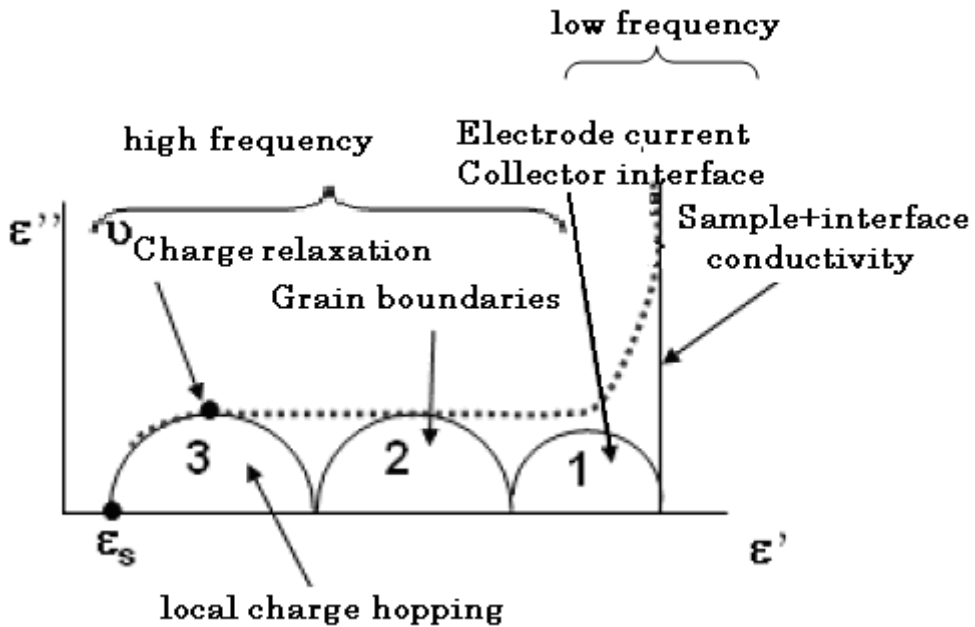


Figure 4. Typical complex permittivity plot of a conducting material.

The easiest way to make the decomposition is usually to start from the low frequencies because the relaxation strengths $\Delta\epsilon$ are larger than those at high frequencies. In conducting materials, the characteristic frequencies of the relaxations are interpretable as the characteristic frequencies of charge carriers' motions (i.e. local and long-range motions). The study of these characteristic frequencies allows us to locate the different scales of analysis (interatomic, grain, agglomerates, etc.).

According to Eq. 1.9, the complex permittivity data $\epsilon(\omega)$ can thus be transformed into complex conductivity $\sigma(\omega)$ and/or complex resistivity data $\rho(\omega) = [\sigma(\omega)]^{-1}$. For example, the complex resistivity plots reveal the different resistances that are encountered along the conduction paths in the sample. These resistances are due to contacts between grains, between clusters of grains and between the sample and the silver paint used for measurements. Each contribution is described by a CC-function:

$$\rho(\omega) = \rho_{HF} + \frac{\rho_{LF} - \rho_{HF}}{1 + (i\omega\tau)^{1-\alpha}} \quad (1.17)$$

where the parameters τ , v_r and α have the same meaning as for the dielectric relaxation (cf. Eq. 1.11). ρ_{LF} and ρ_{HF} are low- and high-frequency limits of the complex resistivity when $\omega\tau \ll 1$ and $\omega\tau \gg 1$, respectively. The CC-function is here represented in the Nyquist plane by a

semicircle intersecting the x-axis in ρ_{LF} and ρ_{HF} , and centered at coordinates $[\frac{\rho_{HF} + \rho_{LF}}{2}, -\frac{\Delta\rho}{2}\tan((1-\alpha)\frac{\pi}{2})]$ as shown in Figure 5 below. The top of the circle is reached at the relaxation frequency characteristic of the sample and the center of the circle is located below the x-axis.

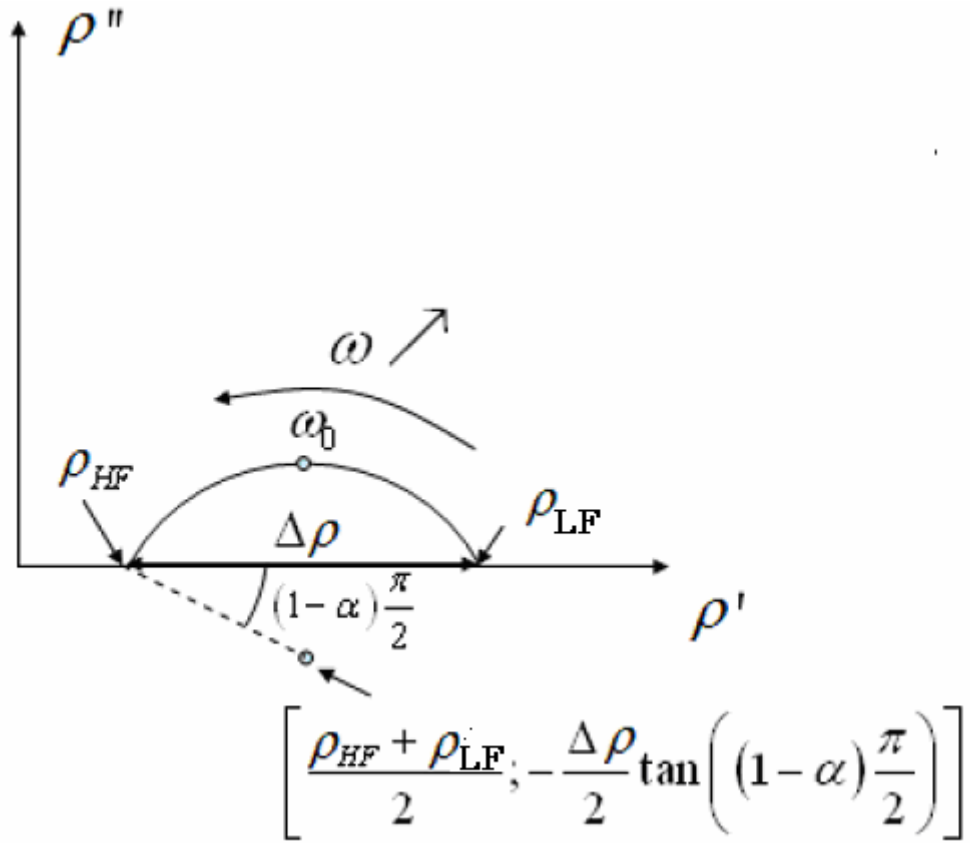


Figure 5. Complex resistivity Nyquist plot for the Cole-Cole function.

Due to the series connection of the different resistances encountered along a conduction path, the expected complex coordinate diagram for the resistivity is the sum of different contributions that can be decorrelated by subtraction. Once again, the easiest way is usually to start with low frequencies because the contributions are far more significant in terms of $\Delta\rho$ than the ones at high frequency. The purpose of using these diagrams in this work is to identify the resistivity of the different scales like the grain (ρ_g), the clusters (ρ_{cl}), the sample (ρ_{sample}) and so on, using the intersection of the different components of resistivity with the x-axis as shown below in Figure 6.

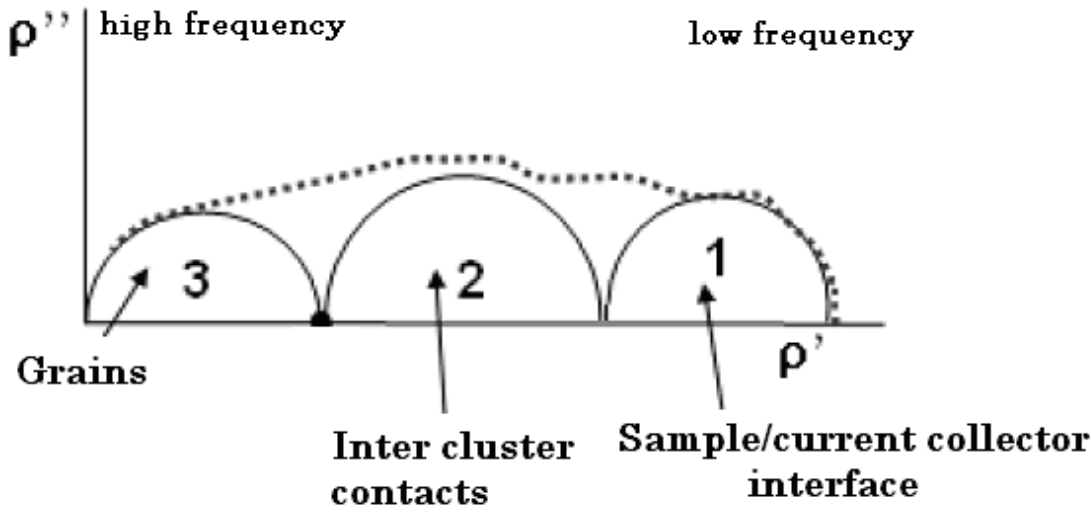


Figure 6. Typical complex resistivity plot of an electronic conductor.

The complex conductivity diagrams can also be used for this same purpose. The procedure, however, is different. In a complex conductivity diagram, the high frequency part is particularly pronounced in comparison to the lower frequencies. The last visible contribution in resistivity is a semi-circle through 0; its equivalent in conductivity is a straight line at right angle. As a result, a right oblique is sought in the diagram of complex conductivity. In conclusion the two representations can be used in complement to each other depending on the application. An easier treatment is obtained in complex conductivity representation when we are looking for information at high frequency and vice versa.

2.3. Experimental aspects

The experiment basically is to study the interaction of an electromagnetic wave and a compacted powder pellet in frequency range between 40 Hz and 10 GHz.

Experimental method: the theory

A Transverse Electromagnetic (TEM) wave is emitted using a network or impedance analyzer through a coaxial output. This TEM wave is propagated in the coaxial waveguide. The interaction is followed by the study of the reflection coefficient of the TEM wave when the sample is placed at the end of a coaxial line terminated by a short circuit. Figure 7 below

shows the measuring cell for determining the electrical parameters of a sample versus frequency.

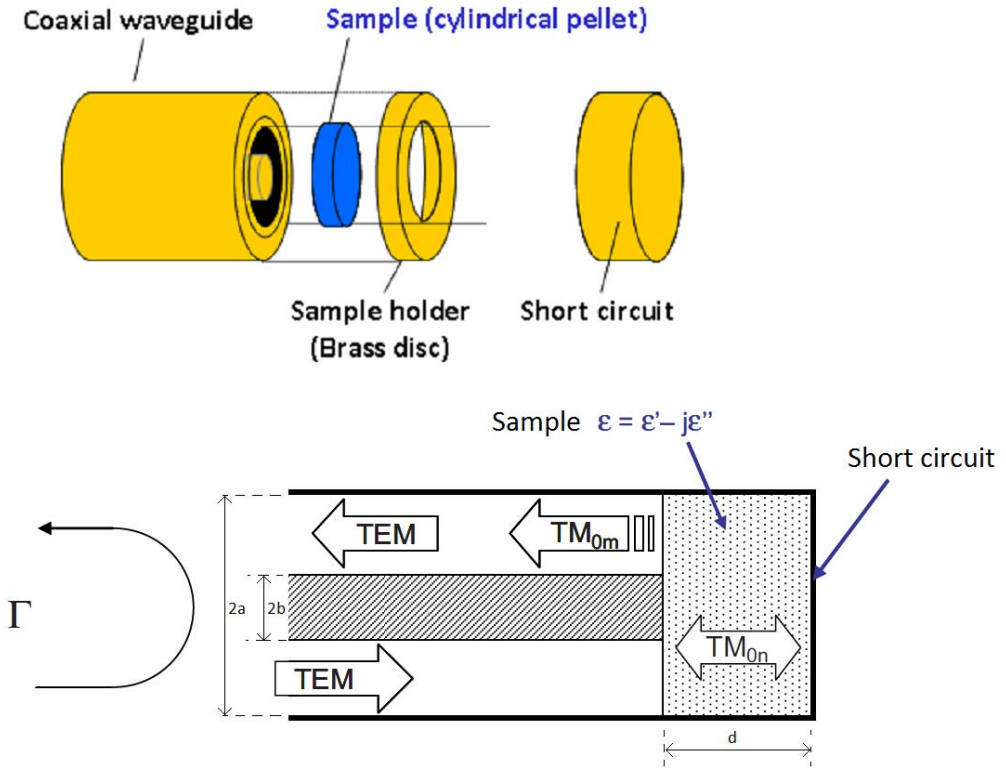


Figure 7. Schemes 3D and 2D of the measuring cell in a reflection mode. TM_{0m} or n are transverse magnetic waves, see text.

The resolution of the electromagnetic problem consists to link the reflection coefficient Γ to the permittivity of the sample. This problem has been solved by N. E. Belhadj-Tahar and al [23]. They have shown that the incident TEM wave generates at the interface coaxial waveguide / sample a reflection TEM wave and infinity of Transverse Magnetic waves (TM_{0n} or m) in the coaxial waveguide and in the sample. The electromagnetic analysis is performed according to the “mode-matching” method: the reflection coefficient of the TEM mode is calculated by matching the fields at the interfaces of the layered material and using the orthogonality properties of modes in cylindrical waveguides. With this method, the admittance Y_s in the interface coaxial waveguide / sample is given by:

23. N.E. Belhadj-Tahar and A. Fourrier-Lamer, IEEE Trans. Microwave Theory Tech., 34 (1986) 346

$$Y_s = Y_0 \frac{jk_0 \epsilon_r}{\ln \frac{b}{a}} \cdot \sum_{n=1}^{\infty} \frac{2J_0^2(k_{Bn}a) \coth \left[\sqrt{k_{Bn}^2 - k_0^2 \epsilon_r} d \right]}{\sqrt{k_{Bn}^2 - k_0^2 \epsilon_r} [k_{Bn} b J_1(k_{Bn} b)]^2} \cdot \left[1 - a \sum_{m=1}^{\infty} \frac{A_m}{A_0(1+\Gamma)} \cdot \frac{Z_1(k_{Am}a)}{\left(\frac{k_{Am}}{k_{Bn}} \right)^2 - 1} \right] \quad (1.19)$$

where a and b are the radius of the outer and inner conductors respectively, d the sample thickness, ϵ_r the relative complex permittivity, k_0 the propagation constant in air, k_{Am} and k_{Bn} the cut-off constants of the TM_{0m} in the coaxial and of the TM_{0n} in the cell respectively, Y_0 the characteristic admittance of the coaxial waveguide (1/50 Siemens), Γ the reflection coefficient of the TEM wave, A_0 the amplitude of the incident TEM, A_m the amplitude of the TM_{0m} , J_0 and J_1 the Bessel functions of the first kind, Z_1 a combination of Bessel functions of the first and second kinds:

$$Z_1(k_{Am}a) = J_1(k_{Am}a) + \left[\frac{-J_0(k_{Am}a)}{N_0(k_{Am}a)} N_1(k_{Am}a) \right] \quad (1.20)$$

The reflection coefficient Γ , the impedance Z_s , and the admittance $Y_s = G + jB$ are linked by the following expression:

$$Z_s(\omega) = Z_0 \frac{1 + \Gamma(\omega)}{1 - \Gamma(\omega)} = \frac{1}{Y_s(\omega)} \quad (1.21)$$

where Z_0 is the characteristic impedance of the coaxial line (50 Ω).

Note that in the coaxial, the TM waves (considered in the theory) and other parasite modes (not considered in the theory), which are due to the imperfections of the geometry (e.g. Transverse Electric modes, TE), must not propagate because the returned wave at the impedance or network analyzers must be only TEM (the reflection coefficient is determined by the measurement of the TEM emitted and received). We have used the coaxial APC7-mm standard ($2a = 7$ mm, Figure 7): the first TM or TE mode (in fact the TE_{11}) begins to propagate in the coaxial at 19.6 GHz, which determines the maximum frequency of our measurement set-up (in fact 18 GHz to have a safety margin).

Experimental set up

The process to obtain the reflection coefficient is described here.

Measurement apparatus

The measurements of the reflection coefficient versus frequency are made with impedance or network analyzers. In order to achieve dielectric spectra over a wide frequency band, it is necessary to use several measuring devices (Figure 8). Each one is independent. An alternator enables to use successively these analyzers without dismantling the cell, which is very important during measurements versus temperature. In our case, we used three devices: a HP 8510 (and then an Agilent PNA network analyser E8364B used between 10 MHz – 10 GHz), an Agilent 4291 impedance analyzer (1 MHz - 1.8 GHz) and an Agilent 4294 impedance analyzer (40 Hz - 110 MHz).

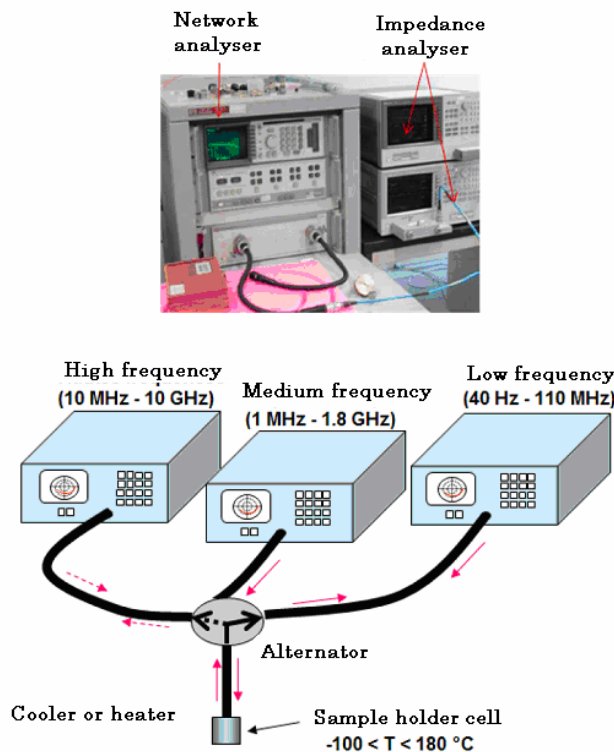


Figure 8. Experimental setup with 3 machines in case of a cell in reflection setup.

Coaxial waveguide

The standard APC-7mm is used for the coaxial waveguide: the diameter of the outer conductor (2a) and of the inner conductor (2b) is 7 mm and 3.04 mm respectively. The maximum frequency of this standard is 18 GHz. We have made measurements up to 10 GHz.

Calibration

Before the measurement of the sample, a calibration process is applied to remove the systematic errors of the analyzers and coaxial guide: three well-known charges placed in the calibration plane (interface coaxial waveguide / sample, cf. figure 7) are measured.

- An “open circuit”, actually a capacitor $C = 89 \text{ fF}$ (impedance $Z = 1/jC\omega$);
- A short circuit: the reflection coefficient $\Gamma(\omega) = -1$ (and the impedance $Z = 0$);
- A load of 50Ω or "adapted charge": the reflection coefficient $\Gamma(\omega) = 0$ (and of course the impedance $Z = 50 \Omega$).

Once the network or impedance analyzers are calibrated, the impedance (or the reflection coefficient) of the cell containing the sample under test can be measured in the plane of calibration.

Sample preparation

In general, the samples are compacted powders in pellets with diameters of 7 mm or 3 mm and thickness between 0.3 and 1.1 mm. We have used 7 mm diameter pellets. Hereafter only this configuration is discussed. The contact quality between the sample and the metallic parts are very important: a poor contact adds air gap, i.e. an unwanted capacity. For this purpose, all these areas, i.e. the inner conductor / sample, the sample holder / sample and the short-circuit / sample, are usually metallised with silver paint. Carbon or gold contacts can also be made following evaporation or painting methods.

The sample holder must be for the same raison carefully chosen: indeed, an air gap can exist between the outer conductor of the waveguide and the holder if the holder is too thin or between the inner conductor of the waveguide and the sample if it is too thick. These problems have been studied in [24].

24. H. de Chanterac, « Contribution à l'étude de la modulation de la transmission et de l'absorption d'ondes électromagnétiques aux fréquences microondes. Faisabilité d'un dispositif contrôlé électriquement », UPMC PhD thesis, 1992

Permittivity calculation and accuracy

Software allows us the acquisition (Labview) and calculation (C language) of this data, i.e. to compute the complex permittivity versus frequency from the admittance according to [23]. As we have seen, an infinite number of TM modes are generated at the interface coaxial / sample: we must then perform a truncation. It has been shown that the first three TM_{0i} in the coaxial waveguide and the first six TM_{0i} in the sample are enough, the higher modes being negligible [25]. Note that the number of TM modes considered in the coaxial waveguide and in the sample is different to fulfill the energy balance.

The accuracy depends on the analyzers used and on the admittance of the cell measured. A way to study the accuracy is to simplify the rigorous electromagnetic resolution of [23] by using a simple capacitance model if the fringing capacitance is neglected (which is realistic when the sample is not a film): indeed, the sample can be seen as a parallel plate capacitance with two circular plates (diameter $2a$ and $2b$, cf. Figure 7), the sample being of course the dielectric. Then, the relation between the admittance and the permittivity is [26]:

$$C = \epsilon_0 \epsilon \pi b^2 / d \quad (1.22)$$

where b is the radius of the inner conductor of the coaxial guide and d the thickness of the sample. Note that this formula is valid at low frequency (depending on the permittivity, this is discussed in [**Erreur ! Signet non défini.**]). Then, the complex permittivity can be computed from the measured complex admittance:

$$\epsilon = d Y_s / (j \omega \epsilon_0 \pi b^2) \quad (1.23)$$

For the low-frequency device, an error of less than 10% is obtained on the modulus of the admittance when the modulus measured is between the following limits (in Siemens, S):

$$10^{-9} \langle |Y_s| \rangle 10 \quad [S] \quad (1.24)$$

The sensitivity of the apparatus been known, we can deduce easily from equations 1.23 and 1.24 a condition on the permittivity and the frequency. For a sample thickness of 1 mm, we obtain a product management module of the complex permittivity with the frequency expressed in Hz:

25. O. Dubrunfaut, « Instrumentation pour la caractérisation aux fréquences micro-ondes de matériaux magnétiques solides ou liquides », UPMC PhD thesis, 1997.

26. N. Marcuvitz, « Wave guide Handbook », 1st edition, Mc Graw-Hill, New York, 1951.

5. N.-E. Belhadj-Tahar, O. Dubrunfaut, A. Fourrier-Lamer, J. of Electromagnetic Waves and App., 15 (2001) 727.

$$4.10^3 \langle |\epsilon| f_{Hz} \rangle 4.10^{12} \quad [\text{Hz}] \quad (1.25)$$

In the case of the high frequency device, the product of the modulus of the complex permittivity and the measured frequency (expressed in GHz) must be above a certain value from the geometry of the coaxial line to ensure the accuracy of the measurement. For a sample thickness of 1 mm, we have:

$$1 \langle |\epsilon| f_{GHz} \rangle \quad [\text{GHz}] \quad (1.26)$$

For a sample thickness of 0.5 mm the factor 4 in equation 1.25 would become 2 and the factor 1 in equation 1.26 would become 0.5. If the conditions above are fulfilled, instrumental uncertainties are limited in comparison to uncertainties related to decomposition of data. Using equation 1.25 and 1.26 instrumental uncertainties have been verified and are found to be well within the valid limits for all the samples. The table below (to be numbered) shows the results for one sample (CLFP3). As the results, instrumental uncertainties are limited in comparison to uncertainties related to decomposition of data. Overall uncertainties are reasonably estimated to be around 10%.

Sample (0.5-1mm)	At Low frequency $ \epsilon f$	At high frequency $1\langle \epsilon f\rangle$
CLFP3	$6.6 \times 10^6 - 5.4 \times 10^8 \text{ Hz}$ (between 40Hz and 110MHz)	38 GHz (at 10Ghz)

2.4. Previous works performed using the BDS

In this section we will summarize some previous works which made use of the already discussed broadband dielectric spectroscopy (BDS) technique. Mainly the case of oxides and granular/ hierarchical materials will be discussed. In each case, even though the objective is different, the principle utilized for the experiments was similar. This part is supposed, first of all, to provide information on the versatility of the technique and secondly, it will enable us to have an insight in the type of information that we can get from the technique.

The technique was implemented to determine the conductivity of possible active materials for lithium batteries: $\text{Li}_x\text{V}_2\text{O}_5$, $\text{Ni}_{1+x}\text{O}_2$, $\text{Li}_x\text{WO}_3\text{H}_2\text{O}$, $\text{Li}_{1+x}\text{V}_3\text{O}_8$

[27,28,29,30,31,32,33]. In all cases, the analysis of the high-frequency part of the electrical spectra and its variations with the temperature allowed the determination of the bulk conductivity of the crystallites or grains, as well as the conduction behaviour (typically small polarons hopping). Dielectric and resistivity relaxations were also identified and could be attributed to the existence of interfaces at different scales within the samples (crystallites or grains boundaries, inter clusters junctions and sample/collector contact). The role of the texture of the samples (sample porosity, particle size) on the dc-conductivity and the conduction behaviour (surface vs. bulk diffusion of small-polarons on (in) particles or grains) was also highlighted. An influence of adsorbed polar molecules (water, ethylene and propylene carbonate) at the surface of the grains could be identified and quantified. A real composite electrode with a binder and a conductive additive (carbon black) added to the active material ($\text{Li}_{1.1}\text{V}_3\text{O}_8$) was also studied [21]. Different electrical relaxations were evidenced on the composite electrodes, resulting from the polarizations at the different scales of the carbon black network which short-circuited the $\text{Li}_{1.1}\text{V}_3\text{O}_8$ clusters (or particles): the carbon black (i) graphite crystallites, (ii) particles, (iii) and clusters. Higher effective conductivities, as well as thinner distribution of relaxation times of the clusters, were measured for the electrode with the better developed percolating network of smaller carbon black clusters.

The technique was also used to study ionic conductors. In the fast Li^+ conductor perovskite [LLTO] $\text{Li}_{3x}\text{La}_{2/3-x}\text{TiO}_3$ ($x = 0.09$) [34,35], it was possible to distinguish between the long range and localized motions of the Li^+ ions as well as the dimensionality (2D in the grain boundaries or 3D in the bulk) of these ones depending on the temperature. Similarly, the ionic transport properties of $\text{Ba}_{1.16}\text{Al}_{2.32}\text{Ti}_{5.68}\text{O}_{16}$ and $\text{Ba}_{1.16}\text{Ga}_{2.32}\text{Ti}_{5.68}\text{O}_{16}$ hollandites in the temperature range 320–440 K have been measured [36].

Finally, the electrical properties and phase transitions of CsHSO_4 , CsHSeO_4 , CsDSeO_4 and NH_4HSeO_4 have been studied [37]. Several dipolar relaxations were observed and

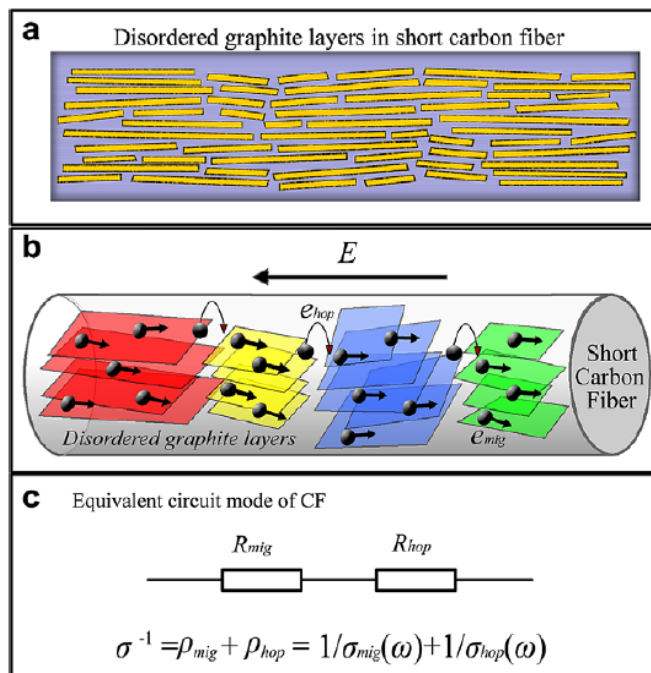
- [27]. J.C. Badot, A. Mantoux, N. Baffier, O. Dubrunfaut and D. Lincot, *J. Mater. Chem.* ... (2004) ...
- [28]. J.C. Badot, V. Bianchi, N. Baffier and N. Belhadj-Tahar, *J. Phys.: Condens. Matter*, 14 (2002) 6917
- [29]. J.C. Badot, A. Mantoux, N. Baffier, O. Dubrunfaut, D. Lincot, *J. Phys. Chem. Sol.*, 67 (2006) 1270
- [30]. L. Beluze, J.C. Badot, R. Weil, and V. Lucas, *J. Phys. Chem. B*, 110 (2006) 7304
- [31]. B. Pecquenard, J.C. Badot, N. Baffier, and N. Belhadj-Tahar, *Phys. Stat. Sol. (a)* 159 (1997) 469
- [32]. J.C. Badot, L. Beluze, and O. Dubrunfaut, *J. Phys. Chem. C*, 112 (2008) 14549
- [33]. J.C. Badot, E. Ligneel, O. Dubrunfaut, J. Gaubicher, D. Guyomard, B. Lestriez, submitted *J. Phys. Chem. C*
- [34]. O. Bohnke, J.C. Badot and J. Emery, *J. Phys.: Condens. Matter* 15 (2003) 7571
- [35]. T. Šalkus, E. Kazakevičius, A. Kežionis, A.F. Orliukas, J.C. Badot, O. Bohnke, *Solid State Ionics* 188 (2011) 69
- [36]. V. Aubin-Chevaldonnet, J.C. Badot, D. Caurant, *Solid State Ionics* 178 (2007) 1274
- [37]. J.C. Badot, *Solid State Ionics* 35 (1989) 143

assigned to protonic species re-orientations (HSO_4^- , HSeO_4^- , NH_4^+), to proton jump relaxations, and HSO_4^- (DSeO_4^- , HSeO_4^-) reorientations.

In conclusion, this section showed how versatile the technique is. It is also clear that the knowledge of the micro- and macro-structure is very important for the reliable interpretation of the dielectric data. The technique will enable to study grain boundary and hopping mechanisms in granular materials. It is also possible to discriminate between surface and volume conductivity mechanism in samples with different particle sizes. The temperature dependence of the dielectric properties and the extracted parameters such as the frequency and conductivity pre exponential factors provide valuable information on the nature and type of charge carriers. It also plays a decisive role in determining the mechanism of charge transport.

3. Conduction mechanisms in carbon (hopping)

In this part some of the established mechanisms of conductivity in carbons will be briefly presented. Here the objective is to offer a perspective on the possible ways of conductivities in such systems. The study of carbon fibers (CFs)/Silica composites [38] provided a simplified view of the existing conduction mechanism in the CFs; it was suggested that in carbon fibers there exist both the migrating conductance in the graphite plane direction and the hopping conductance among disordered graphite layers.



[38]. M-S. Cao, W-L. Song, Z-L. Hou, B. Wen, J. Yuan, Carbon 48 (2010) 788

Figure 9. (a) Schematic illustration showing the microstructure of a CFs according to the HRTEM from Refs. [39,40]. (b) Schematic illustration exhibiting the two types of conductance occurring on the graphite layers in a carbon fibers(CFs). (c) Equivalent circuit model of a carbon fiber(CF).

Figure 9a shows the disordered graphite layers in short CFs. Figure 9b specifically illustrates the migrating electrons on the graphite plane and the hopping electrons among the disordered layers in CFs. Meanwhile, Figure 9c exhibits an equivalent series circuit of the two resistances to demonstrate these behaviours. In Figure 9c, σ_{mig} and σ_{hop} are the electrical conductivities of electron migration and of electron hopping, respectively. In accordance with the electrical property of graphite, both the migrating conductance of graphite layers in CFs and the hopping conduction among graphitic layers are observed to be thermally activated.

On the other hand J.P. Sullivan, T.A. Friedman presented their findings on electronic transport in amorphous carbon (a-C) [41]. In their work, combined stress relaxation and electrical transport studies were used to identify the transport mechanism in a-C films prepared by pulsed-laser deposition. It was found that the conductivity of a-C films is exponentially proportional to increases in 3-fold carbon concentration. This result is explained by thermally activated hopping along carbon 3-fold chains (sp^2) combined with chain-to-chain tunnelling. They also stressed that the heterogeneous nature of the conductivity may explain the spatially localized electron emission which is observed in a-C assuming a tunnel barrier emission model. According to the authors, most experimental evidence indicates that electronic transport, particularly near room temperature and at low applied electric fields, behaves according to *hopping conduction*. Several evidences are provided for such an assertion by the authors. In general, there exists enough evidence to indicate that, the mainstream consensus on the type of conduction mechanisms in the carbon is hopping between graphitic layers. However, there exists some debate on the specific nature of the conduction mechanisms.

5. State of the art about the understanding of the electronic properties of composite electrodes for lithium batteries.

As the composite electrode is a bi-percolating medium involving ionic and electronic parts, its architecture (dispersion of the active material(AM), the carbon additives (C) , binder

[39]. B. Reznik, D. Gerthsen, K.J. Hüttinger, Carbon 39 (2001) 215

[40]. G.B. Zheng, H. Sano, K. Suzuki, K. Kobayashi, Y. Uchiyama, H.M. Cheng, Carbon 37 (1999) 2057

[41]. J.P. Sullivan, T.A. Friedman, Master thesis ,Sandia National Laboratories, MS 1421, Albuquerque, NM 87185-1421, USA (1997)

ingredients (B), porosity...) does influence the electrode performance (energy, power, cycle life).

The critical importance of the electronic conductivity with respect to battery performance (energy, power [42,43,44,45,46,47] and cyclability [48,49,50]) has been repeatedly shown. In particular for silicon negative electrodes, the loss of interparticle contacts (C / C or C / AM) and the resulting degradation of the electronic conductivity are often invoked as probable causes for loss of capacity on cycling [51]. Recent modelling [52] suggests the contributions of the non-electroactive components to the electrode resistance (see Figure 2b in the general introduction), is very significant in particular for thick films. However, scientific literature is scarce in this research area.

All parameters that influence the electrical conductivity of a composite electrode, i.e. the content and nature of C, the content and nature of B, and the compression and so on, must be chosen by “try and see experiments or on a case-by-case basis”. Many studies have been done in the industry in this field, but such knowledge is proprietary information on one hand, and, it remains qualitative (empirical) on the other hand.

In short, there is clearly a lack of fundamental understanding of the relationships between the “formulation” (composition, processing), the morphology, the electrical properties and the electrochemical performance of the composite electrode [36,53,54,55,56,57,58,59].

-
- [42]. G. B. Appetecchi, M. Carewska, F. Alessandrini, P. P. Prosini, S. Passerini, *J. Electrochem. Soc.*, **147**, 451 (2000).
 - [43]. S. Mandal, J. M. Amarilla, J. Ibáñez, J. M. Rojo, *J. Electrochem. Soc.*, **148**, A24 (2001).
 - [44]. K. Sheem, Y. H. Lee, H. S. Lim, *J. Power Sources*, **158**, 1425 (2006).
 - [45]. M.S. Wu, J.T. Lee, P.C. J. Chiang, J.C. Lin, *J. Mater. Sci.*, **42**, 259 (2007).
 - [46]. K.A. Striebel, A. Sierra, J. Shim, C.W. Wang, A.M. Sastry, *J. Power Sources*, **134**, 241 (2004).
 - [47]. J.S. Gnanaraj, Y.S. Cohen, M.D. Levi, D. Aurbach, *J. Electroanal. Chem.*, **516**, 89 (2001).
 - [48]. J. Shim, K.A. Striebel, *J. Power Sources*, **122**, 188 (2003).
 - [49]. J. Lei, F. McLarnon, R. Kostecki, *J. Phys. Chem. B*, **109**, 952 (2005).
 - [50]. R. Kostecki, J. Lei, F. McLarnon, J. Shim, K. Striebel, *J. Electrochem. Soc.*, **153**, A669 (2006).
 - [51]. (a) N. Dimov, S. Kugino, M. Yoshio, *Electrochim. Acta* **48**, 1579 (2003). (b) J. H. Ryu, J. W. Kim, Y.-E. Sung, S. M. Oh, *Electrochim. Solid-State Lett.* **7**, A306 (2004).
 - [52]. V. Srinivasan, J. Newman, *J. Electrochem. Soc.*, **151**, A1517 (2004).
 - [53]. D. Guy, B. Lestriez, D. Guyomard, *Adv. Mater.*, **16**, 553 (2004).
 - [54]. (a) N. Dimov, S. Kugino, M. Yoshio, *Electrochim. Acta* **48**, 1579 (2003). (b) J. H. Ryu, J. W. Kim, Y.-E. Sung, S. M. Oh, *Electrochim. Solid-State Lett.* **7**, A306 (2004).
 - [55]. S.D. Beattie, D. Larcher, M. Morcrette, B. Simon, J.-M. Tarascon, *J. Electrochem. Soc.* **155**, A158 (2008).
 - [56]. B. Lestriez, S. Bahri, I. Sandu, L. Roue, D. Guyomard, *Electrochim. Commun.*, **9**, 2801 (2007).
 - [57]. J.H. Lee, U. Paik, V.A. Hackley, Y.M. Choi, *J. Electrochem. Soc.*, **152**, A1763 (2005).
 - [58]. C.C. Li, J.T. Lee, X.W. Peng, *J. Electrochem. Soc.*, **153**, A809 (2006).
 - [59]. W. Porcher, B. Lestriez, S. Jouanneau, D. Guyomard, *J. Electrochem. Soc.*, **156**, A133 (2009).

In the prospect of a more fundamental understanding of the electronic conductivity, on one side, Sastry's group [60] provided exhaustive modelling study on the percolation threshold concentration dependence on shape, orientation of C and electrode thickness [61,62]. On the other side, the group at IMN [63,64,65,66] provided exhaustive experimental studies regarding the dependence on the nature of B, C and on the processing conditions of the composite electrode and highlighted the importance of electron tunnelling at the interparticle contacts.

The major difficulty in relating the electrochemical performance to the electronic conductivity within the composite electrode is that the direct current (dc) transverse electronic conductivity (surface-to-surface average conductivity), that is the usually measured quantity, is a macroscopic averaged quantity that does not relate directly to the real electronic wiring of the AM grains [47,67,68]. At low rate, where the ionic conductivity is not a limitation, discrepancies are often observed between σ_{dc} and the discharge capacity of the composite electrode when several formulations are compared [47]. Interpretations naturally postulate a critical importance of the composite electrode architecture at the micro and nano scales on the electronic conductivity. The nano and microscopic aspects / entities involved in the electronic wiring of AM grains are:

- At the nanoscale, most of the electronic contacts within the composite electrode, i.e. C / C and C / AM and C or AM / CC, could be described by tunnel junctions, whose resistivity ρ increases exponentially with w the gap thickness [47,69]. This parameter w is dependent on the amount of binder Γ that adsorbs at the surface of the solid (particles and current collector) surfaces during the elaboration of the electrode [63] (Figure 2a). The surface contact area A through which most of the tunnelling occurs, the height of the potential barrier V_0 , the dielectric constant ϵ of the binder which fills the gap and w are all important factors with respect to the resistivity of the contact

-
- [60]. Collaboration between the Michigan University, the Lawrence Berkeley National Laboratory and Institut de Recherche d'Hydro Québec
- [61]. C. W. Wang, A. M. Sastry, K. A. Striebel, K. Zaghib, *J. Electrochem. Soc.*, **152**, A1001 (2005).
- [62]. Y.B. Yi, C.W. Wang, A.M. Sastry, *J. Electrochem. Soc.*, **151**, A1292 (2004).
- [63]. D. Guy, B. Lestriez, R. Bouchet, D. Guyomard, *J. Electrochem. Soc.*, **153**, A679 (2006).
- [64]. E. Ligneel, B. Lestriez, A. Hudhomme, D. Guyomard, *Electrochim. Solid-State Lett.*, **10**, A122 (2007).
- [65]. E. Ligneel, B. Lestriez, A. Hudhomme, D. Guyomard, *J. Electrochem. Soc.*, **154**, A235 (2007).
- [66]. B. Lestriez, S. Desaever, J. Danet, P. Moreau, D. Plée, D. Guyomard, *Electrochim. Solid-State Lett.*, **12**, A76 (2009).
- [67]. R. Dominko, M. Gaberscek, J. Drofenik, M. Bele, S. Pejovnik, *Electrochim. Solid-State lett.*, **4**, A187 (2001).
- [68]. M. Gaberscek, J. Jamnik, *Solid State Ionics*, **177**, 2647 (2006).
- [69]. G.R. Ruschau, S. Yoshikawa, R.E. Newnham, *J. Appl. Phys.*, **72**, 953 (1992).

point [70,71,72]. All parameters (w , Γ , A , V_0 , and ε) rely upon material (AM, C and B) properties and processing conditions of the composite electrodes. For example A would depend on the shape of the C particles, ε would depend on the molecular structure of B, Γ would depend on the affinity of B for C and/or AM, etc [48].

- At the micro scale, the C network can be characterized in terms of primary particles and clusters of primary particles. The C / AM interface can be characterized in term of number of contact points. The type of C network can be defined according to the density of the secondary clusters, airy ones being referred to as highly structured network [73]. On the whole, a *highly structured* network increases the number of contact points at the C / AM interface. The same kind of hierarchical description can be proposed for AM grains made up of aggregated particles (micro scale) with grain boundaries (nanoscale) in between.

6. Conclusion

We believe that the electrical properties of composite electrodes are poorly understood, mostly due to the lack of pertinent technique and also due to the complexity of their hierarchical architecture. BDS appears a technique of choice, which will be applied in the following two chapters to C-LiFePO₄, one of the most important active material for lithium batteries with a complex architecture as it is a (nano)composite by itself.

-
- [70]. P. Sheng, *Phys. Rev. B*, **21**, 2180 (1980).
 - [71]. P. Sheng, E.K. Sichel, J.I. Gittleman, *Phys. Rev. Lett.*, **40**, 1197 (1978).
 - [72]. E.K. Sichel, J.I. Gittleman, P. Sheng, *Phys. Rev. B*, **18**, 5712 (1978).
 - [73]. I. Balberg, *Phys. Rev. Lett.*, **59**, 1305 (1987).

Chapter 2: Binary Systems

1. Introduction

LiFePO_4 is a mixed conductor which can have a cooperative motion of lithium ions and polarons. [74] The electronic conductivity is known to be due to (hole) small polaron transfer [75], these charge carriers being trapped by lithium vacancies. Previously published values for the electronic conductivity of LiFePO_4 range between 10^{-7} to 10^{-8}S/m [76] and the ionic conductivity is measured to be in the same range. [77] LiFePO_4 grains are usually wrapped by a carbon coating. The coating is an amorphous carbon which contains short-order sp^2 -coordinated carbon domains (in-plane correlation length of 1–4 nm) bonded by sp^3 -coordinated carbon atoms, and has some functional groups adsorbed on the sample surface. [78,79] The carbon coating increases the conductivity of the material, likely provides better electronic contacts between submicronic particles within large clusters, and thus improves the electrochemical performance. [80,81] The carbon content must be high enough for full and homogeneous coating of the particles; however, too thick coatings (with average thickness of 5–10 nm) show a deterioration effect of the electrochemical performance, probably reflecting a kinetic hindrance to lithium ions penetration. [82,83] In previous works, the electrochemical performance of LiFePO_4 composite electrodes was closely correlated to macroscopic (sample) conductivities of the active material. [84,85] Higher discharge capacities and better rate capability of LiFePO_4 composite electrodes were directly correlated with increased content of sp^2 (vs. sp^3 -) carbon domains as determined by Raman spectroscopy, a trend which can be interpreted in terms of the increasing amount of larger graphene clusters in the disordered carbon structure. The sample conductivity data are however fairly limited because the direct-current techniques do not give information on conduction mechanisms. Dc measurements

-
- [74]. T. Maxish, F. Zhou, and G. Ceder, Phys. Rev. B, 73 (2006) 104301.
 - [75]. K. Zaghib, A. Mauger, J.B. Goodenough, F. Gendron, and C.M. Julien, Chem. Mater., 19 (2007) 3740.
 - [76]. C. Delacourt, L. Laffont, R. Bouchet, C. Wurm, J.-B. Leriche, M. Morcrette, J.-M. Tarascon, and C. Masquelier, J. Electrochem. Soc. 152 (2005) A913.
 - [77]. R. Amin, P. Balaya, J. Maier, Electrochem. Solid-State Lett. 9 (2007) A13
 - [78]. M.M. Doeff, Y. Hu, F. McLarnon, R. Kostecki, Electrochem. Solid State Lett., 6 (2003) A207
 - [79]. A. Salah, A. Mauger, K. Zaghib, J. B. Goodenough, N. Ravet, M. Gauthier, F. Gendron, and C. M. Julien, J. Electrochem. Soc., 153, A1692 (2006).
 - [80]. N. Ravet, A. Abouimrane, M. Armand, Nature Mater., 2 (2003) 702.
 - [81]. Y. Hu Y, M.M. Doeff, R. Kostecki, R. Finones, J. Electrochem. Soc. 151 (2004) A1279
 - [82]. R. Dominko, M. Bele, M. Gabersek, M. Remskar, D. Hanzel, S. Pejovnik, J. Jamnik, J. Electrochem. Soc., 152 (2005) A607
 - [83]. J. Mozkon, R. Dominko, M. Gabersek, R. Cerc-Korošec, J. Jamnik, J. Electrochem. Soc., 153 (2006) A1805
 - [84]. M.M. Doeff, J.D. Wilcox, R. Yu, A. Aumentado, M. Marcinek, R. Kostecki, J Solid State Electrochem., 12 (2008) 995
 - [85]. J.D. Wilcox, M.M. Doeff, M. Marcinek, R. Kostecki, J. Electrochem. Soc. 154 (2007) A389

were also carried out on sintered samples, thus not reflecting the material as is used in the battery. [86].

An approach toward a more fundamental understanding of the electronic transport in these amorphous carbon coatings can be found in the literature. The most likely structure is where sp^2 sites arrange in compact clusters of fused six fold ring, i.e., graphitic layers of about 1.5nm in diameter, bounded by sp^3 sites. [87] Other theoretical works suggest that the sp^2 -coordinated carbon rather tend to form extended chain-like structures with fractal dimension between 1 and 2, but for films of carbon containing a majority of sp^3 -coordinated carbon. [88] Published values for the activation energy of the low frequency (dc-conductivity) range between 0.04-0.13eV. [76,86] A larger degree of graphitization results in smaller activation energy [89]. It is typically observed that the electrical conductivity increases and activation energy decreases when the sp^2 -coordinated content increases. [90,91] Most experimental evidence indicates that electronic transport, particularly near room temperature and at low applied electric fields ($< 10^4$ V.cm $^{-1}$), behaves according to hopping or tunneling conduction between clusters of sp^2 -coordinated carbon. [92] To date no direct measurement of the coating conductivity has been achieved owing to the lack of suitable technique. Only indirect relationships between the conductivity of pressed or sintered macroscopic pellets of C-LiFePO₄ and the sp^2 content have been achieved. [84,85] Here, we use the broadband dielectric spectroscopy from low frequencies (few Hz) to microwaves (few GHz), which allows to measure the electrical parameters (permittivity, resistivity, and conductivity) with respect to the frequency. The understanding of the transport mechanism, from the sp^2 -coordinated carbon domains up to the sample scale will be interpreted.

As previously pointed out in chapter one the electrical response of a material is due to charge density fluctuations, when it is submitted to a time-dependent electric field. This response can be described either by the time dependent current density $j(t)$ or by the time dependent dipole moment $\mu(t)$. We have already shown in chapter one that in the frequency

-
- [86]. M. Maccario, L. Croguennec, B. Desbat, M. Couzi, F. Le Cras, L. Servant, J. Electrochem. Soc. 155 (2008) A879
 - [87]. J. Roberston, E.P. O'Reilly, Phys. Rev. B, 35 (1987) 2946.
 - [88]. N.A. Marks, D.R. McKenzie, B.A. Pailthorpe, M. Bernasconi, M. Parrinello, Phys. Rev. Lett., 76 (1996) 768.
 - [89]. M. Koos, S.H.S. Moustafa, E. Szilagyi, I. Pocsik, Diamond. Relat. Mater., 8 (1999) 1919.
 - [90]. D.I. Jones and A.D. Stewart, Phil. Mag. B, 46 (1982) 423.
 - [91]. J.P. Sullivan, T.A. Friedman, *Electronic transport in amorphous carbon*, 1997 Dec 01, Report Number(s) SAND-97-1903C; CONF-9707129-, available at [ww.osti.gov/bridge/product.biblio.jsp?osti_id=555540](http://www.osti.gov/bridge/product.biblio.jsp?osti_id=555540)
 - [92]. D. Dasgupta, F. Demichelis, A. Tagliaferro, Phil. Mag. B, 63 (1991) 1255.

domain, these fluctuations are either expressed by the frequency-dependent complex permittivity $\epsilon(\omega)$, conductivity $\sigma(\omega)$ or resistivity $\rho(\omega)$ which are related by,

$$\sigma(\omega) = [\rho(\omega)]^{-1} = i \omega \epsilon_0 \epsilon(\omega) \quad (2.1)$$

where ϵ_0 is the vacuum permittivity, and $\omega = v \cdot 2\pi$ the frequency expressed in s^{-1} (v being the frequency expressed in rad.s^{-1}). The time scale (or relaxation time) of the fluctuations depends generally on the geometric scale at which they occur. In electronic conductors, different electrical relaxations result from their hierarchical structure (microstructure, nanostructure and crystal structure). Several polarization mechanisms occurring at different scales with distinct characteristic frequencies can be separated and treated individually. When the frequency increases, different kinds of polarization appear in the following order: a) interfacial polarization due to the existence of cluster and particle boundaries giving rise to relaxations in the low-frequency domain; b) orientation polarization due to local charge motions (e.g. electrons) giving rise to relaxations in radio- and microwave frequency domains.

In this chapter, results of the dielectric measurements performed on one non carbon coated and three carbon coated LiFePO₄ samples with two different particle sizes and three carbon contents, will be discussed. In the first part of this chapter, the morphologies of the different samples are carefully detailed. Then, their permittivities and conductivities vs. temperature and frequency are described between 40 and 10¹⁰ Hz.

2. Results and discussion

2.1. Morphology and analysis of the LiFePO₄ materials

Materials: Carbon and non-carbon coated (0-4 wt %) LiFePO₄ pristine materials ranging in particle size between 50-150nm were supplied by our industrial partner UMICORE Cobalt & Specialty Materials, Belgium. In short, their synthesis follows a two step process. First the LiFePO₄ primary particles are synthesized. Second, they are carbon coated using an organic compound as a precursor.

Table 1. The samples studies with their notifications.

Sample	Particle size d (nm)	Carbon coating (wt%)	Measured at IMN	Data from Umicore	B.E.T. (m^2/g) $S_{theo} = 6/(d \times \rho)$
LFP	150	0	23	8	11
CLFP1	50	4.0	55	44	33
CLFP2	150	2.8	30	24	11
CLFP3	150	4.0	36	55	11

Material characterization: Scanning electron microscopy (SEM) imaging on gold-palladium sputtered samples using a JEOL JSM 7600F apparatus was used to study the morphology of the materials. Representative SEM images of the samples are shown in Figure 3. The pristine materials are in the form of spherical balls of few μm composed of agglomerated primary particles. Moreover, the SEM pictures suggest the probable existence of clusters of few particles, which are tightly bound by the carbon coating. Note that the particle sizes have not been measured. The values given Table 1 come from UMICORE. The B.E.T. values are not used later in the interpretation of the results and are thus not discussed.

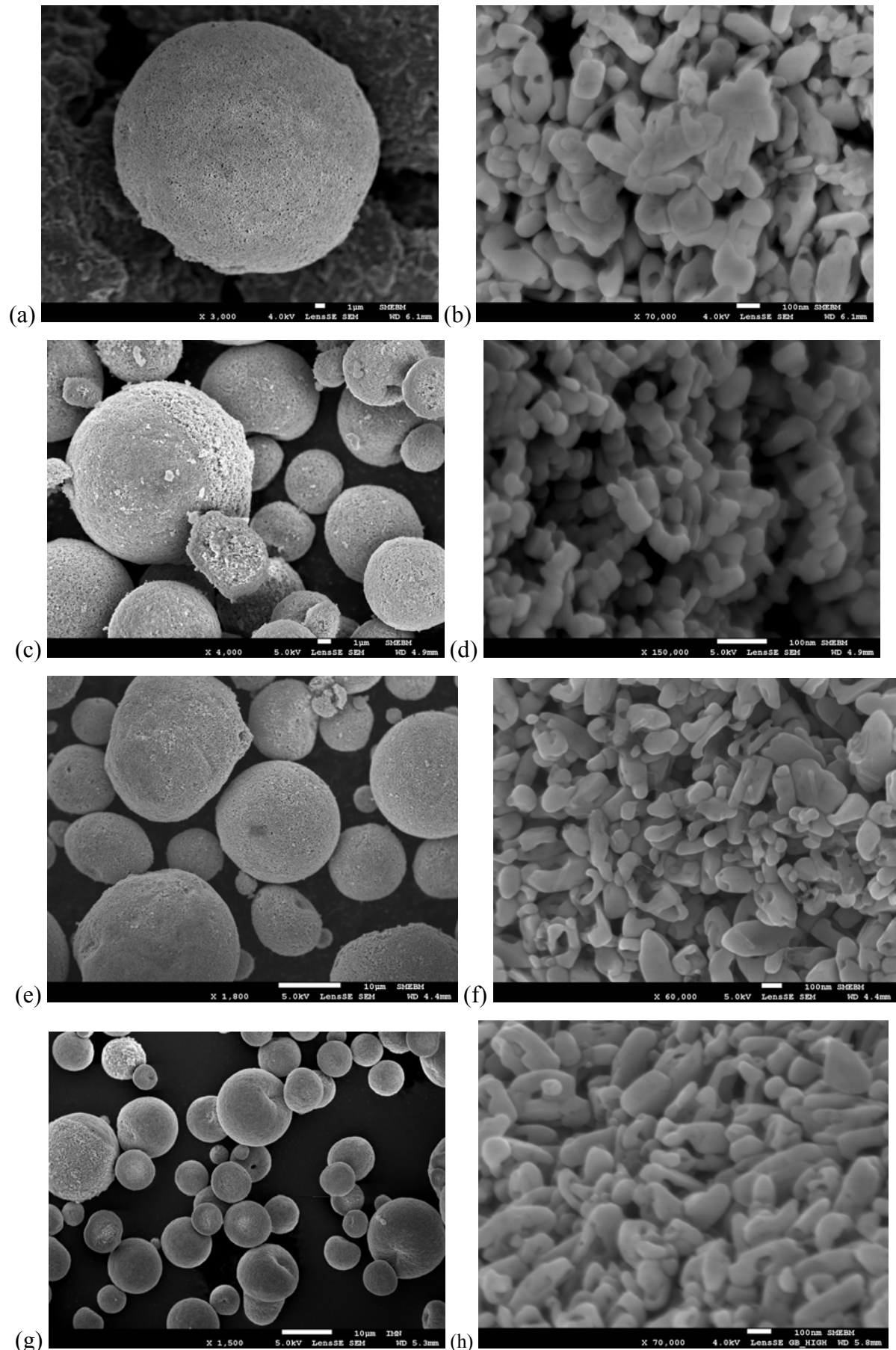


Figure 3. SEM of the LFP, CLFP1, CLFP2 and CLFP3 secondary (a, c, e, g) and primary (b, d, f, h) particles.

The particle size distribution measurements were also carried out on the same samples using a zeta seizer. The sample powders were ball milled for an hour at 500rpm with 1wt% CMC dispersant (carboxymethyl cellulose) in water (400mg of powder for 1 mL of water) in a silicon nitride vial with 3 silicon nitride balls of 1cm in diameter. With these experimental conditions, we have checked in previous works in the group that the primary particles are not broken. Only the secondary particles are disagglomerated. Thus we expect here revealing (or not) clusters of few primary particles that are tightly bound.. A drop of the recovered slurry was diluted in ultrapure water and dispersed using ultrasound for 20 minutes to disperse the clusters/particles sufficiently for measurement. The results showed two groups for each sample (Figure 4), the primary and small clusters of particles (the primary particles likely bound by the carbon coating). This supports the finding in the SEM which evidenced clusters (particles agglomerated by the carbon coating surrounding layer).

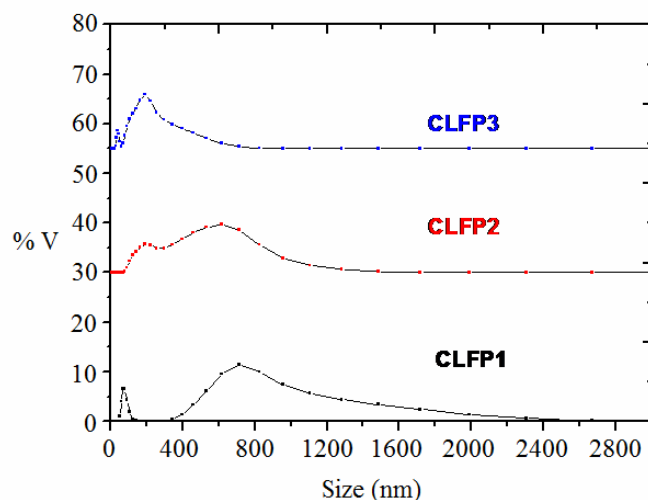


Figure 4. Particle size distribution as measured by the zeta sizer.

High resolution transmission electronic microscope (HRTEM) studies were performed with a TEM-Field Emission Gun (FEG) Hitachi HF2000 operated at 200 kV, and spectra were recorded using a modified GATAN 666 parallel spectrometer, equipped with a CCD camera. Powders were dispersed in acetone, deposited onto a holey carbon grid and then placed on a HRTEM cooling sample holder. Prior to its introduction into the microscope, the sample holder containing the powder was placed under vacuum at 80°C for an hour to remove surface contamination. The TEM images for the samples principally showed a fairly homogeneous and continuous carbon coating around the particles (Figure 5). However, a slight difference in the thickness is observed from one sample to another (mean values are given in Table 2 later

on). On the other hand graphitic sp^2 domains are observed parallel to the particle at the edge rather than at the particle-coating interface. In addition it is clear that the sp^2 sections are separated by amorphous (non- sp^2) sections here and there.

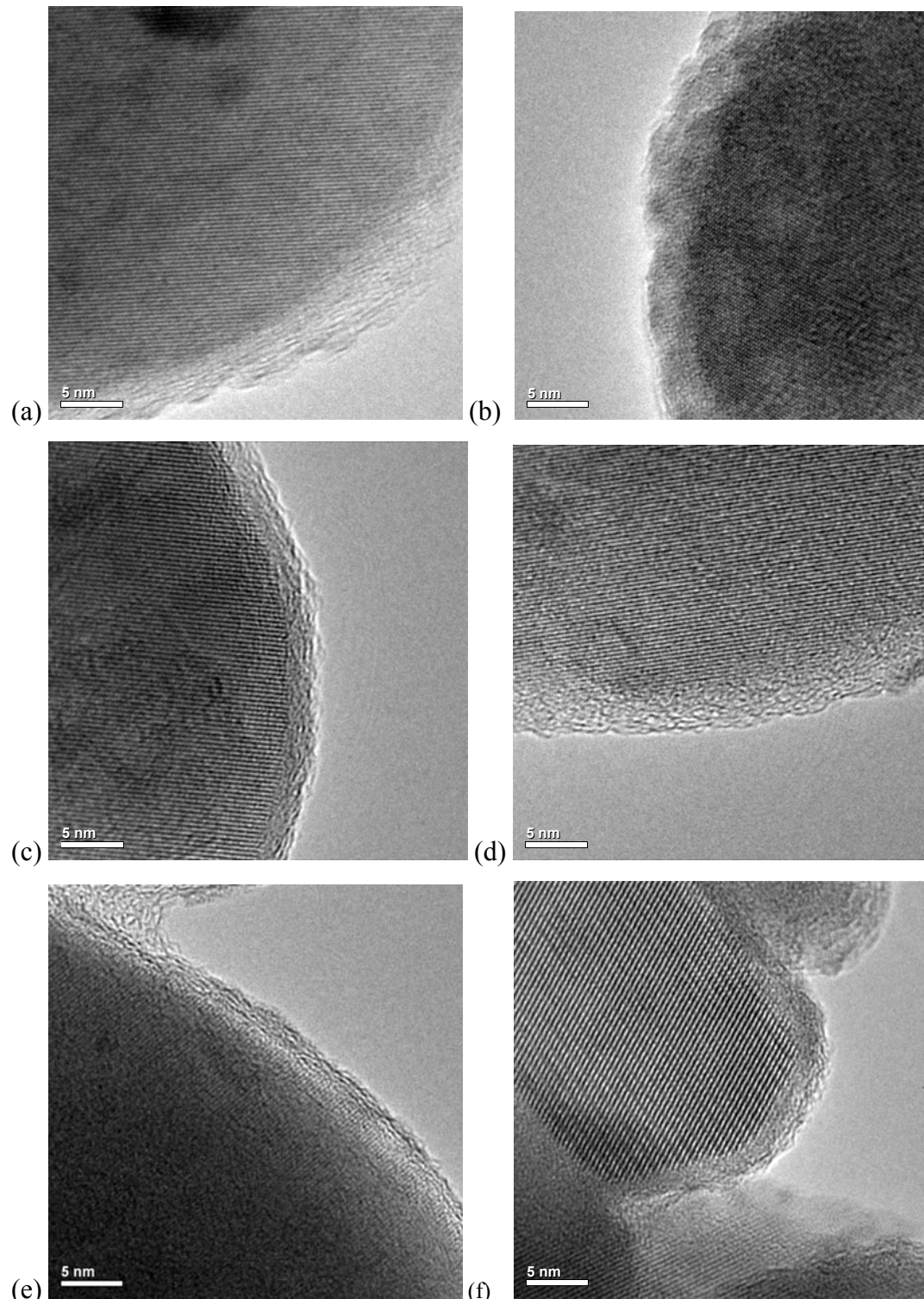


Figure 5. TEM images of the CLFP1 (a,b), CLFP2 (c,d) and CLFP3 (e,f) samples zooming on the carbon coating.

The EELS spectra acquired for the sample with the thickest carbon coating (CLF3) is shown in Figure 6. The result confirms our observation in TEM on the same sample. The existence of a sharp peak at 284eV ($1s-\pi^*$ transition) indicates a principally sp^2 hybridization in our material. Further more the second peak at 291eV ($1s-\sigma^*$ transition) is also previously reported to correspond to sp^3 type hybridization. The absence of three characteristic peaks usually related to graphite (100% sp^2 type hybridization) which are often in the energy range between 295 and 310 eV is also evident.

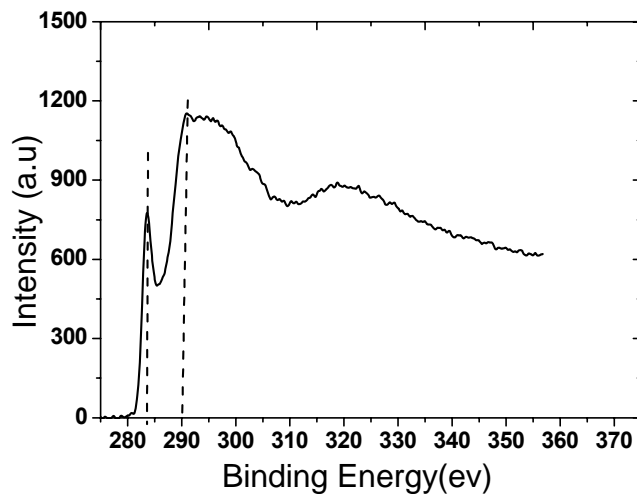


Figure 6. A representative EELS spectrum for the sample CLFP3.

The assignment of 284eV binding energy ($1s-\pi^*$ transition) and 291eV binding energy ($1s-\sigma^*$ transition) to sp^2 and sp^3 hybridization were previously reported. [93] Similarly the characteristic peaks corresponding to graphite like carbon is discussed in Reference [94].

Raman spectra were recorded using a Jobin-Yvon T64000 spectrometer. Raman spectroscopy measurements were carried out at room temperature in ambient atmosphere using an internal Cryptone 647 nm laser as the excitation source. The power of the laser beam was adjusted to 1 mW with neutral filters of various optical densities. The average acquisition time for each spectrum was 1 minute. The resulting spectrum is shown below in Figure 7. The fingerprint spectra are characteristic of an amorphous carbon. Most authors agree that the peaks at $\sim 1350\text{cm}^{-1}$, and $\sim 1600\text{cm}^{-1}$ are usually assigned to the D and G bands, which correspond to the sp^3 and sp^2 , respectively. However, there is a lot of controversy on the

[93]. S. Urbonaitė, S. Wachtmeister, C. Mirguet, E. Coronel, W.Y. Zou, S. Csillag, G. Sevenson, Carbon 45

(2007) 2047

[94]. P. Moreau, F. Boucher, G. Goglio, D. Foy, V. Mauchamp, and G. Ouvrard, Phys Rev B, 73 (2006) 195111

ability of the procedure to provide a quantitative measure of the graphene or sp^3 content. [95] So we have some reservations from using Raman spectroscopy for quantifying the sp^2 and sp^3 amounts. Raman spectroscopy in this case is used as a complimentary technique to offer qualitative information on the nature of the surface coating. At least, it indicates the existence of multiple hybridizations.

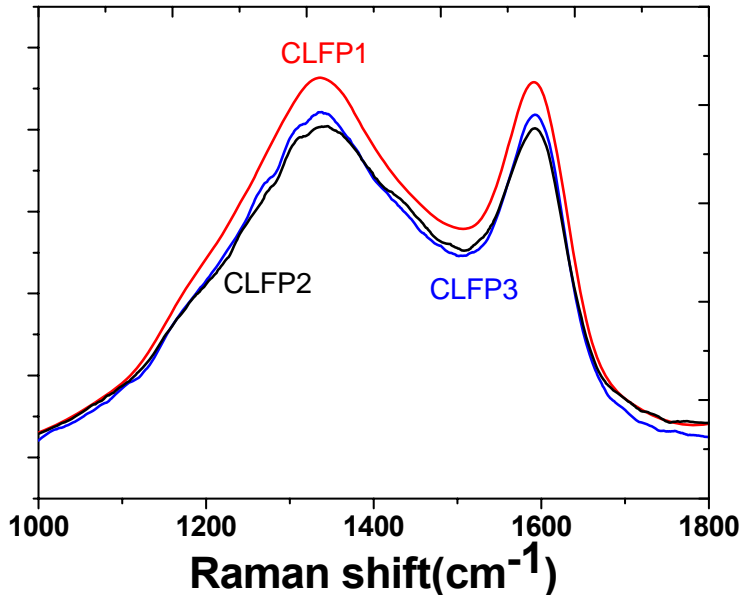


Figure 7. The fingerprint Raman spectrum for all the carbon coated samples.

X-ray photoelectron spectroscopy (XPS) technique using Kratos Axis ultra DLD was used to quantify the sp^2 and sp^3 content in the coating Figure 8. The data treatment is carried out using Casa software by decomposition of the C1s core binding energy (BE) spectra on two constituent's function corresponding to sp^2 and sp^3 hybridization states. [96,97] The sp^2 and the sp^3 hybridization states were fitted at 284.74eV and 285.63eV. Three additional peaks were introduced in the fitting of the C1s spectra which resulted from environmental oxidations. They are the C-O, C=O and COO at 286.78eV, 288.31eV and 289.40eV respectively. Similar procedure was followed in other works. [98] The percentage sp^2 was calculated taking into account all the contributions rather than just sp^2 and sp^3 . We believe considering all the resulting five components (sp^2 , sp^3 , C-O, C=O, COO) for the calculation of the % sp^2 is the best representation of the reality. However often in publications only sp^2 and

[95]. James D.Wilcox Marca M.Deoff,Marek Marcinek and Roberet kostecki,Journal of the electrochemical society, 154(5)A389-A395(2007).

[96]. E. Riedo, F. Comin, J. Chevrier, F. Schmithusen, S. Decossas, M. Sancrotti, Surf. Coat. Technol. 125 (2000) 124.

[97]. J. Díaz, G. Paolicelli, S. Ferrer, F. Comin, Phys. Rev., B, 54 (1996) 8064.

[98]. M. Raybachuk, J.M. Bell, Thin solid films, 515(2007)7855

sp^3 are considered in the calculation of the % sp^2 , ignoring the other components (C-O, C=O, COO). In addition measurements were done after 2 years to confirm the reproducibility of the measurements and less than 1% difference was observed between the measurements signalling minimal evolution of the material when stored in a glove box. Further more, several other characterizations were carried out to assess different physical and structural properties of the materials. The results are presented in Appendix 1.

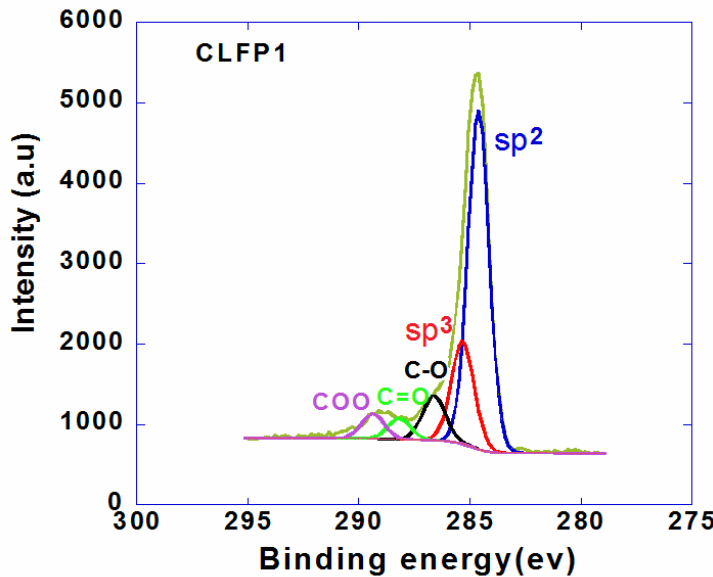


Figure 8. A representative XPS spectrum (300-275 eV) in the region of C1s as well as additional contributions of the spectrum peak for the CLFP1 sample.

2.2. The Sample preparation for BDS measurements

Samples preparation: Due to the specification of the sample holder (a precision coaxial connector (APC7mm)) in the BDS measurements cylindrical samples are required. The cylindrical samples are compacted active material powders at 510 MPa by using a pelletizer (Ets Canaple) (Figure 9a-c). Metallic contacts are made by applying and drying conductive Ag or Au paste (Oxford Instruments) directly on both front faces of the pellet. Figure 9d-e shows the SEM images of the two metallization types (Ag/Au). A flak-like morphology is observed for the Silver painted samples whereas a colloidal morphology is observed in the gold painted ones. After painting with the silver paint, the sample is dried under vacuum at 120°C for 2hrs to extract most of the adsorbed humidity. The pellets are then transferred to a hermetic container inside the glove box to facilitate a safe (contamination free) transport. The

only exposure to humidity the pellets will face is during the transfer from the hermetic container to the BDS measurements cell which usually lasts less than 30 seconds under normal conditions.

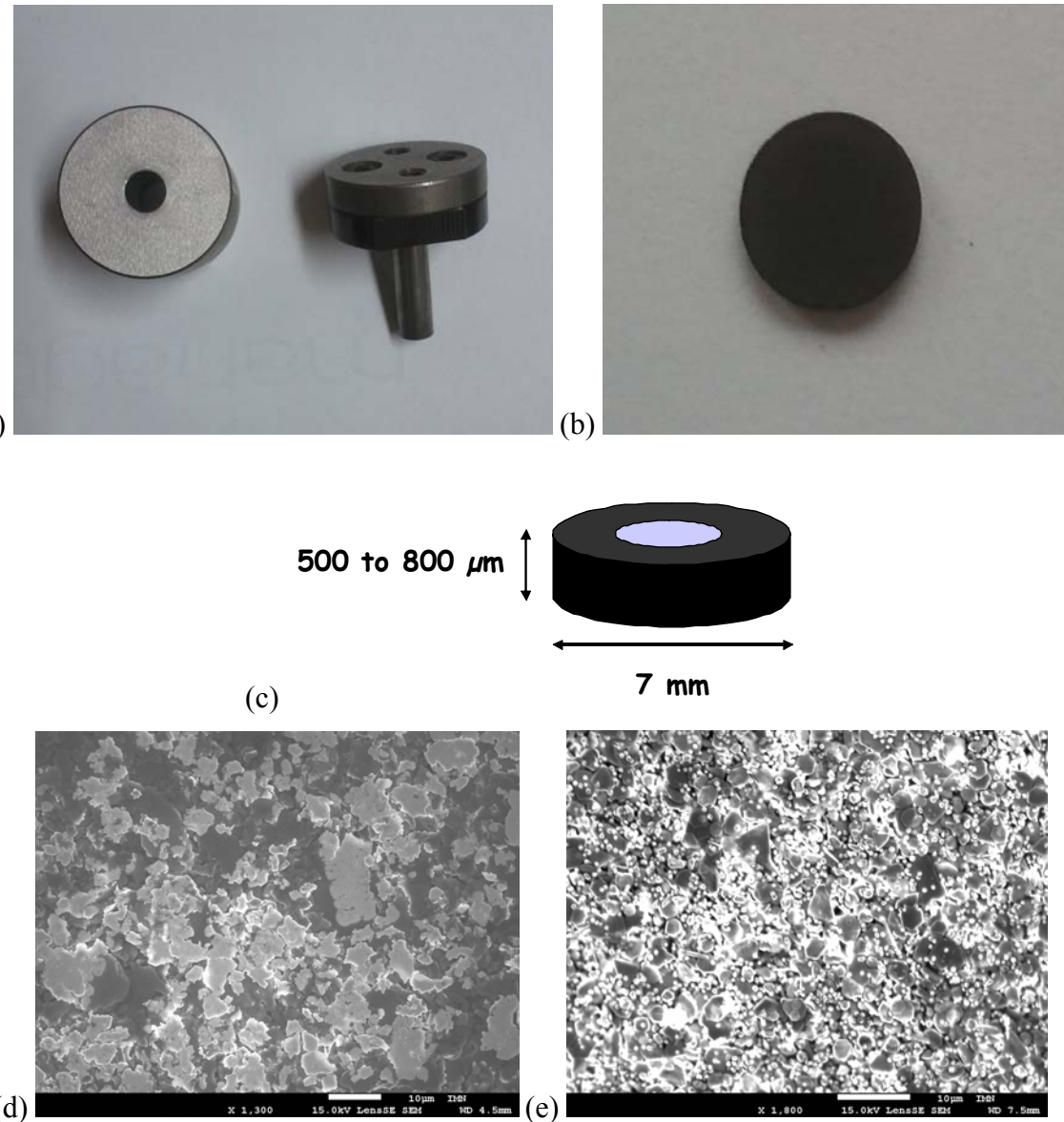


Figure 9. (a) The Pelletizer. (b) The actual image of the pellet prepared. (c) The dimensions of the pellet and the silver metallization. SEM image of silver painted (d) and gold painted (e) front face.

Before going into the results section, the measured/calculated %sp² as well as some other important parameters (particle size, coating thickness, carbon volume fraction per clusters, sample porosity) are summarized in Table 2 below.

Table 2. Mean particle and cluster sizes, sample porosity, carbon coating thickness, sp²% in the coating and coating volume fraction per cluster of the different samples. sp² type carbon volume fraction determined from XPS measurements. Coating thickness measured by TEM. Cluster size from zeta sizer measurements. Sample porosity determined from the consideration of the volume fraction of each component and the actual volume of the electrode. On the other hand the Carbon volume fraction calculated using the equation given below

$$\Phi_{vc} = (1 - \Phi_{porosity}) * \frac{(m_{wc}/\rho_c)}{(m_{wc}/\rho_c) + (m_{LFP}/\rho_{LFP})} \quad \text{where } \Phi_{vc} \text{ is the carbon volume fraction, } \Phi_{porosity} \text{ is the pellet porosity, } m_{wc} \text{ is the mass of carbon in the pellet, } m_{LFP} \text{ is the mass of the LFP in the pellet, } \rho_c \text{ is the density of carbon, } \rho_{LFP} \text{ is the density of LFP.}$$

porosity, m_{wc} is the mass of carbon in the pellet, m_{LFP} is the mass of the LFP in the pellet, ρ_c is the density of carbon, ρ_{LFP} is the density of LFP.

Sample	Particle size (nm)	Cluster size (μm)	Sample porosity ϕ_p (%)	Coating thickness (nm)	sp ² percent in the coating	Carbon volume fraction per cluster ϕ_{cc}
LFP	150		47	-	-	-
CLFP1	50	0.4-2.0	45	3.00	64	3.8×10^{-2}
CLFP2	150	0.4-1.2	40	2.80	52	3.0×10^{-2}
CLFP3	150	0.4-0.6	48	4.60	70	3.6×10^{-2}

Broadband Dielectric Spectroscopy (BDS) measurement: Complex resistivity and permittivity spectra were recorded over a broad frequency range 40 to 10^{10} Hz, using simultaneously an impedance analyzer (Agilent 4294 from 40 to 1.1×10^8 Hz) and a network analyzer (HP 8510 from 4.5×10^7 to 10^{10} Hz) Figure 10. The experimental device, fully described in chapter 1 and references [99,100], consists of a coaxial cell (APC7 standard) in which the cylindrically shaped sample with silver plated front faces, fills the gap between the inner conductor and a short circuit. The sample has the same diameter as (7 mm) that of the outer conductor of the coaxial cell. After a relevant calibration of the analyzers, the complex (relative) permittivity $\epsilon(\omega) = \epsilon'(\omega) - i\epsilon''(\omega)$ of the sample is computed from its admittance Y_s . Complete dielectric spectra were made from about 400 measurements with an accuracy of approximately 3 to 5% in the experimental frequency range. The knowledge of the complex permittivity enables the calculation of the complex conductivity $\sigma = \sigma' + i\sigma'' = i\omega\epsilon_0\epsilon$ (ϵ_0 being the vacuum permittivity) and resistivity $\rho = \sigma^{-1}$. Temperature measurements were made under a dry N₂ flow in the range 200 to 400K.

[99]. N.E. Belhadj-Tahar, A. Fourrier-Lamer, IEEE Trans. Microwaves Theory and Tech., 39-10 (1991) 1718.

[100]. S. Berthumeyrie, J.C. Badot, J.P. Pereira-Ramos, O. Dubrunfaut, S. Bach, and Ph. Vermaut, J. Phys. Chem. C, 114 (2010) 19803.



Figure 10. The experimental device consisting of a network (left) analyzer and an impedance analyzer (right).

2.3. Electrical measurements: identification of the different relaxations and their attributions (the electronic conductivity mechanisms).

Following the preparation of the samples, Complex resistivity and permittivity spectra were recorded over a broad frequency range 40 to 10^{10} Hz. As described above the samples have silver plated front faces in order to ensure good contacts between the samples and the experimental device. However, since the silver deposited on the sample surface is a blocking electrode for the lithium ions, the dc-conductivity will be only due to electron transfer with an accumulation of lithium ions at the silver electrodes. The Activation energy for conductivity will thus be owing to a strong Li^+ (vacancy)-hole polaron binding energy (i.e. 0.50 eV) in LiFePO_4 .

The frequency dependence of the real parts of the conductivity and of the permittivity for LiFePO_4 (LFP) at room temperature is shown in Figure 11a and b respectively. The lowest measured value is about 10^{-7}S.m^{-1} at 40Hz and the lack of dc-conductivity plateau shows that our set-up does not allow accessing to the very low value of the dc-conductivity.

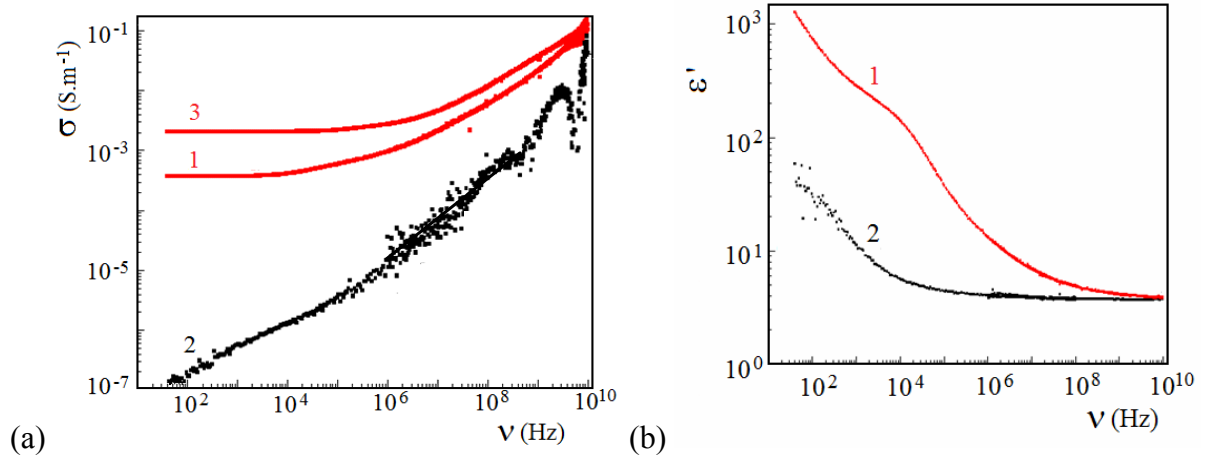


Figure 11. Real parts of the conductivity (a) and of the permittivity (b) as a function of the frequency for both carbon-coated and uncoated samples, i.e. CLFP3 (curve 1) and LFP (curve 2), at 298K. In (a) the real part of the conductivity is also given at 398K for CLFP3 (curve 3).

Figure 11b shows also the existence of a dielectric relaxation around 10^2 Hz at room temperature because ϵ' value is decreasing from 40 to a constant value equal to 4 at higher frequencies (i.e. above 10^6 Hz). This relaxation would be due to cluster boundary or to silver/sample interface. Above 10^5 Hz, the frequency dependence of LiFePO₄ conductivity follows a power law:

$$\sigma = A\omega^s \quad (2.2)$$

where A and s are fitting parameters. The value of the exponent s is equal to 0.75 and thus describes a variable range hopping (VRH) conduction mechanism[101]. This describes electrical conduction in disordered systems with localized sites randomly distributed in the crystal network. [102] In this case, the hopping probability depends on the spatial separation of the sites.

The carbon coating in C-LiFePO₄ drastically increases the electrical conductivity in the whole frequency range (Figures 11a). At 298K, the dc-conductivity σ_S of the sample has a value of more than 10^{-4} S.m⁻¹ below 10^5 Hz and the high frequency conductivity reaches almost 10^{-1} S.m⁻¹ in the GHz region. This type of frequency dependence shows that in the composite C-LiFePO₄ the carbon-coating constitutes continuous conducting paths spanning

[101].N.F. Mott, Phil. Mag. 19 (1969) 835

[102]. N. F. Mott and E. A. Davis, Electronic Processes in Non-Crystalline Materials, 2nd Ed. (Oxford University Press, Oxford, UK, 1979).

throughout the sample. [103] This situation can be realized with a small volume fraction of conductor owing to the core-shell morphology of the carbon-coated LiFePO₄ material. [104,105] The disappearance of the power law evolution in the CLFP3 sample confirms the dominant role of the coating with the existence of one or more relaxation domains above 0.1MHz (Fig. 11a). Figure 11b shows the existence of a low frequency relaxation around 10⁴ Hz for CLFP3, which is due to its higher conductivity σ_s correlated to the presence of the carbon-coating. At the highest frequencies, C-LiFePO₄ and LiFePO₄ permittivities converge to a frequency independent residual permittivity ϵ_∞ corresponding to the effective (bulk) permittivity of LiFePO₄ (LFP). Indeed, in CLFP3, the volume fraction of the carbon coating is too small in the sample to play significantly on the residual permittivity(ϵ_∞).

The type of metallization (i.e. silver and gold paints) affects the spectra at frequencies below 10⁶ Hz Figure 12a-b. The measurements reported in Figure 11 and Figure 13 were performed on two different batches of CLFP3 (See Appendix 1, Table 1). The lower dc conductivity in Figure 13 compared to Figure 11 is due to the lower sp² content of the second CLFP3 batch.

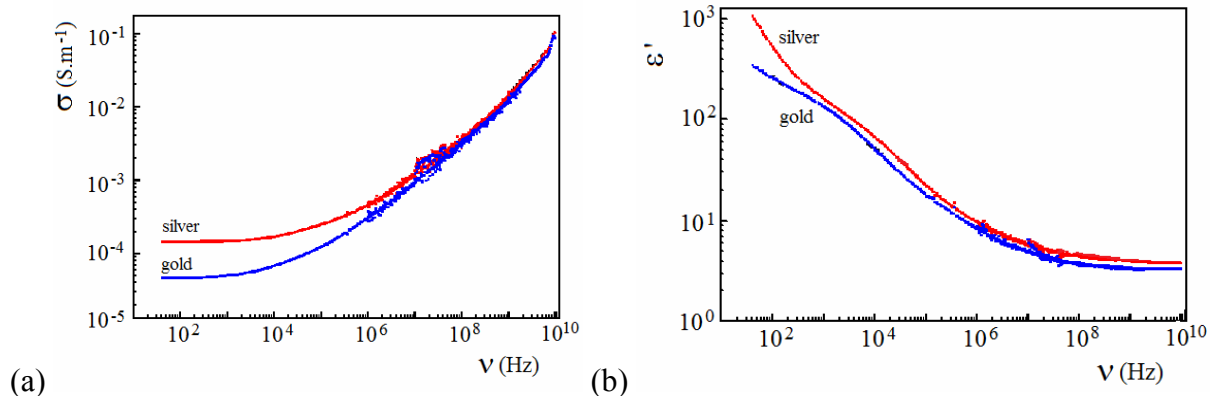


Figure 12. Real parts of the conductivity (a) and of the permittivity (b) as a function of the frequency and for different metallization type, for carbon-coated CLFP3, at 298K.

The difference in the spectra could most likely be a result of a difference in work function of the metals with that of amorphous carbon coating covering the LFP particles. Since the work functions of the silver and the amorphous carbon are almost similar, the silver metallization is more favorable for the electric measurements of C-LiFePO₄. [106] In the low

[103]. R. Pelster, G. Nimtz, B. Wessling, Phys. Rev. B , 49 (1994) 12718

[104]. C. Chiteme and D.S. McLachlan, Physica B 279 (2000) 69

[105]. J. Mozkon, R. Dominko, R. Cerc-Korosec, M. Gaberscek, J. Jamnik, J. Power Sources, 174 (2007) 683

[106]. B. Sun, P.E. Colarita, H. Kim, M. Lockett, M.S.Marcus, L.M. Smith, R.J. Hamers, Langmuir 2006, 22, 9598.

frequency range, the electrical properties of the sample are thus affected by the sample/metal interface. Moreover, for frequencies above 10^6 Hz, the dielectric spectra correspond to the intrinsic spectra of the composite sample because they are not depending on the nature of the metallization. The dielectric relaxation which appears around 10^4 Hz at room temperature (in the case of CLFP3) is thus due to the interfacial polarization resulting from the sample /metal contact. At the highest frequencies, the negligible evolution of the conductivity vs. the temperature would indicate a quasi-metallic behavior in the carbon-coating Figure 11a. Different conductivity levels could exist at different size levels from the macroscopic one (lower frequencies) to the local one (higher frequencies). Long-range electron transfer at macroscopic scale takes place via a higher energy barriers than that at local scale since it undergoes sample discontinuities (particles, clusters boundaries and junctions). However, different transfer mechanisms can be observed at the different scales of composite systems. [107]

As the possible dielectric relaxations are not clearly seen in frequency-dependent representation, it is more suitable to use the Nyquist plots (discussed in chapter 1) that offer an easier decomposition of the dielectric spectra. Since all the polarizations at different scales are additive owing to their vector character, their contributions (relaxations) can thus be evidenced by a decomposition procedure of the Nyquist plots (ϵ'' vs. ϵ' and ρ'' vs. ρ'). [108] This procedure, which is applied to the recorded data by home-made software, is obtained by successive subtractions of the different contributions from low to high frequencies. Dielectric relaxations are often described by the complex Cole-Cole function (hereafter called CC-function),

$$\epsilon(\omega) = \epsilon_H + \frac{\epsilon_L - \epsilon_H}{1 + (i\omega\tau_\epsilon)^{1-\alpha}} \quad (2.3)$$

where ϵ_L and ϵ_H are respectively the low- and high-frequency limits of the permittivity and τ_ϵ is the mean relaxation time (relaxation frequency, $v_\epsilon = (2\pi\tau_\epsilon)^{-1}$). The strength of the relaxation is $\Delta\epsilon = (\epsilon_L - \epsilon_H)$. The fitting parameter α ranges between 0 and 1 and determines the degree of deviation from the ideal Debye response for which $\alpha = 0$. Note that the Debye expression corresponds to the occurrence of a single relaxation time (described in chapter1). When $0 < \alpha$

[107]. J.C. Badot, E. Ligneel, B. Lestriez, D. Guyomard, O. Dubrunfaut, Adv. Funct. Mater., 19, 2749 (2009).
[108]. A. von Hippel, Dielectrics and Waves (Wiley, New York, 1952).

< 1 , the Cole-Cole function is described by a continuous distribution $G_\varepsilon(\tau)$ of the relaxation times which has a maximum at $\tau = \tau_\varepsilon$ and becomes broader as values of α increase. In a similar manner, resistivity relaxation functions are similar to the CC-function (Eq. 3) and are therefore given by,

$$\rho(\omega) = \rho_H + \frac{\rho_L - \rho_H}{1 + (i\omega\tau_p)^{1-\alpha}} \quad (2.4)$$

with ρ_L and ρ_H respectively the low- and high-frequency limits of the resistivity and τ_p a (resistivity) relaxation time. Here, the Cole-Cole function is due to the existence of a continuous distribution $G_\rho(\tau)$ of the relaxation times as a result of a distribution of contact resistances and capacitances.

In practice, complex resistivity plots are useful to determine the grain (crystallite) bulk dc conductivity in powdered compounds. However, they can also be used to obtain the conductivity at different scales of the sample (sample and aggregates conductivities). Complex resistivity plots are complementary to complex permittivity plots in order to establish some correlation between conductivities and dielectric relaxation frequencies.

Furthermore, in order to investigate the correlation between the electric conduction mechanisms and the nature of charge carriers, the temperature dependences of the conductivity and of the different dielectric relaxation frequencies are of crucial interest. Obtained activation energies and frequency prefactors often provide some indications on the charge carrier behaviours.

Figure 13a shows the entire Nyquist (Cole-Cole) plot, i.e. ε'' vs. ε' of CLFP3 (in the low-frequency part of the dielectric spectrum at 300 K. The first dispersion domain (D1) is fitted with a good precision by a straight line, which correspond to a v^{n-1} frequency response of the complex permittivity with an exponent n of about 0.14 whatever the sample and the temperature. Upon subtracting this low frequency contribution, a second dispersion domain D2 (Figure 13b) is evidenced and well fitted by a circular arc corresponding to dielectric relaxations described by the CC-function (see Eq. 2.3). The relaxation domain D3 (Figure 13c) is unambiguously defined after subtracting the contributions D2 and is also described by the CC-function. By the same procedure, the relaxations D4 (Figure 13d) is obtained.

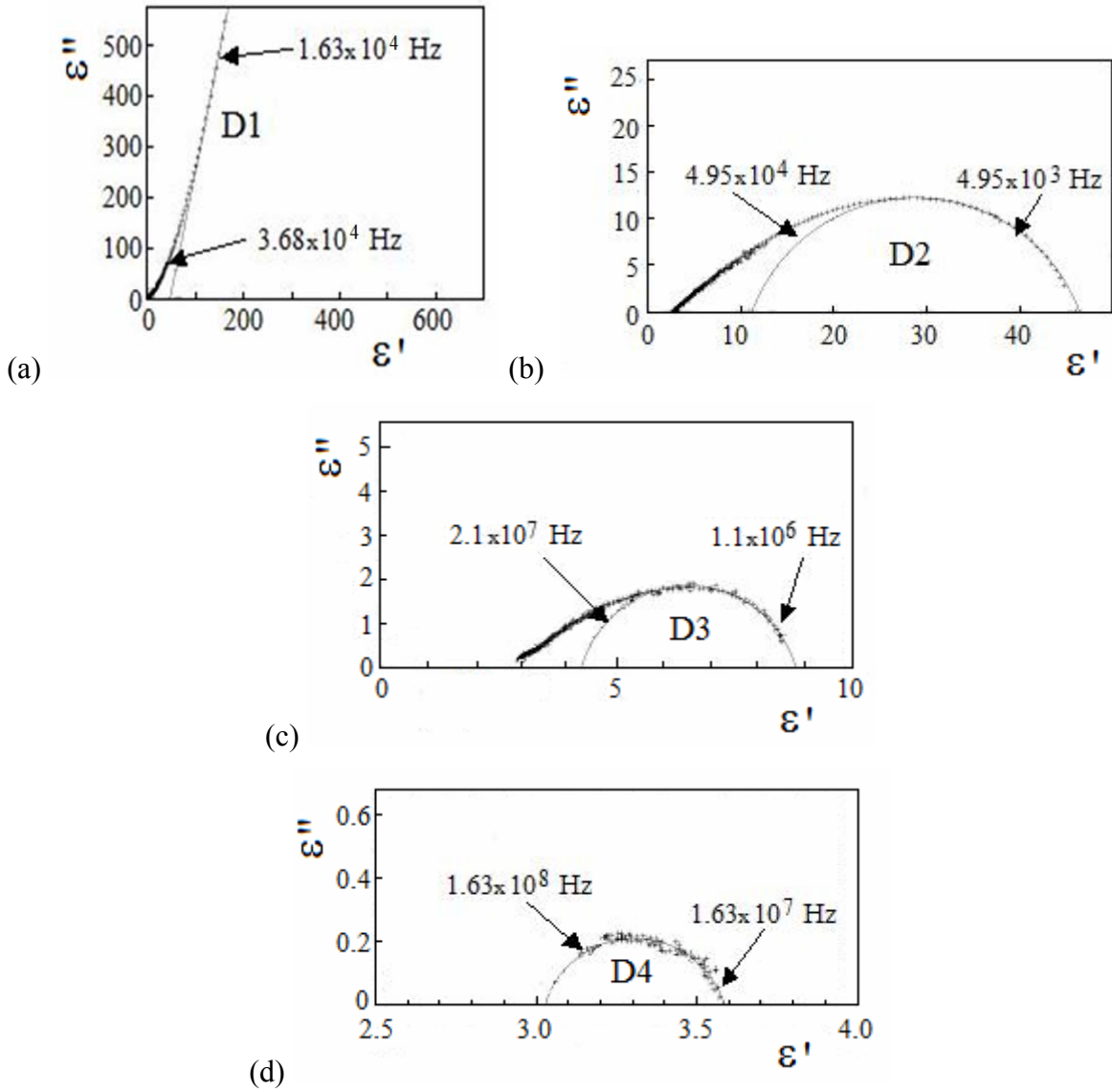


Figure 13. (a) to (d) Cole–Cole plots of the imaginary part $\epsilon''(v)$ vs. the real part $\epsilon'(v)$ of the complex permittivity at 298 K for CLFP3: (a) Entire plot from 40 to 10^{10} Hz: only the contribution (D1) of the low frequency conductivity represented by a straight line is visible; (b) Plot obtained after subtracting the contribution D1 and evidence of relaxation D2; (c) Plot obtained after subtracting the contribution of the relaxation D2 and evidence of relaxation D3; (d) Plot obtained after subtracting the contribution of the relaxation D3 and evidence of relaxation D4.

In the other samples (except LFP), the decomposition of the plots allows identifying also four dielectric domains (three of whom being relaxations) from D1 to D4. The different values of the α parameters (α_2 , α_3 and α_4), relaxation strengths ($\Delta\epsilon_2$, $\Delta\epsilon_3$ and $\Delta\epsilon_4$), relaxation frequencies (v_2 , v_3 and v_4) and their corresponding prefactors (v_{02} , v_{03} and v_{04}) are summarized in Table 3.

Table 3. Conductivity σ_i , activation energy E_i , dielectric relaxation frequency v_i at room temperature, frequency prefactor v_{0i} , dielectric strength $\Delta\epsilon_i$ and α_i parameter associated with the polarization sources within the different samples: hopping between the sp²-carbon domains (D4), cluster (D3) and interfacial (D2) polarizations.

	Interfacial polarization D2	Clusters polarization D3	sp ² domains (hopping) D4	Residual permittivity ϵ_∞	Conductivity (S.m ⁻¹)			
Sample	v_2 (Hz)	v_3 (Hz)	v_4 (Hz)		σ_S	Sample	Cluster	sp2
	v_{02} (Hz)	v_{03} (Hz)	v_{04} (Hz)			E_S (eV)	E_{CL} (eV)	^{a)} σ_{sp2e}
CLFP1	$\Delta\epsilon_2$	$\Delta\epsilon_3$	$\Delta\epsilon_4$	3.28	4.5x10 ⁻⁴	1.2x10 ⁻²	38	
	α_2	α_3	α_4					
	6.0x10 ⁴	2.0x10 ⁶	3.5x10 ⁷					
	1.5x10 ⁸	1.2x10 ⁸	2x10 ⁸					
	0.20	0.12	0.04					
CLFP2	84	7	2	3.40	1.3x10 ⁻³	1.0x10 ⁻²	32	
	0.09	0.18	0.26					
	1.7x10 ⁴	2.7x10 ⁵	1.5x10 ⁷					
	6x10 ⁷	2.0x10 ⁸	2x10 ⁸					
	0.21	0.16	0.05					
CLFP3	6.90	4.5	1.08	3.05	9.1x10 ⁻⁴	2.5 x10 ⁻²	41	
	0.01	0.2	0.18					
	1.7x10 ⁴	5x10 ⁶	1.5x10 ⁸					
	3x10 ⁸	2x10 ⁸	5x10 ⁸					
	0.22	0.09	0.03					
	39	4.5	0.58		0.16	0.16	41	
	0.24	0.18	0.10					

All the relaxation frequencies v_i ($i = 2, 3$ and 4) have thermally activated behaviors, and can be described by Arrhenius behavior.

$$v_i = v_{0i} \exp\left(-\frac{E_i}{kT}\right) \quad (2.5)$$

Where v_{0i} is the frequency prefactor, E_i the activation energy, k the Boltzmann constant ($k = 1.38 \times 10^{-23}$ J.K⁻¹) and T the temperature (Figure 14) recaps the activation energy that characterizes each dielectric relaxation in the different samples.

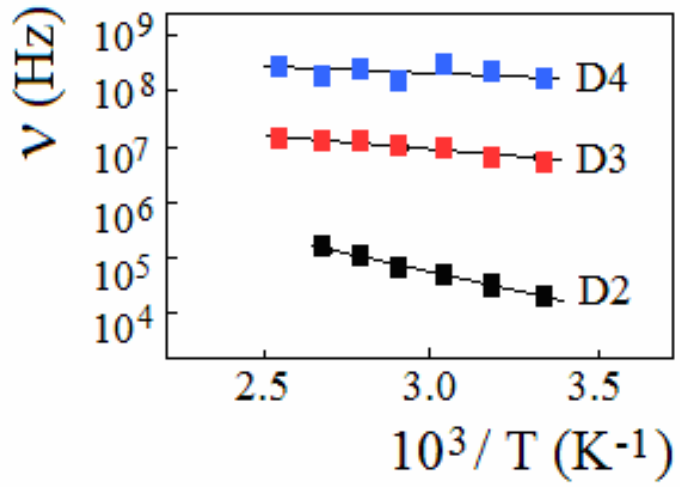


Figure 14. (a) Relaxation frequencies of the different relaxations (D2, D3 and D4) as functions of inverse temperature in CLFP3.

Dispersion domains (D1) and (D2) occur at frequencies lower than 10^6 Hz (at room temperature) and depend on the metallization, as previously observed in Figure 12a. (D2) is a dielectric relaxation due to the existence of an interfacial polarization at the junction sample/silver, which is often called a Schottky barrier. The result is the buildup of a positively charged depletion region in the sample (i.e. amorphous carbon coating). The response of the created space-charge to an alternating electric field is a dielectric relaxation which generally occurs in the low-frequency domain. The relaxation frequency depends on the width and the capacitance of the Schottky barrier. Moreover, The dispersion domain (D1) describes the frequency power law for permittivity, i.e. $\epsilon(\omega) = B(i\omega)^{-0.86}$ whatever the temperature. This behavior can be explained by the roughness of the sample due to its high porosity (40 to 50%). It results a contact (sample/Ag) area smaller than the sample geometrical surface which could create slight frequency dependence (i.e. a quasi-dc conductivity behavior).

Higher frequency dispersion domains (D3) and (D4) are polarizations generated within the sample because they occur at frequencies above 10^6 Hz at room temperature. It has to be noted that the samples are constituted of clusters in which the particles are bound/stuck together by the carbon coating layer (Figure 3 & Figure 4). The later forms a continuous network within the cluster and is constituted of sp^2 conducting domains separated by insulating sp^3 gaps. We have thus two polarization levels in the samples: (a) the first one (larger scale) being the cluster and (b) the second one (smaller scale) involving the mean

distance between the sp^2 domains. As it involves longer distances for charge transport, the cluster polarization occurs thus at lower frequency and gives rise to the relaxation (D3). The faster relaxation (D4) is due to the hopping from sp^2 domain to another via the sp^3 gap along the particles Figure 15.

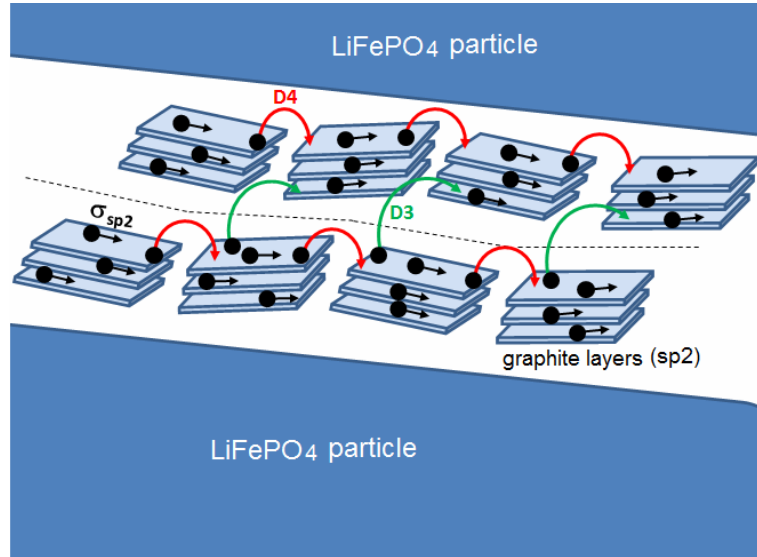


Figure 15. The schematic phenomenological description of dielectric relaxations D3 and D4.

The relaxation frequency ν_4 of (D4) has activation energy E_4 between 0.03 and 0.05 eV and a prefactor ν_{04} with a mean value around 3×10^8 Hz (Table 3). The activation energy E_4 of the frequency ν_4 is the hopping barrier between two sp^2 domains via sp^3 gap. According to Mott and Davis, [102] the electronic transport in the amorphous carbon is governed by hopping between domains of sp^2 -carbon. The hopping frequency (or probability) from an occupied site to unoccupied site depends on the overlap of the electronic wave functions on the two sites. This frequency is given by

$$\nu = \nu_{ph} \exp(-2\alpha r) \exp\left(-\frac{E}{kT}\right) \quad (2.6)$$

where ν_{ph} is the phonon frequency, r the separation between sp^2 domains, E the energy difference (e.g. E_4) between the localized sites and α^{-1} the localization length characterizing the spatial extension of the electronic wave function. The order of magnitude of the mean

frequency prefactor $v_0 = v_{ph} \exp(-2\alpha r) \approx 3 \times 10^8$ Hz can be justified if $\alpha^{-1} \ll r$. Hence, the small value of v_{04} could be due to a localization of the electrons within sp^2 domains. Moreover, we must interpret the origin of E_3 which is the activation energy of the characteristic frequency of cluster polarization. Figure 16 shows that the two activation energies E_3 and E_4 are decreasing functions of the sp^2 content. The activation energy E_3 higher than E_4 can be interpreted as the interparticle barrier for charge transport in the coating at the cluster scale.

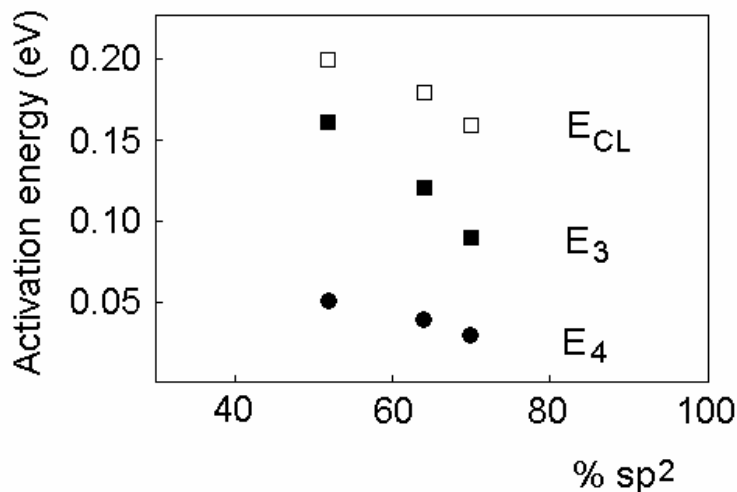


Figure 16. Activation energies E_{CL} , E_3 and E_4 vs. carbon- sp^2 content (% sp^2) in the coating for the cluster conductivity, the relaxation frequencies of D3 (cluster polarization) and D4 (local hopping between sp^2 domains), respectively.

The electron which hops along a particle over a barrier E_4 can also hop towards another particle pertaining to the same cluster over a barrier E_3 . The latter energy is higher because the separation between sp^2 domains is larger between two neighboring particles. The two energies E_3 and E_4 are correlated since $E_3 \approx 3E_4$. This behavior could be explained by a homothetic variation of the distances between the sp^2 domains.

In another way, Table 3 shows that D2 has a relaxation frequency prefactor similar to that of the D3 and D4 relaxations. By comparing D2 with D3 and D4, the only difference is higher activation energy, i.e. $E_2 > E_3 > E_4$. This phenomenon can be attributed to the hopping of the trapped electrons in the coating at the vicinity of the interface silver/sample.

The entire resistivity Nyquist plot (ρ'' vs. ρ') of CLFP3 at 300 K is depicted in Figure 17. To provide evidence for the different resistivity relaxations, we used decomposition procedure of the Nyquist plots as for the complex permittivity diagrams. The first dispersion domain R1 is well fitted by a circular arc in the low-frequency part of the plot and thus

described by the complex CC-function (Eq. 2.4). R1 crosses the real axis ρ' at ρ_{SM} (low-frequency limit) and at ρ_S (high-frequency limit). After subtraction of the domain R1, the higher frequency contribution R2 is evidenced (Figure 17a) and also fitted by a circular arc described by Eq. 2.4. R2 crosses the real axis at ρ_S (low-frequency limit) and at ρ_{CLE} (high-frequency limit). The incremental resistivities $\Delta\rho_1$ and $\Delta\rho_2$ of R1 and R2 correspond to the sample/ag interface and to the clusters junction resistances, respectively. ρ_S and ρ_{CLE} correspond to the sample and cluster resistivities, respectively.

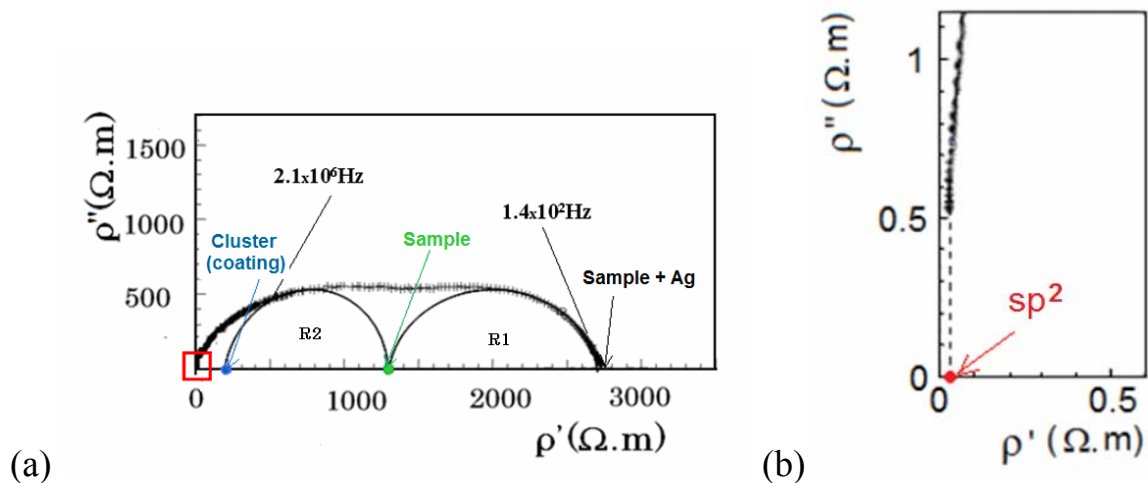


Figure 17. (a) Nyquist plot of the imaginary part $\rho''(v)$ vs. the real part $\rho'(v)$ of the complex resistivity at 298 K for CLFP3 (c-LiFePO₄); (b) zoom of the high frequency part of the plot (determination of sp² effective conductivity).

We can consider that the cluster conductivity σ_{CLE} is governed by the coating conductivity σ_{co} because the coating constitutes continuous pathways in the clusters. Hence, their electrical behaviors can be similar, the cluster conductivity corresponding to the effective value of the coating conductivity. Moreover, the zoom of the high frequency part of the complex resistivity plot permits to determine the effective resistivity of the sp² domains ρ_{sp2e} (Figure 17b). The latter assumption is fully supported by the nearly metallic behaviour observed in this frequency range (Figure 11a.). Similar resistivity diagrams were obtained whatever the sample and temperature, in the range 180 to 300K. Table 3 recaps all the conductivity values at room temperature: $\sigma_S = (\rho_S)^{-1}$ is the sample conductivity, $\sigma_{CLE} = (\rho_{CLE})^{-1}$ corresponds to the effective cluster conductivity and σ_{sp2e} corresponds to the effective conductivity of sp² domains. Except σ_S , all values σ_{CLE} and σ_{sp2e} are effective because they depend on the volume fractions.

The resulting temperature dependence of the different conductivities σ_s , σ_{CLE} and $\sigma_{\text{sp}2e}$ is shown in Figure 18. The nearly temperature-independent conductivity (absence of activation energy) for $\sigma_{\text{sp}2e}$ indicates metal like behavior, as expected for carbon-sp² domains. Owing to its order of magnitude, $\sigma_{\text{sp}2e}$ corresponds to effective conductivity of the carbon-sp² domain, the sp² content in the coating and the sample being very low (Table 2). The reasonably good linear fit of $\ln \sigma$ vs. T^{-1} demonstrates a simple thermally activated conduction for clusters and sample conductivities in the narrow temperature range 200-400K.

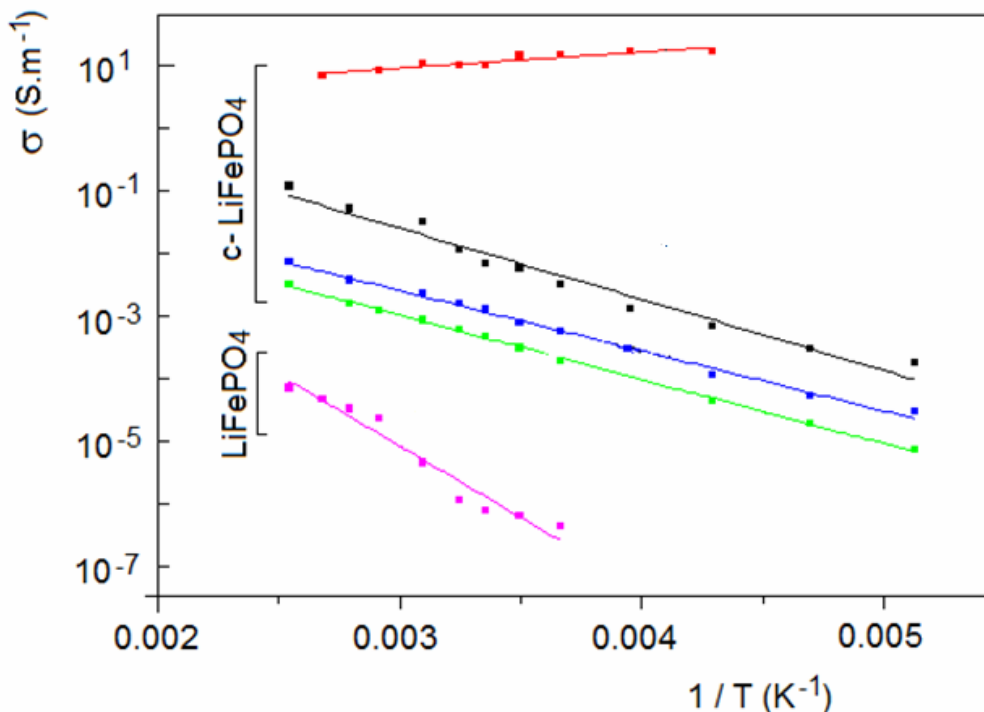


Figure 18. Figure 18, the legend (colors are missing) → “Conductivities vs. inverse temperature T^{-1} for CLFP2 (C-LiFePO₄: sample + Ag ■, sample ▲, cluster ▨ and sp2 ▢) and LFP (LiFePO₄: sample □)..

Despite the different values of the conductivities, the activation energies are similar, i.e. $E_{\text{CL}} \approx E_s$ (Figure 18). This indicates that the charge carriers and transport mechanisms are the same from the coating to the sample scale, likely because intercluster contacts are similar to bottlenecks. These involve hopping between sp² domains, because they give the same potential barrier as in the coating, but limit the electron flux due to the small contact area in between the clusters.

In summary, the hierarchy of the conduction pathways from the nanosize scale (i.e. coherent length of sp² domains) to the macroscopic one is described in

Figure 19.

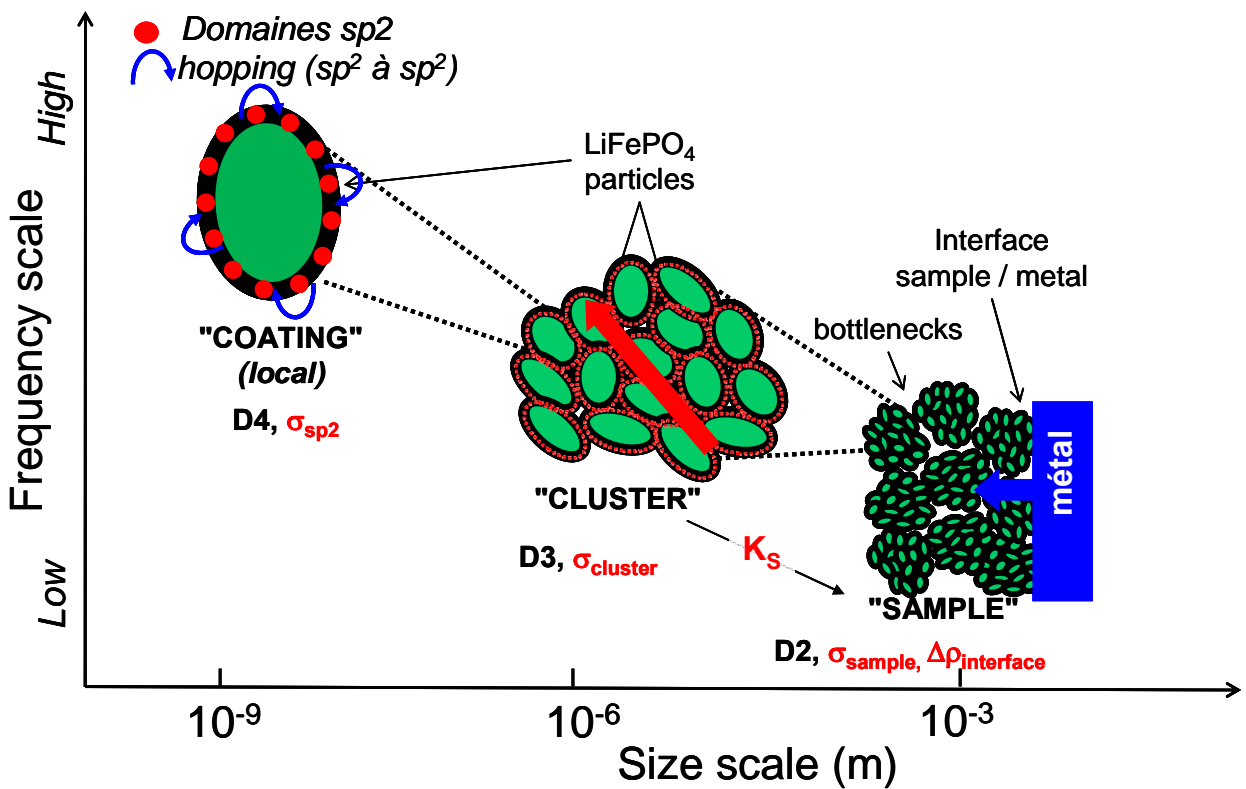


Figure 19. Schematic description of the hierarchical architecture within the samples giving rise to different sources of polarizations.

We can consider that the cluster conductivity is governed by the coating conductivity because the coating constitutes a continuous pathway within the clusters. Their electrical behaviors are thus similar, the cluster conductivity corresponding to an effective value of the coating conductivity, which is mainly dependent of the sp^2 -carbon content. In this way, Figure 20 shows a quasi-linear correlation between the measured (effective) cluster and sp^2 conductivities of the different samples at room temperature (the origin being the sample without coating, i.e. with negligible conductivity).

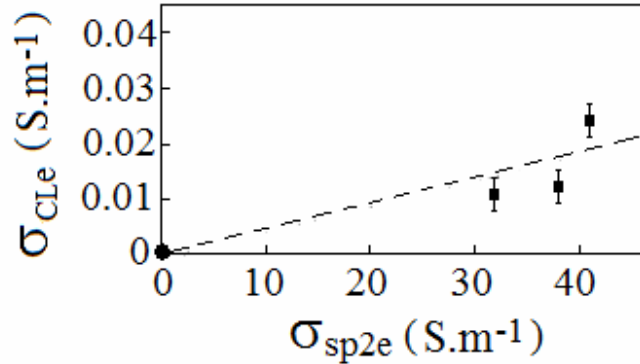


Figure 20. Effective conductivity of the clusters vs. effective conductivity of sp² domains in the different samples.

This correlation is given by

$$\sigma_{CLE} = C\sigma_{sp^2e} \quad (2.7)$$

where σ_{sp^2e} is the sp²-carbon (effective) conductivity and C the slope with a value of about 5×10^{-4} ($\pm 1 \times 10^{-4}$). In the expression (7), the C parameter is surprisingly equal to $\exp(-E_{CL}/kT)$ with $E_{CL} \approx 0.19(\pm 0.01)$ eV, which corresponds to the mean value of the cluster (coating) conductivity activation energy (Table 3). The expression (2.7) can be thus rewritten in the following manner,

$$\sigma_{CLE} = \sigma_{sp^2e} \exp\left(-\frac{E_{CL}}{kT}\right) \quad (2.8)$$

As already mentioned σ_{CLE} and σ_{sp^2e} are effective. Moreover, according to the result depicted in Figure 18, a parameter $K_S < 1$ can be introduced in the equation (2.8) to define the sample conductivity σ_S given by,

$$\sigma_S = K_S \sigma_{CLE} = K_S \sigma_{sp^2e} \exp\left(-\frac{E_{CL}}{kT}\right) \quad (2.9)$$

Since $\sigma_S \ll \sigma_{CLE}$, K_S will take account for the different contacts between the clusters with their constriction resistances and the corresponding conductivity drop from microscopic to

macroscopic scales. [109] In agreement, more favorable value of K_S is found for samples with higher volume fraction of C-LFP (lower porosity), i.e. larger and higher quantity of contacts between the clusters (Figure 21).

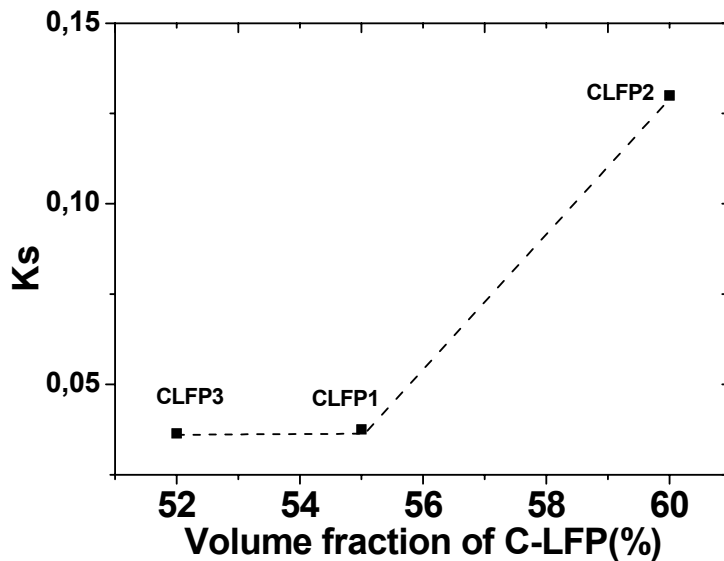


Figure 21. Plot of the parameter K_S (reflecting the constriction+tunneling resistances between clusters) vs. volume fraction of C-LFP.

Finally, the relationship, $\sigma = n\mu_d e$ ($e = 1.6 \times 10^{-19}$ C), between the cluster conductivity σ_{CL} , the drift mobility μ_d and the number n of mobile charge carriers in a cluster is useful to understand the relationship between the activation energies E_{CL} and E_3 . As the drift mobility is proportional to the relaxation frequency, the number of mobile charges is thus thermally activated with activation energy equal to $(E_{CL} - E_3)$.

2.4. Determination of the true conductivities at the different scales of C-LiFePO₄.

In order to extract the coating conductivity from the effective values found from raw experimental results, we will use the brick layer model (BLM), which is well adapted to describe the cluster structure of C-LiFePO₄ samples. The BLM has often been used to explain the electrical properties of electro ceramics and of geological materials (porous rocks,

[109]. D. E. Stephenson, E. M. Hartman, J. N. Harb, and D. R. Wheeler, *J. Electrochem. Soc.*, 154, A1146, (2007).

partially crystallized magma). The classic BLM consists of conducting “cubic bricks” (grain cores) surrounded by resistive “flat mortar” (grain boundaries). In contrary, one cluster of C-LiFePO₄ consists of resistive LiFePO₄ particles surrounded by conducting carbon coating (Figure 22). In this case, the cluster conductivity σ_{CL} is given by [110].

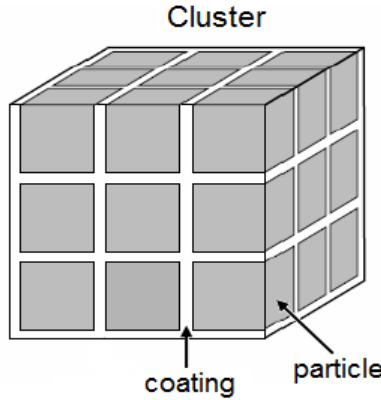


Figure 22. Schematic description of the brick layer model.

$$\sigma_{CL} = \left(1 - (1 - \phi_{cc})^{2/3}\right) \sigma_{CO} \quad (2.10)$$

Where σ_{CO} is the coating conductivity and ϕ_{cc} the carbon-coating volume fraction. As $\phi_{cc} \ll 1$ (Table 2), the expression (2.10) simplifies to:

$$\sigma_{CL} = \frac{2}{3} \phi_{cc} \sigma_{CO} \quad (2.11)$$

As the studied samples are porous (Table 2), it is thus necessary to use a mixture law to express the true value of the cluster conductivity (i.e. σ_{CL}) from the measured one (i.e. σ_{CLe}). General effective medium (GEM) theory describes how to calculate the conductivity of a porous material [111], i.e. consisting of conductive phase and pores. The effective value of the cluster conductivity σ_{CLe} can be compared to that of a hypothetical compact medium σ_{CL} (i.e. true value of the cluster conductivity):

[110]. S.M. ten Grotenhuis, M.R. Drury, C.J. Spiers, and C.J. Peach, J. Geophys. Res. 110 (2005) B12201
[111]. D.S. McLachlan, J. Phys. C: Solid State Phys. 21 (1988) 1521

$$\sigma_{CLe} = \sigma_{CL} \left(\frac{d - d_c}{1 - d_c} \right)^u \quad (2.12)$$

Where d is the volume fraction of the conductive phase (cluster), d_c is the percolation threshold and u is a critical exponent. For 3D systems, ϕ_c is generally between 0.10 and 0.40 and u between 1.65 and 2[110]. Using the expressions (2.11) and (2.12), the true value of the sp^2 conductivity (σ_{sp2}) can be obtained as follow:

$$\sigma_{sp2} = \sigma_{sp2e} \frac{3}{2\phi_{cc}} \left(\frac{1 - d_c}{d - d_c} \right)^u \quad (2.13)$$

where σ_{sp2e} is the effective value of sp^2 reported in Table 2. Considering the mean values $\phi_{cc} = 3.5 \times 10^{-2}$, $d = 0.56$ and $\sigma_{sp2e} = 37 \text{ S.m}^{-1}$, the lower and the upper limits values of the sp^2 conductivity are $\sigma_{sp2} = 5 \times 10^3 \text{ S.m}^{-1}$ and $\sigma_{sp2} = 2.2 \times 10^4 \text{ S.m}^{-1}$ at room temperature, respectively. These results are consistent with experimental values of the graphite conductivity. [112] Using the expression (12) with the same parameters, the lower and the upper limits values of the true cluster conductivity are $\sigma_{CL} = 0.05 \text{ S.m}^{-1}$ and $\sigma_{CL} = 0.23 \text{ S.m}^{-1}$ at room temperature, respectively. In the same way, the expressions (11) and (12) give the lower and the upper limits values of the true coating conductivity σ_{CO} , which are equal to 2 and 10 S.m^{-1} at room temperature, respectively.

In summary, different electrical relaxations (resistivity and permittivity) were shown resulting from the polarizations at their different scales of C-LiFePO₄ samples (Figure 19).

When going from the macro- to the nanoscale, these relaxations can be assigned to: (i) a space-charge polarization at the interface sample – metal (silver); (ii) a polarization of the clusters, which results from the long range motion of charge carriers within the coating; (iii) a polarization due to the local motion of charge carriers in the coating (hopping of electrons from sp^2 to sp^2 via sp^3 carbon regions). The absolute values of the coating σ_{CO} and the clusters σ_{CL} were extrapolated from the measured effective values, and are given for the first time. σ_{CO} and σ_{CL} are reported in Figure 23. The coating conductivity depends on the sp^2 content. The clusters conductivity depends on the coating volume fraction and the coating conductivity. Ultimately, an expression can be given to describe the sample conductivity by combining Eq. (2.9) and (2.13), that is

[112]. X. Wang, L. Zhi, K. Mullen, Nano Lett. 8 (2008) 324.

$$\sigma_s = K_s \left(\frac{d - d_c}{1 - d_c} \right)^u \frac{2\phi_{CC}}{3} \sigma_{sp^2} \exp\left(-\frac{E_{CL}}{kT}\right) \quad (2.14)$$

The expression (14) denotes a relationship between macroscopic (sample) and microscopic (sp^2 domain) levels.

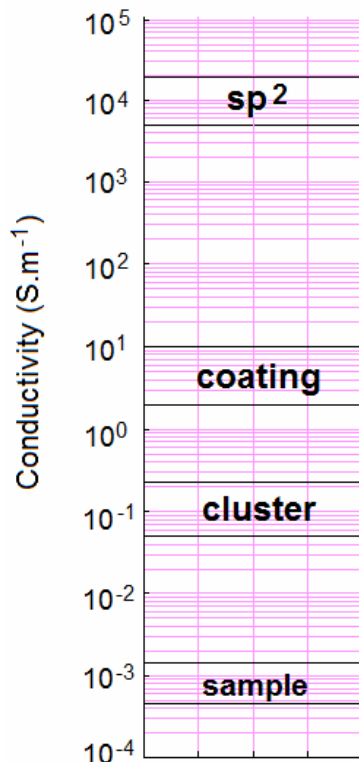


Figure 23. Different conductivity levels in a hierarchical compound such as C-LiFePO₄

2.5. Calculation of the bulk permittivity of LiFePO₄.

General effective medium theory can also determine the permittivity of a porous sample[110]. As the volume content of carbon coating is negligible, its permittivity has no influence on the sample permittivity. The effective value of LiFePO₄ permittivity ϵ_∞ can be compared to that of a hypothetical compact medium ϵ_{LFP} :

$$\frac{(1-d)(1-\epsilon_\infty^{1/u})}{d_c + (1-d_c)\epsilon_\infty^{1/u}} + \frac{d(\epsilon_{LFP}^{1/u} - \epsilon_\infty^{1/u})}{d_c\epsilon_{LFP}^{1/u} + (1-d_c)\epsilon_\infty^{1/u}} = 0 \quad (2.15)$$

Considering the mean values $d = 0.56$ and $\epsilon_\infty = 3.55$, the lower and the upper limits values of the LiFePO₄ permittivity are $\epsilon_{LFP} = 6.8$ and $\epsilon_{LFP} = 8.8$, respectively. These values are lower than the calculated value ($\epsilon_s = 11.58$) by the shell model. Our experimental and calculated values by GEM theory agree with measured values for other inorganic phosphates (in the range 4.6 – 10.7) reported by Shannon [113] and Islam et al. [114]

3. Conclusions

The broadband dielectric spectroscopy (BDS) has been used for a more detailed characterization of the electrical properties of composite materials for lithium batteries. The BDS frequency range is extended from low-frequencies (few Hz) up to microwaves (few GHz). The results obtained in this work demonstrate that the BDS can distinguish the different types of electronic transfers involved in the different scales of the material architecture. These phenomena occur from interatomic to macroscopic sizes with the influence of the morphology of the different constituents at these scales. In summary, considering a composite material composed of an active material (e.g. LiFePO₄) and a conductive agent (e.g. carbon coating), when the frequency increases, different kinds of polarizations, giving rise to dielectric relaxations, appear in following order: a) Space-charge polarization (low-frequency range) due to the interface between the sample and the conductive metallic layer deposited on it; b) Polarization of C-LiFePO₄ clusters (micronic and/or submicronic scales) due to the existence of resistive junctions between them; c) Electron hopping between sp² domains (nanometric scale) within the carbon coating around the LiFePO₄ particles. The conductivity and permittivity of the composites measured are effective parameters since they are functions of the relative concentration of the different phases. Using the Brick Layer Model and the General Effective Medium theory, it was possible to give some orders of magnitude for the true values of the conductivity at the different scales of the material, i.e. macroscopic, cluster, and coating and sp² domains levels. We have thus established an empirical expression to describe the sample conductivity with respect to that of the smaller level (coherence length of sp² domains). Moreover, the true permittivity value of LiFePO₄ has been, for the first time, obtained from permittivity

[113]. R.S. Shannon, J. Appl. Phys. 73 (1993) 348.

[114]. M.S. Islam, D.J. Driscoll, C.A.J. Fisher, and P.R. Slater, Chem. Mater., 17 (2005) 5085.

measurements and the use of the GEM theory. The results are in good agreements with the permittivity values of the different phosphates.

Chapter 3: Ternary systems

1. Introduction

With the context of going step by step, once we have studied the binary systems (Carbon-LiFePO₄) in chapter two, we continued to study ternary systems (Carbon-LiFePO₄/binder). It has to be remembered that in Chapter 2, we used the broad band dielectric spectroscopy technique (BDS) to study the electrical properties at the different scales of C-LiFePO₄ samples with primary particles varying in size (50-150nm) and carbon content (0-4wt%), aggregated into micron-size clusters (<2μm), and compacted in the form of powder pellets. By varying the frequency from low frequencies (40 Hz) to the microwaves (10 GHz), the BDS has evidenced four dispersion domains (three of which being relaxations) associated with the different scales of the samples. Below few MHz, two dispersion domains at the sample/current collector scales were identified: a) D1 corresponding to the dc conduction and related to the random distribution of the contact points between the sample and the current collector; b) D2 due to space charge relaxation at the electrode current collector interface (Schottky barrier). Above few MHz, two relaxations at the micro/nano scales were evidenced: a) D3 due to the long range hopping of charge carriers in the carbon coating (cluster polarization); b) D4 related to the local charge transfer between sp² domains. Subsequently, from low to high frequency, three intrinsic conductivity levels have also been identified corresponding to the sample (σ_s), the clusters (σ_{CLE}) and sp²-coordinated carbon domains (σ_{sp2e}). Furthermore the sample/current collector interface ($\Delta\rho_1$) and inter-cluster ($\Delta\rho_2$) values corresponding to junction resistivities were determined. The temperature dependence of the relaxation/conductivity levels was exploited to understand the nature of the charge carriers and thus the conductivity mechanisms. The true conductivities at the different levels have also been calculated using a mixing law (i.e. General Effective Medium theory) and the Brick Layer model. To sum it up, we have established a relationship between the nano/sub-nano (sp² and coating), the micro (clusters) and the macro (sample) scales. The true mean permittivity of LiFePO₄ was also determined from experimental data and found to be in good agreement with calculated values. We will exploit thereafter the know-how developed to study ternary Carbon-LiFePO₄/carboxymethyl Cellulose systems. The evolution of the different relaxation domains and conductivity levels with the introduction of a binder will be investigated. For the purpose, several equations and relationships, which have already been used on binary systems (Chapter 2), are summarized in Table 1.

Table 1. The main equations used to characterize the different electrical relaxations at the different scales, their hierarchical relationships, and used to calculate the true conductivities from the measured (effective) data.

See next page

Equation	Identification of the parameters
The complex Cole-Cole function used to describe the dielectric relaxations [22] $\epsilon(\omega) = \epsilon_H + \frac{\epsilon_L - \epsilon_H}{1 + (i\omega\tau_\epsilon)^{1-\beta}} \quad (3.1)$	ϵ_L and ϵ_H : low- and high-frequency limits of the permittivity. τ_ϵ : Mean relaxation time (relaxation frequency, $v_\epsilon = (2\pi\tau_\epsilon)^{-1}$). $\Delta\epsilon = (\epsilon_L - \epsilon_H)$: strength of the relaxation. β : ($0 \leq \beta \leq 1$), determines the degree of deviation from the ideal Debye ($\beta = 0$).
The complex Cole-Cole function used to describe the resistivity relaxations [22] $\rho(\omega) = \rho_H + \frac{\rho_L - \rho_H}{1 + (i\omega\tau_\rho)^{1-\beta}} \quad (3.2)$	ρ_L and ρ_H : low- and high-frequency limits of the resistivity. τ_ρ : Mean relaxation time (relaxation frequency, $v_\rho = (2\pi\tau_\rho)^{-1}$). $\Delta\rho = (\rho_L - \rho_H)$: strength of the relaxation. β : defined above
Describes the relaxation frequency of the electrons hopping between localized sites (sp^2 domains) into the carbon coating. [102] $v = v_0 \exp\left(-\frac{E}{kT}\right) \quad (3.3a)$ $v_0 = v_{ph} \exp(-2\alpha R) \quad (3.3b)$	v_{ph} : phonon frequency (4.2×10^{13} Hz in graphite) [115] v_0 : frequency prefactor R: Mean hopping distance, E: energy difference between the localized sites. α^1 : localization length ($\alpha^1 \ll r$) characterizing the spatial extension of the electronic wave function (1.2 nm in amorphous carbon). [116] k and T have their usual meanings
Empirical (Arrhenius) equation relating the effective clusters and effective sp^2 domains conductivities. $\sigma_{CLe} = \sigma_{sp2e} \exp\left(-\frac{E_{CL}}{kT}\right) \quad (3.4)$	σ_{CLe} : effective conductivity of cluster σ_{sp2e} : effective conductivity of sp^2 domains. E_{CL} : activation energy for long-range hopping in the cluster.
Empirical equation relating the effective cluster and sample conductivities $\sigma_s = K_s \sigma_{CLe} \quad (3.5)$	σ_s : the sample conductivity K_s : parameter introduced to account for inter-cluster constriction and tunneling resistances. $K_s = f(w_{gap}, \epsilon_{binder}, T, N_{contact}, R_{tunnelling}, \dots)$
Simplified ($\phi_{cc} \ll 1$) brick layer equation relating the true coating and cluster conductivities. [110] $\sigma_{CL} = \frac{2}{3} \phi_{cc} \sigma_{CO} \quad (3.6)$	σ_{CO} : true coating conductivity σ_{CL} : true cluster conductivity. ϕ_{cc} : the coating volume fraction in the cluster.
A general effective media theory (GEM) equation used to calculate the true cluster conductivity. [104] $\sigma_{CL} = \sigma_{CLe} \left(\frac{1-d_c}{d-d_c} \right)^u \quad (3.7)$	d: volume fraction of the conductive phase (clusters). 1-d is the insulator volume fraction d_c : percolation threshold ($0.10 < d_c < 0.40$ in 3D systems) u: critical exponent ($1.65 < u < 2$ in 3D Systems).
Equation obtained by combining (3.6) and (3.7) used to calculate the true sp^2 conductivity. $\sigma_{sp2} = \sigma_{sp2e} \frac{3}{2\phi_{cc}} \left(\frac{1-d_c}{d-d_c} \right)^u \quad (3.8)$	σ_{sp2} : true sp^2 domains conductivity.
A general expression depicting the relationship between macro (sample) and sub-nano (sp^2 domains) conductivities. $\sigma_s = K_s \left(\frac{d-d_c}{1-d_c} \right)^u \frac{2\phi_{CC}}{3} \sigma_{sp2} \exp\left(-\frac{E_{CL}}{kT}\right) \quad (3.9)$	(All parameters defined above)

2. Results and discussion

[115] J. Maultzsch, S. Reich, C. Thomsen, H. Requardt, and P. Ordejon, Phys. Rev. Lett., 92 (2004) 75501
[116] J. Robertson, Adv. Phys., 35 (1986), 317

2.1. Sample preparation and analysis of their morphology

Materials: A new batch of pristine active material used, C-LiFePO₄ with 4 wt % Carbon coating and primary particle size of 150nm, was supplied by UMICORE Cobalt & Specialty Materials, Belgium. carboxymethyl cellulose [CMC, 0.7 carboxyl unit per molecule of cellulose (DS=0.7), Mw=90,000g/mol, Aldrich] was used as a binder (Figure 1). Deionised water was used as a solvent.

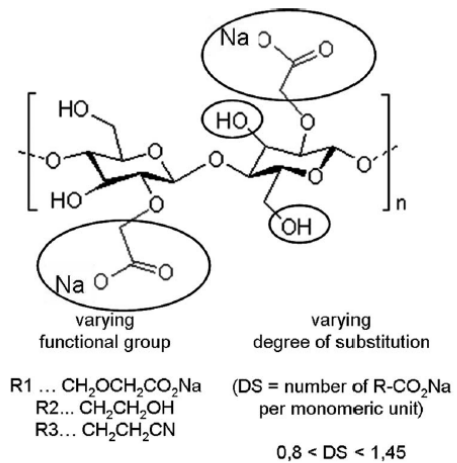


Figure 1. Structure of carboxymethyl cellulose molecule (CMC) [117]

Samples: The materials were mixed in the solvent (deionised water) with a solid loading of ~28%wt (C-LiFePO₄+CMC) using a planetary ball mill (with three ZrO₂ balls) operating at 700rpm for 1 hour. This step ensures homogenous distribution of the components. This slurry is then casted onto an appropriate support (aluminium foil) and dried. The resulting film is then scrapped from its support and the sample is recovered in powdery form. Appropriate size cylindrical disc pellets are prepared for BDS measurements by compaction at 510 MPa using a pelletizer (Ets Canaple). Metallic contacts are made by applying and drying conductive Ag paint (Oxford Instruments) directly on both front faces of the pellet. Pellets of several compositions were prepared for the purpose.

Characterizations and Morphological studies: **Table 2** below gives the samples' composition and their parameters. HRTEM was performed following the same procedure described in the earlier chapter. TEM images before (Figure 1) and after ball milling (Figure 2) in two different solvents, N-Methyl-2-pyrrolidone (NMP) and Water, were taken to check the

[117]. W.R. Liu, M.H. Yang, H.C. Wu, S.M. Chiao, N.L. Wu, Electrochim. Solid-State Lett. 8 (2005) A100

evolution of the carbon coating if there is any upon ball milling in water and NMP. They suggested a slight reduction/compaction in thickness upon ball-milling.

Table 2. The samples' composition, thickness, porosity. The volume fraction of C-LiFePO₄ was calculated from the considerations of its volume (from its density and mass) and the actual volume of the electrode (from the thickness and surface area): $\phi_{v,LFP} = ((\phi_{w,C-LFP} \times m_{pellet}) / \rho_{C-LFP}) / (t \times s)$, with t pellet thickness, s surface areas of pellet. The theoretical thickness w of binder covering the C-LFP particles, on the other hand, was calculated from the volume of the binder (1-porosity- $\phi_{v,C-LFP}$), and then assuming a homogeneous distribution of the binder

$$w = \left(\left((\phi_{v,CMC} \times r^3) / \phi_{v,LFP} \right)^{1/3} - r \right)$$

around spherical C-LiFePO₄ particles, with r radius of the primary particles.

Sample	%v CMC (Φ_v,CMC)	Mass of the pellet (mg)	Thickness of the pellet (μm)	Porosity (%)	%v C-LiFePO ₄ (Φ_v,LFP)	Theoretical thickness of CMC covering C- LFP particles w (nm)
150C4	0	60	875	51	49	----
C0	0	32	452	47	53	0
C5	6	41	583	44	50	2.9
C7	9	61	858	42	49	4.4
C10	12	67	927	40	48	5.85
C15	17	56	795	38	45	8.5

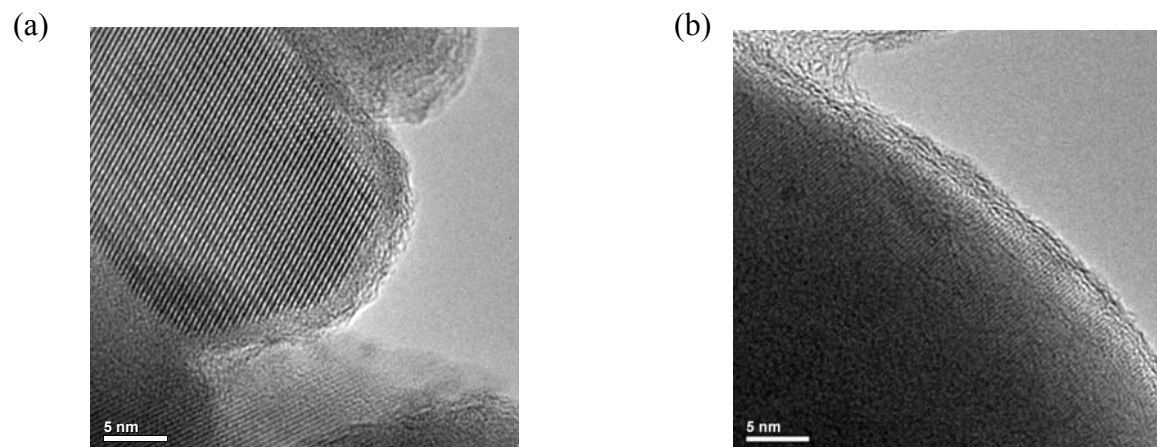


Figure 24. HRTEM images of the powders (a,b) before ball milling

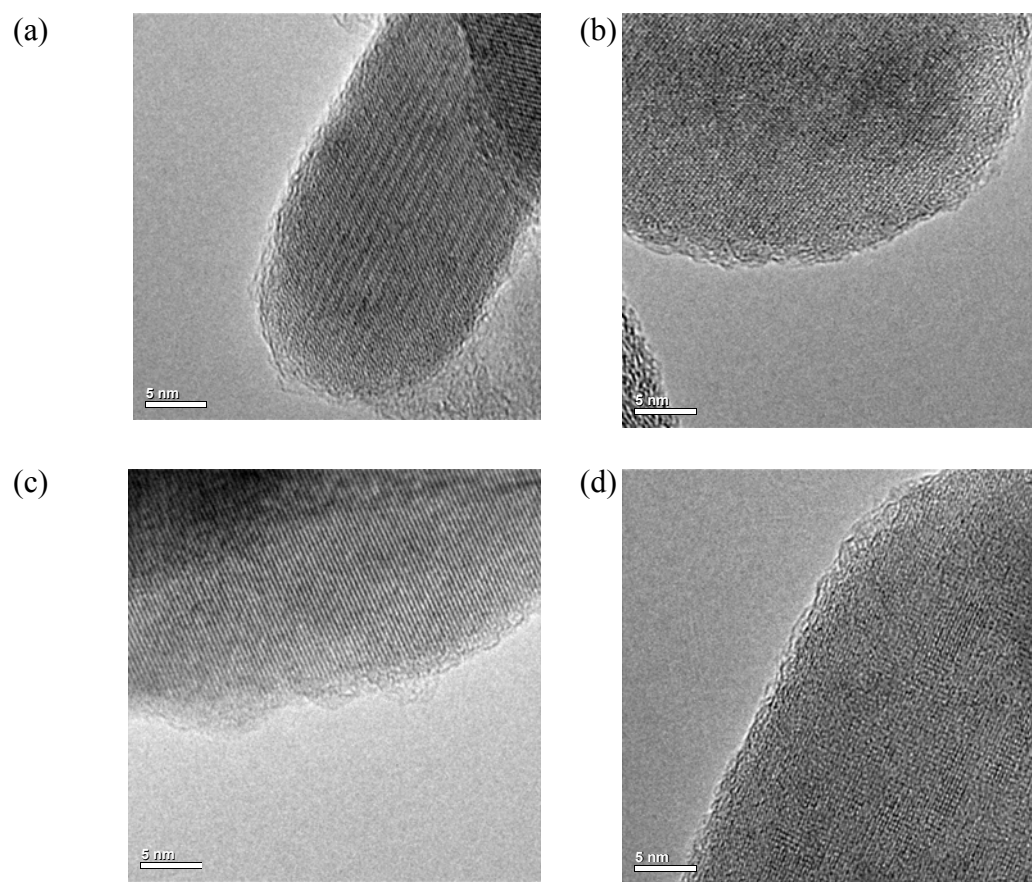


Figure 2. HRTEM images of the powders (a,b) after ball milling in water; (c,d) after ball milling in NMP

Similarly HRSEM measurements were carried out following the procedure described in the chapter 2. The representative HRSEM images are shown for C3 and C15 in Figure 3. These pictures show that even at high magnification, a distinct polymer phase from the C-LFP

particles is hardly detectable in C3 (Figure 3a-b). CMC is thus not segregated and rather homogeneously coat the C-LFP clusters. In C15, the CMC is visible for the naked and accustomed eye and looks fairly homogeneously distributed as a layer at the surface of the particles. This will fill, to some extent, the porosity and/or increase the interparticle contact surface area (Figure 3c-f).

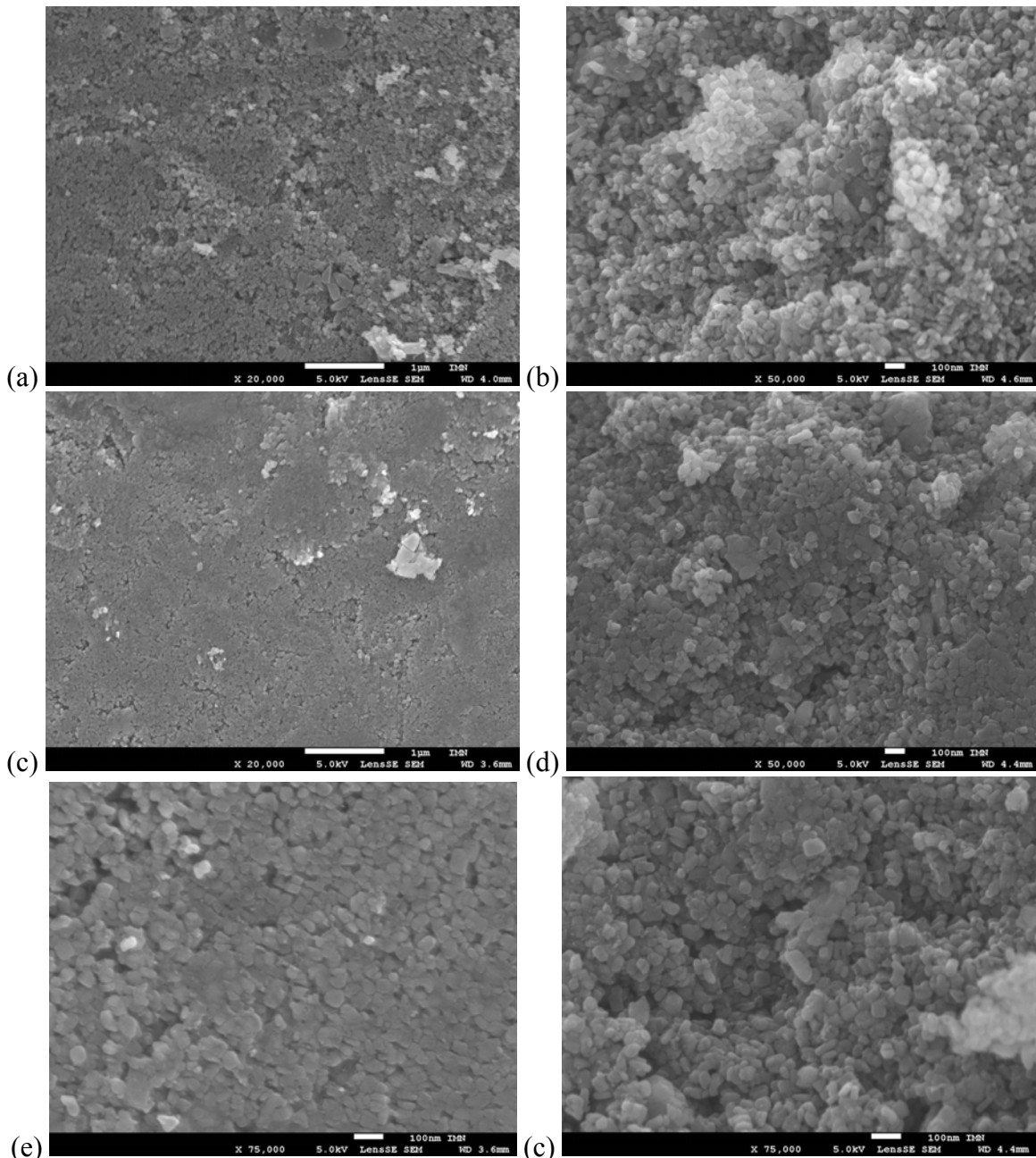


Figure 3. The SEM images of the pellets for C3 and C15 samples. (a) C3 surface x 20,000. (b) C3 cross-section x 50,000. (c) C15 surface x 20,000. (d) C15 cross-section x 50,000. (e) C15 surface x 75,000. (f) C15 cross-section x 75,000.

2.2. Electrical measurements.

Complex resistivity and permittivity spectra were recorded over a broad frequency range 40 to 10^{10} Hz. The frequency dependent conductivity (real part) of the samples at room temperature is shown in Figure 4. A slight discrepancy for the CMC10 can be noted from the distinctly higher permittivity above the MHz. It could be due to experimental imperfections like a slight adsorption of water during the sample transfer.

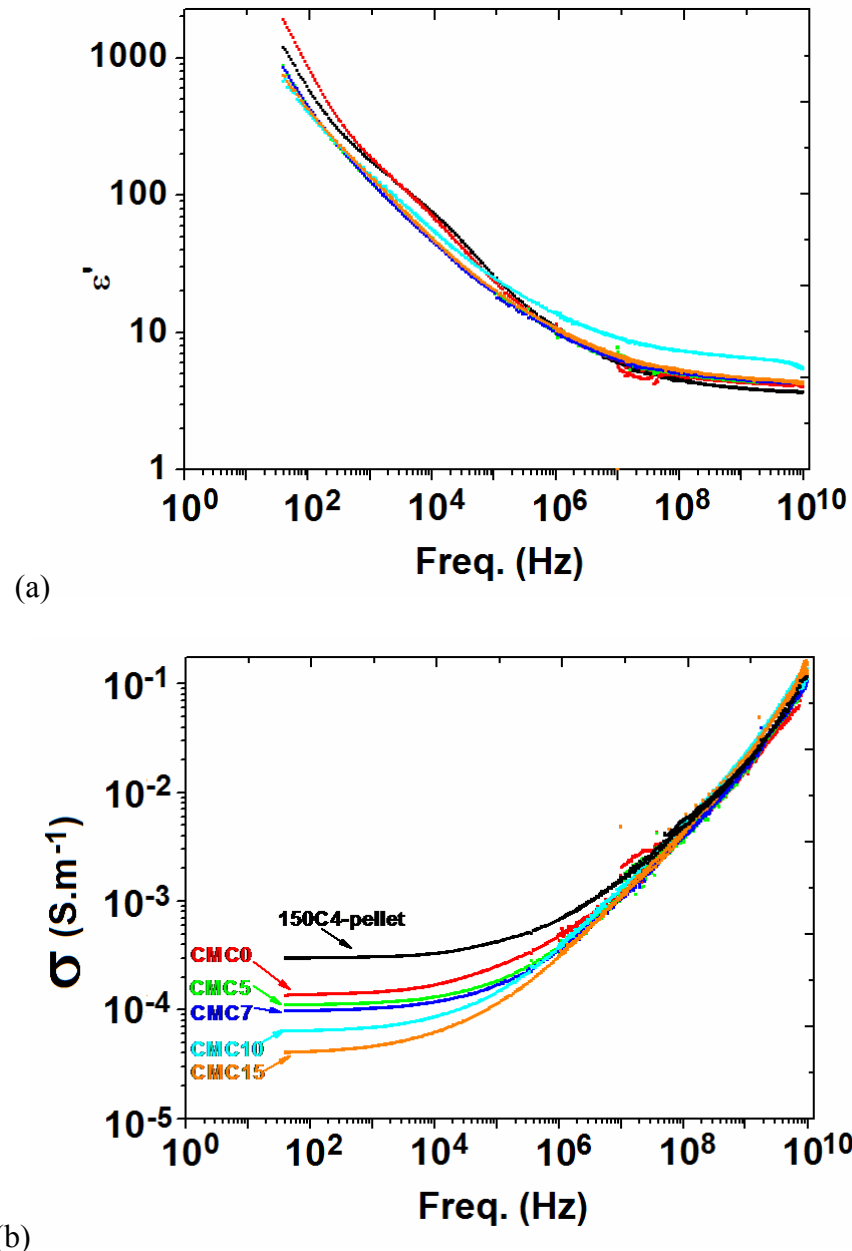


Figure 4. The frequency dependence of real part of conductivity (σ') and (b) the frequency dependence of real part of the permittivity (ϵ') for all the samples at RT.

As the possible dielectric relaxations are not clearly seen in frequency-dependent representation, it is more suitable to use the Nyquist plots that offer an easier decomposition of the dielectric spectra. Since all the polarizations at different scales are additive owing to their vector character, their contributions (relaxations) can thus be evidenced by a decomposition procedure of the permittivity Nyquist plots (i.e. ϵ'' vs. ϵ') (Figure 5) in a similar manner as already seen in previous chapter. The same data can also be represented in resistivity Nyquist plots (i.e. ρ'' vs ρ'), which are shown in Figure 6. The relevant parameters extracted from the complex permittivity and conductivity plots using Cole-Cole function (eq. 3.1 and 3.2 in Table 1) are presented in Figure 7 (example of CMC5 conductivity Arrhenius plot) and **Table 3**.

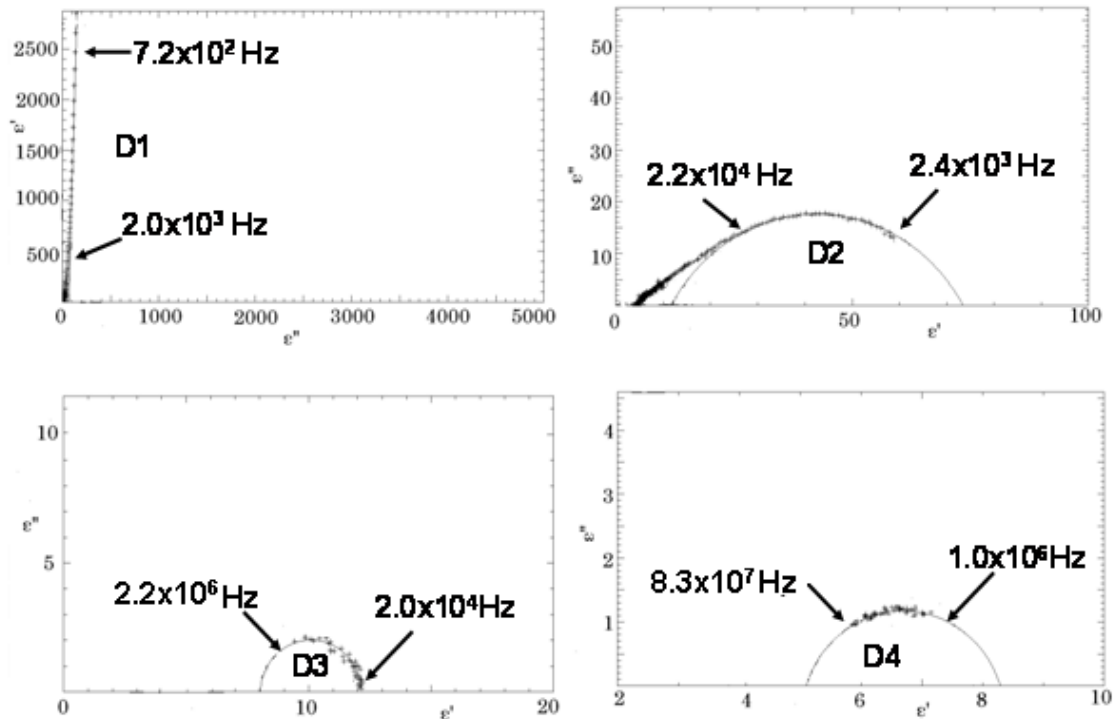


Figure 5. Decomposition of permittivity Nyquist plots (i.e. ϵ'' vs. ϵ') for CMC5 at room temperature

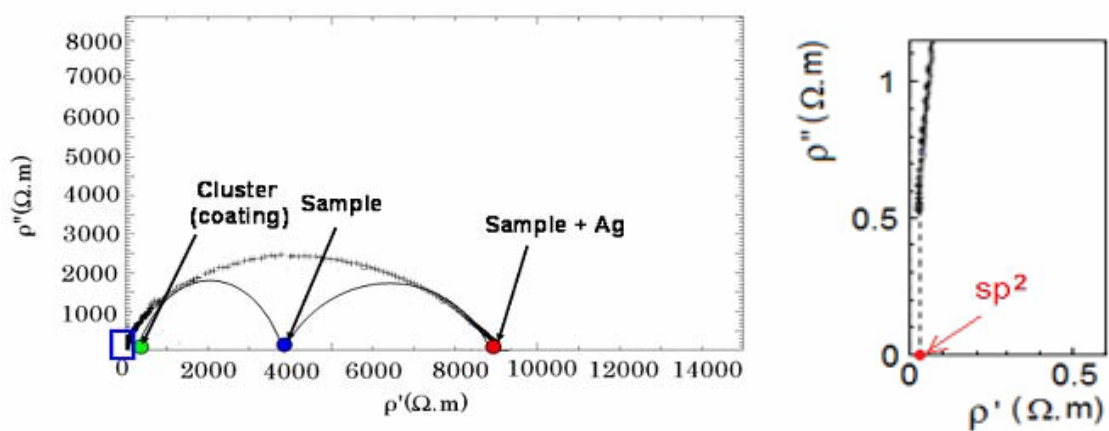


Figure 6. Decomposition of resistivity Nyquist plots (i.e. ρ'' vs. ρ') for CMC5 at room temperature

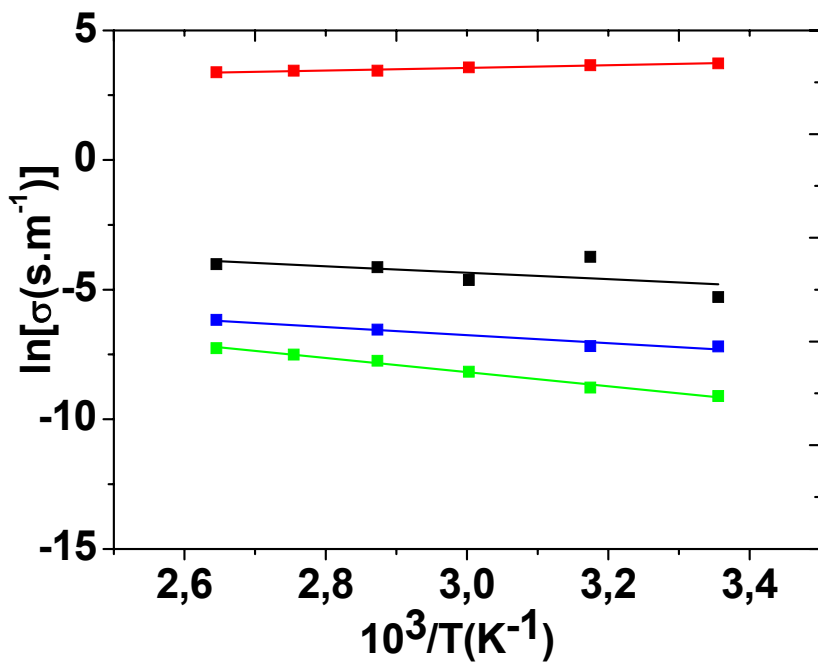


Figure 7. Effective conductivities as function of inverse temperature for CMC5: sample / interface Ag (green); sample (blue); cluster (black) and sp^2 domain (red).

Table 3. Conductivity σ_i , sample/current collector ($\Delta\rho_{1,2}$) and clusters' junction ($\Delta\rho_{2,3}$) resistivities, activation energy E_i , dielectric relaxation frequency v_i at room temperature, frequency prefactor v_{0i} , dielectric strength $\Delta\epsilon_i$ and α_i parameter associated with the polarization sources within the different samples: hopping between the sp^2 -carbon domains (D4), cluster (D3) and interfacial (D2) polarizations.

	Interfacial polarization D2	Clusters polarization D3	sp^2 domains (hopping) D4	Conductivity($S.m^{-1}$)						ϵ_∞
Sample	v_2 (Hz)	v_3 (Hz)	v_4 (Hz)	Sample σ_s E_s (eV)	Cluster	$^{a)} \sigma_{CLe}$	$^{a)} \sigma_{sp2e}$	$\Delta\rho_1$ ($\Omega.m$)	$\Delta\rho_2$ ($\Omega.m$)	
	v_{02} (Hz)	v_{03} (Hz)	v_{04} (Hz)		E_{CL} (eV)					
150C4	2×10^4	5×10^5	1.2×10^7	1.1×10^{-3} 0.19	1.0×10^{-2}	40	2500	1000	3.7	
	4.7×10^7	7.8×10^7	8.4×10^7		0.18					
	0.20	0.13	0.05	0.19	0.18					
	65	8.2	2.8							
CMC0	1.1×10^4	2.5×10^5	8.5×10^6	9.1×10^{-4} 0.14	5.2×10^{-3}	41	6275	950	4.0	
	5.6×10^6	1.3×10^8	2.7×10^8		0.13					
	0.16	0.16	0.08	0.14	0.13					
	87	9.2	2.6							
CMC5	9.5×10^3	3.4×10^5	8.2×10^6	7.5×10^{-4} 0.16	5.1×10^{-3}	41	7710	1250	4.2	
	1.5×10^7	2.5×10^8	8.7×10^8		0.14					
	0.19	0.17	0.12	0.16	0.14					
	61	4.1	3.2							
CMC7	8×10^3	2.3×10^5	4.8×10^6	4.6×10^{-4} 0.19	3.6×10^{-3}	38	8180	3110	4.3	
	1.9×10^7	3.7×10^8	1.6×10^9		0.18					
	0.20	0.19	0.15	0.19	0.18					
	50	10.2	3.6							
CMC10	5×10^3	2.6×10^5	6.6×10^6	4.1×10^{-4} 0.21	3.6×10^{-3}	$55-71$	13530	4100	5.4	
	1.8×10^7	6.2×10^8	3.5×10^9		0.19					
	0.21	0.20	0.13	0.21	0.19					
	93	14	2.3							
CMC15	4.5×10^3	3×10^5	8.4×10^6	1.8×10^{-4} 0.25	1.7×10^{-3}	37	19860	11380	4.2	
	4.0×10^7	2.3×10^9	1.9×10^9		0.23					
	0.23	0.23	0.14	0.25	0.23					
	86	5	3.3							
	0.38	0.16	0.25							

2.3. Analysis of the effect of ball-milling in water

First, let's assess the effect of ball milling and compare the samples prepared from the pristine powder (150C4) with the one prepared from the powder ball milled in water and dried (C0). Table 4. sp^2 percent (%) determined from XPS measurements for the pristine 150C4 powder sample (CLFP3 batch n°2) and C0 (the same 150C4 sample but ball milled in water at 500rpm for 1 hr).

Sample	sp^2 percent in the coating (%)
150C4	60
C0	49

The $\% \text{sp}^2$ is significantly reduced in the CMC0 sample compared to 150C4, most likely due to the amorphization of the coating and an increase in impurity content due to environmental oxidation. Both can be induced by the high energy ball milling in water. The decrease in $\% \text{sp}^2$ is in agreement with the increase in activation energies E_3 and E_4 for C0 compared to 150C4 (See Table 3 and Figure 16 in chapter 1).

Let's note that the 150C4 sample is from a new batch, which explains why the results reported in Table 3 for this sample are different from chapter 2. As we have shown above (Figure 4), a drop in conductivity, specifically at low frequency, is observed from 150C4 to C0. This drop in conductivity occurs mostly in the low frequency range, i.e. at the sample/current collector interface. $\Delta\rho_1$, which characterizes the sample/silver paint contact resistance, is more than 2 times higher for C0 compared to 150C4 (Table 3). This corresponding contact resistance depends on various parameters (e.g. roughness of the pellet surface, the hand-deposited metallization), thus it is difficult to provide a relevant explanation at this scale.

On the other hand an increase in activation energy of the same magnitude (i.e. $0.03\text{eV} \sim kT$) is observed for D3 and D4 (Table 3), which corresponds typically to the interaction of a mobile dipole with a charge carrier. [118] This might indicate a possible contamination of the sample by a small quantity of water molecules during ball milling in water. The small increase in ϵ_∞ from 3.7 (150C4) to 4.0 (C0) is also in agreement with this hypothesis.

[118]. L. Beluze, J. C. Badot, R. Weil, and V. Lucas, *J. Phys. Chem. B*, 110 (2006) 7304

2.4. Analysis of the effect of the binder on the bulk properties (ε_∞ and σ_{sp2e})

In the following section, we will discuss the results of the BDS related to the ball milled binary samples (C0-C15). We will follow a logical order in which we will start from the nanoscale and continue to the macro scale in hierachal manner. Figure 8 shows the evolution of ε_∞ and σ_{sp2e} as a function of the binder loading at room temperature. Globally, one can see that both parameters are unaffected by the addition of the binder, as expected. There is a small decrease in σ_{sp2e} , likely due to the decrease in the volume fraction of the carbon (Eq. 3.8, Table 1). Another trend is a small increase in permittivity with the exception of 150C4, which could be due to the increase in quantity (in the range of 4-20v%) of the non LFP component (carbon coating + binder). This is significant and will most probably affect ε_∞ in contrast to the binary systems in which the volume fraction of carbon is adjudged to be too small to affect ε_∞ . Note that ε_∞ of CMC is in the range 2 to 6. [119,120,121]

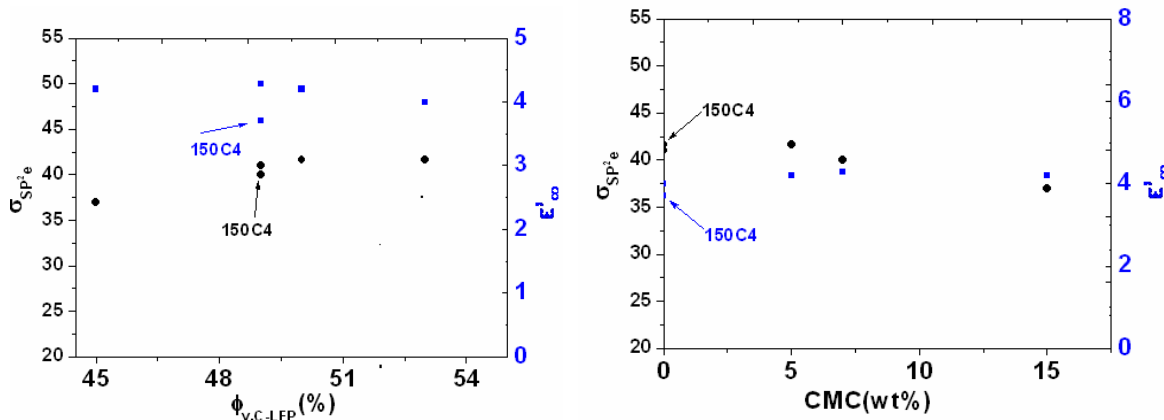


Figure 8. The evolution ε_∞ and σ_{sp2e} as a function of CMC loading at room temperature.

2.5. Analysis of the effect of the binder on the coating properties and cluster conductivity

Figures 9a and b present the relaxation frequencies of the dielectric relaxations D3 and D4 (at room temperature), which correspond to the long range (cluster polarization) and local hopping of electrons in the coating respectively.

-
- [119]. E. El Shafee, Carbohydrate Polymers, 31 (1996) 93
 - [120]. Refaat I. Nessim, Maged G. Botros, Gamal R. Saad, Mohamed M. Shalaby, Die Angewandte Makromolekulare Chemie, 204 (1993) 51
 - [121]. S.A. El-Henawii, S.M. Saad, I.M. El-Anwar., J. Mater. Sci. Technol., 15 (1999) 164

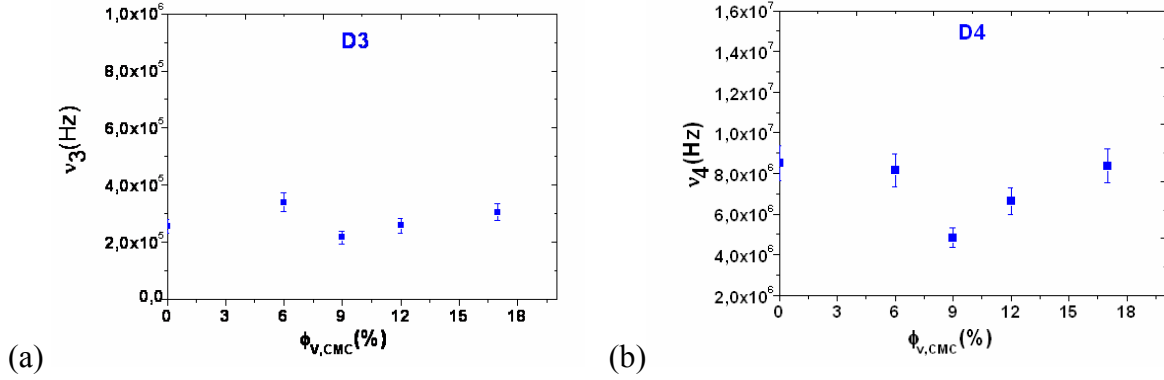


Figure 9. The evolution of the relaxation frequency for the (a) relaxation domain D3 and (b) for the relaxation domain D4 in both cases at RT

At first sight, it looks like there is no significant evolution of the relaxation frequencies with the binder loading. The dependence in the binder additives does not seem expected for these phenomena (D3 and D4). Nevertheless, for better understanding of these dielectric relaxations we must scrutinize the variations of the fundamental parameters: prefactors (v_{03} and v_{04}) and activation energies (E_3 and E_4) of v_3 and v_4 (see Eq. 3.3 in Table 1). The evolution of the activation energies of D3 and D4 with the binder loading is presented in Figure 10. The results show that the activation energy for the relaxations tends to increase with an increase in binder loading for: a) long-range or inter-particle (within the clusters) hopping (D3) and b) local hopping between sp^2 domains (D4). The evolution for D4, on the other hand, is different compared to D3. There is a plateau after a CMC volume fraction of about 9%.

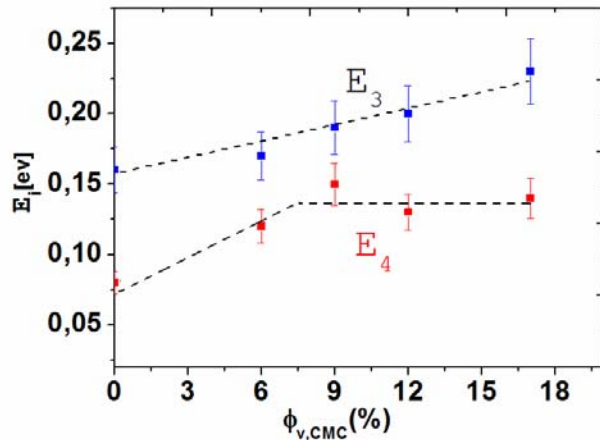


Figure 10. Evolution of the activation energy for the relaxation domains D3 and D4 with the binder loading (volume fraction).

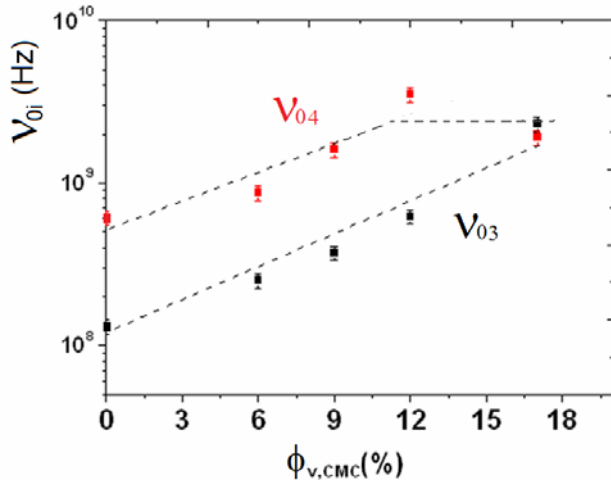


Figure 11. The evolution of the pre exponential factors $v_{0,3}$ and $v_{0,4}$ with the binder loading (volume fraction).

Furthermore, the evolution of the frequency prefactors $v_{0,3}$ and $v_{0,4}$ with the CMC content is shown in Figure 11. The prefactor v_{03} of about one order of magnitude as the binder volume fraction increase from 0 to 17%.

An induced electrostatic interaction between CMC and the carbon coating could explain the variations in the properties of the D3 and D4 which are however considered to be intrinsic properties of the coating.

Indeed, an electronic interaction between CMC and different graphitic substrates has been reported in several works. CMC has been shown to favourably interact with graphitic surface and spontaneously adsorb. [122,123,124] Riou et al. reported a non covalent binding between semi-conducting (rather than metallic) single walled carbon nanotube (SWNT) and CMC and hypothesized some hydrophobic or Van der Waals interaction between the glucose ring of the CMC macromolecule and the hydrophobic graphitic surface of carbon nanotube, i.e. sp^2 -coordinated carbons. [125] There are also reports on the existence of an interaction between CMC and highly oriented pyrolytic graphite (HOPG) in such a way that the hydrophobic axial plane of the glucose ring of CMC can strongly interact with the sp^2 hybridized orbital of the aromatic rings through CH- π bonding. [126,127,128] Other interaction mechanism mainly based on hydrogen bonding or chemical complexation between

-
- [122]. Lee, J.-H. Paik, U. Hackley V.A.; Choi, Y.-M. J. Electrochem. Soc., 2005, 152, A1763.
 - [123]. Lee, J.-H.; Paik, U.; Hackley V.A.; Choi, Y.-M. J. Power Sources, 2006, 161, 612.
 - [124]. Pawlik, M. Coll. Surf. A, 2005, 266, 82.
 - [125]. I. Riou, P.Bertoncini, H. Bizot, J.Y Mevellec, A. Buléon, O.Chauvet, J Nanosci. Nanotechnol. 9 (2009). 6176.
 - [126]. S. Yokota, T. Ueno, T. Kitaoka, D. Tatsumi, and H. Wariishi , Biomacromolecules, 8 (2007) 3848.
 - [127]. T. Ueno, S. Yokota, T. Kitaoka and H. Wariishi, Carbohydrate Research, 342 (2007) 954.
 - [128]. T. Ueno, S. Yokota, T. Kitaoka and H. Wariishi, Carbohydrate Research, 342 (2007) 2593.

the –OH groups at the equatorial sides of the glucose ring and the oxygen-containing groups at the surface of graphite are also suggested. [129,130] In our case, the interaction of the CMC with the amorphous carbon coating should not be surprising. As the result, the electrical properties related to the carbon coating at the nanoscale could possibly be altered by interaction with CMC, electrons being trapped at the surface by functional groups of the adsorbed CMC.

Coming back to our results, the increase in v_{0i} would reflect an increase in the number of trapping centers and the corresponding increase in surface electron density. The trapping sites are formed due to the adsorbed CMC on the carbon coating and their electrostatic interactions. As the CMC content increases, the localization centers (trapping centers) are closer to each other, resulting in a better overlap of the electronic wave functions on the two sites making hopping distances shorter. However, this interaction between CMC and the carbon coating also raises the activation energy for relaxation between two sp^2 sites which has an opposite effect. At room temperature, hopping frequencies appear unaffected by the binder loading.

The hopping distance R, which is inversely proportional to the supplementary number of trapping centers (CMC bonds on carbon coating surface), is determined with Eq. 3.3 (Table 1), considering a constant α (which is about 1.2 nm in amorphous carbon [116]), $v_{ph} \sim 4.3 \times 10^{13} \text{ Hz}$,[115] and from the values of $v_{0,3}$ and $E_{0,3}$. R, is shown as a function of the binder loading in Figure 12. It can be observed that R linearly decreases with volume fraction of CMC ($\Phi_{V,cmc}$). Indeed, when $\Phi_{V, cmc}$ increases, an increase in trapping centers can be reasonably expected, i.e. the hopping distances decreases. As a matter of fact, unpublished results at IMN demonstrate that CMC with Mw 90,000g/mol can adsorb at least up to 4mg/m² on carbon black without reaching the saturation of the graphitic surface. Here, the BET surface of 150C4 is found to lie in between 36 and 55m²/g. For example, if we consider the sample C15, and the situation where all the CMC would adsorb to the surface of the C-LFP particles, that would correspond to adsorption values in between 3.2 and 4.9mg/m². Thus, for all the samples studied here, the CMC concentration is such that it would be below the amount to reach the saturation of the C-LFP surface. Consequently, with increasing the CMC concentration, from C0 to C15, the amount of adsorbed CMC can be expected to increase

[129]. Q. Liu, Y. Zhang, J.S. Laskowski, Int. J. Miner. Process. 60 (2000) 229.

[130]. S. Subrammiant and J. S. Laskowski, Langmuir, 9 (1993) 1330.

linearly with the concentration. [131,132] Thus the linear decrease in R with the CMC content is relevant.

In conclusion, our results strongly suggest a linear relationship between the amount of adsorbed CMC at the surface of the C-LFP particles and the supplementary number of trapping centers for electrons in the carbon coating, as well as an increase in the barrier energy opposing hopping of charges. Complementary investigations must be undertaken to assess this original result.

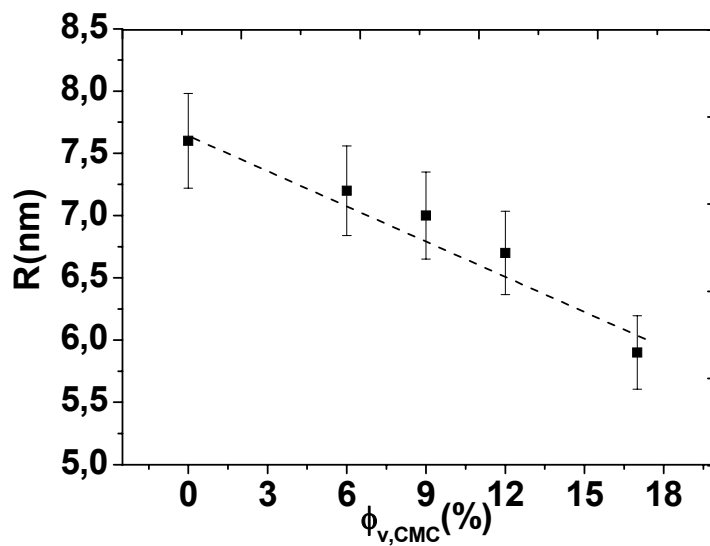


Figure 12. The mean hopping distance R, inversely proportional to the supplementary number of trapping centres (CMC bonds on carbon coating surface), as a function of the binder loading

The study of the conductivity at the cluster level is complementary. The effective value of the cluster conductivity is observed to decrease with the binder loading (or to increase with the C-LiFePO₄ volume fraction) as shown in Figures 13a and b. This is expected, as it is an effective value and accordingly (see Eq. 3.7 in Table 1) increases with the C-LFP volume fraction.

[131]. W. Porcher, B. Lestriez, S. Jouanneau, D. Guyomard, J. Electrochem. Soc., 156 (2009) A133.

[132]. R.A. Jones and R.W. Richards, Polymers at Surfaces and Interfaces, Cambridge University Press New York (1999).

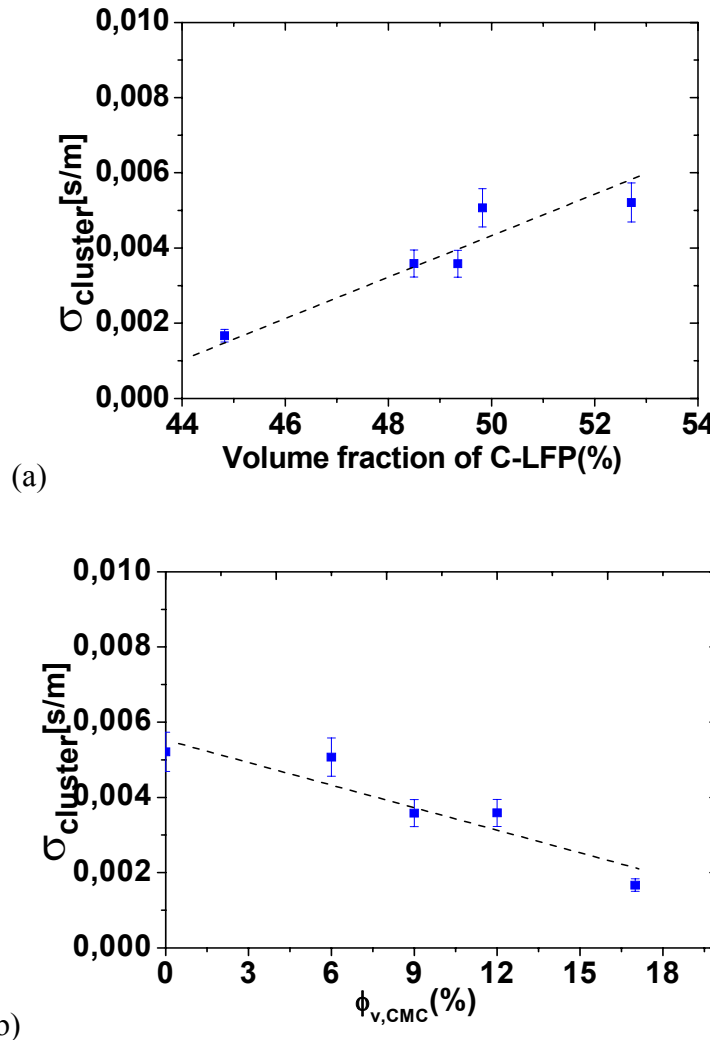


Figure 13. The evolution of the effective cluster conductivity (a) as a function of the volume fraction of the active material at RT and (b) as function of the binder loading).

However, for better understanding, again, we must look at the variation of the fundamental parameters σ_{0CLe} and E_{CL} . These parameters are calculated using the empirical Arrhenius relationship given by:

$$\sigma_{CLe} = \sigma_{0CLe} \exp\left(\frac{-E_{CL}}{kT}\right) \quad (3.10)$$

The activation energy of the cluster conductivity is seen to increase with the binder volume fraction (Figure 14). This is likely due to the additional potential barriers posed by the adsorbed CMC for electron hopping.

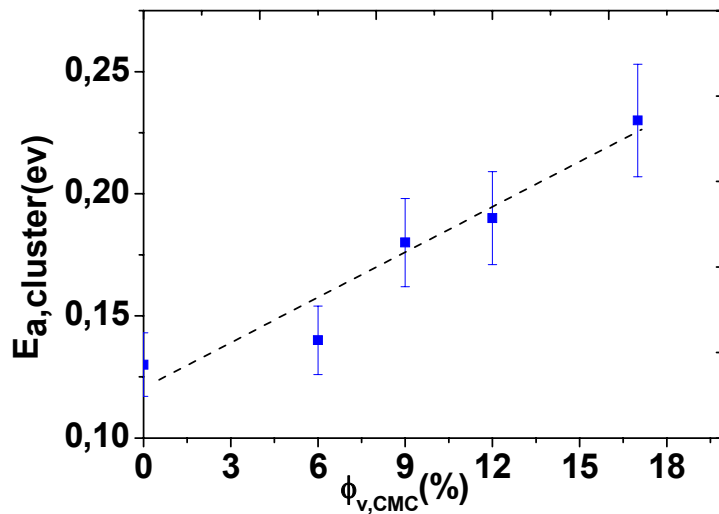


Figure 14. The activation energy for the charge transport in the clusters as function of the CMC loading.

In complement, Figure 15 describes the evolution of the pre-exponential factor $\sigma_{0,cluster}$ with the binder loading. The increasing evolution can most likely be related to the binder loading and the resulting interaction of CMC with amorphous carbon surface. As already discussed, this phenomenon increases the trapping sites at the surface which will increase the confined charges at the surface due to their inability to participate in the electron hopping and at the local and global scale. This will, therefore increase the $\sigma_{0,cluster}$ which is related to the surface electrostatic activity.

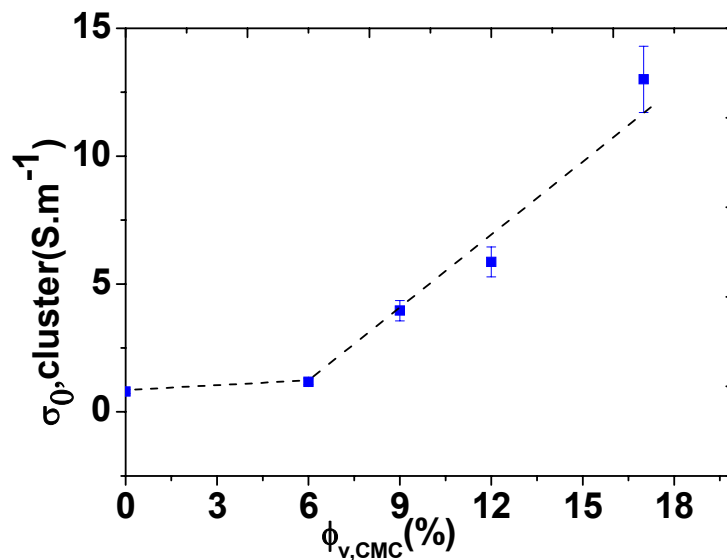


Figure 15. Cluster conductivity prefactor ($\sigma_{0,CLe}$) as function of the CMC loading.

Moreover, a direct relationship was observed between ν_{03} and σ_{0CLe} (Figure 16).

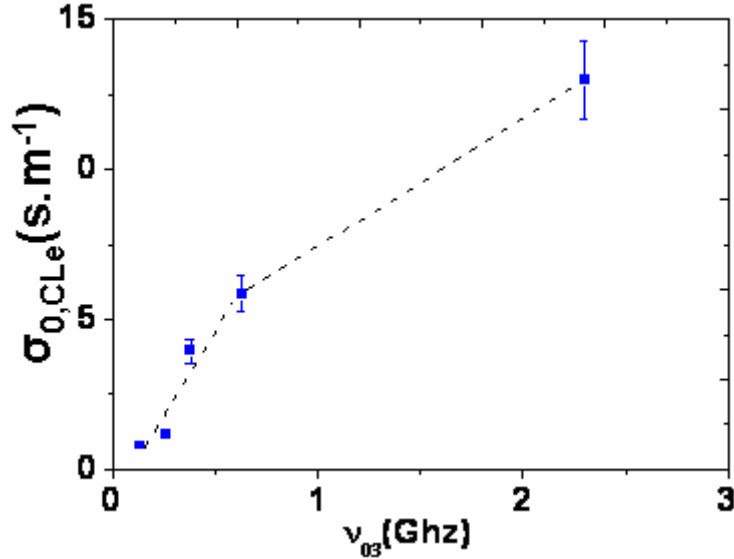


Figure 16. Cluster conductivity prefactor (σ_{0CLe}) as function of the relaxation frequency prefactor ($\nu_{0,3}$) corresponding to the relaxation domain D3.

Furthermore the plot of the Log ($R \times \sigma_0$) vs. R (Figure 17) demonstrates a linear evolution which means that the cluster conductivity prefactor can be given by the following expression:

$$\sigma_{0CLe} = \frac{A}{R} \nu_{ph} \exp(-2\alpha R) \quad (3.11)$$

where A is a constant. The expression (3.11) corresponds to the expression of the hopping conductivity prefactor given by N.F. Mott and E.A. Davies [133].

[133]. N.F. Mott and E.A. Davies, Electronic Processes in Non-Crystalline Materials (Clarendon, Oxford, 1971) Chap. 6.

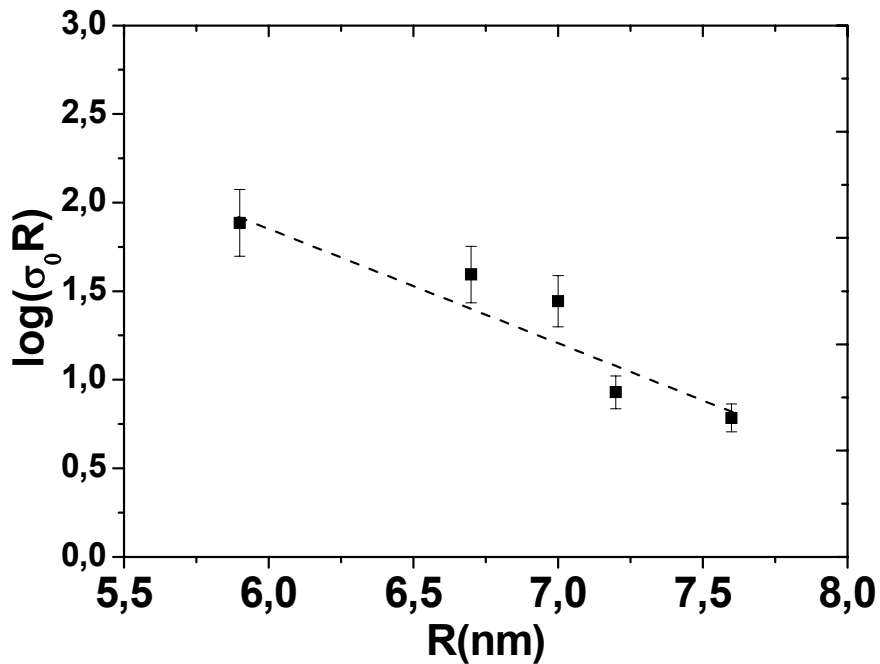


Figure 17. The evolution of $\text{Log} (R \times \sigma_0)$ with respect to the mean hopping distance R .

The slope of the straight line shown in Fig. 17 is thus equal to -2α . The result of the calculation gives the localization length $\alpha^{-1} = 1.2 \text{ nm}$.

2.6. Analysis of the binder effect on the inter-clusters contacts and samples conductivities

The next level of conductivity/resistivity to be discussed is the incremental resistivity $\Delta\rho_2$ in the complex resistivity plots. This value corresponds to the presumed averaged inter-cluster junctions resistivity in the sample. As expected, this value increases with the binder loading (Figure 18a).

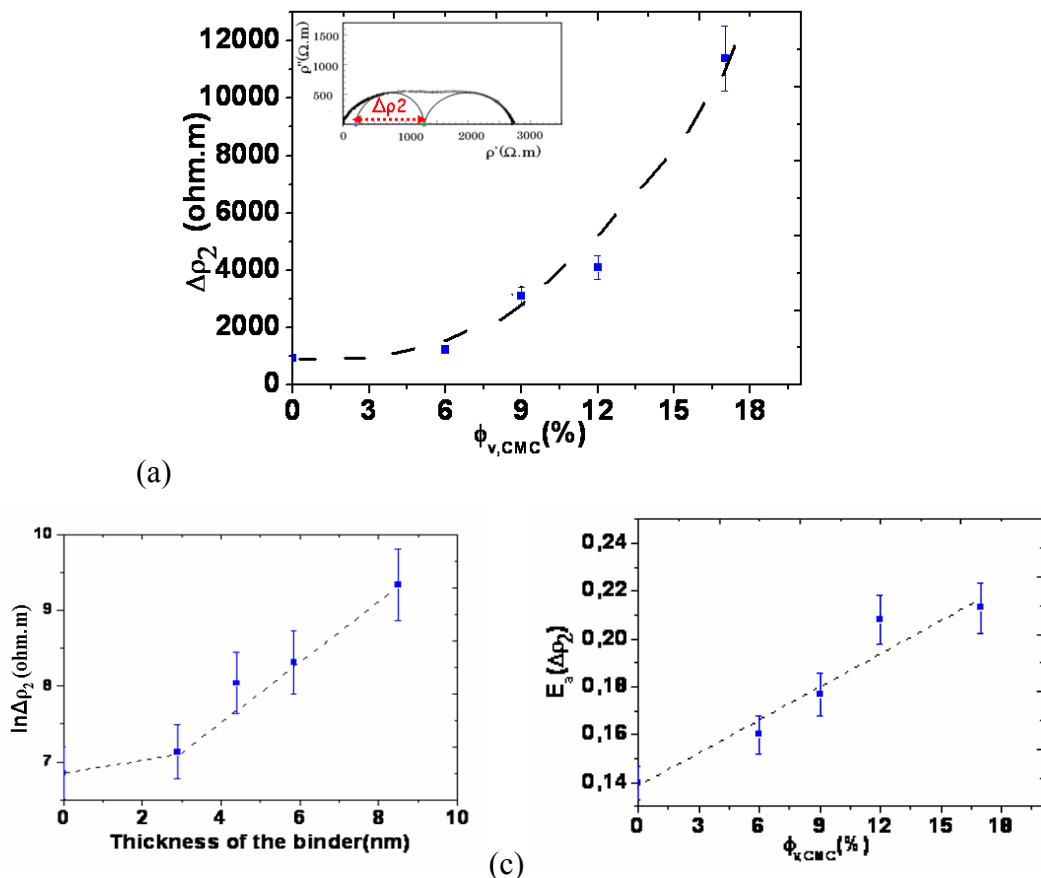


Figure 18. (a) The evolution of the incremental resistance ($\Delta\rho_2$) corresponding to the inter-cluster resistance as a function of the CMC loading at RT. In the complex resistivity plot (inset) the parameter ($\Delta\rho_2$) is indicated. (b) The quasi-exponential evolution of the resistivity corresponding to the inter-cluster contacts as function of the binder thickness. (c) The activation energy for this charge transport at the inter-cluster gap as function the CMC loading

This can be explained using the concept of “Conductivity bottlenecks” introduced in chapter 2. The increase in the amount of binder in between clusters adds an extra potential barrier for charge displacement (through tunnelling or hopping between the clusters) by increasing the effective inter-cluster distance (the thickness of the adsorbed binder layer

calculated assuming spherical particles and a uniform distribution of the CMC, is given in Table 2). It is also worth mentioning that the resistivity increases pseudo exponentially with the binder loading in agreement with the works of Guy et al (Figure 18b). [134] The increase in the adsorbed binder layer will in turn reduce the inter-cluster electron flux. Figure 18c shows the related activation energy for charge displacement through the inter-cluster gap. An increase in the activation energy with the CMC loading is demonstrated, owing to a larger gap.

Looking at the larger scale (i.e. macroscopic scale), the evolution of the sample conductivity as function of the CMC loading or the volume fraction of C-LFP is represented in Figure 19a and b. An increase in the sample conductivity σ_{sample} with an increase in volume fraction of the conducting component (carbon coated clusters) or drop in the CMC loading is evident. The explanation given in the case of inter-cluster contacts is also valid in this case as well. Thus the sample conductivity appears here to be principally governed by the inter-cluster contacts.

A likely exponential dependence of σ_{sample} with the theoretical thickness of adsorbed binder is seen in Figure 19c. The discrepancy observed in the 0-3wt% binder loading could be explained by a non-homogeneous coating of the particles by the binder.

[134]. D. Guy, B. Lestriez, R. Bouchet, D. Guyomard, J. Electrochem. Soc., 153 (2006) A679.

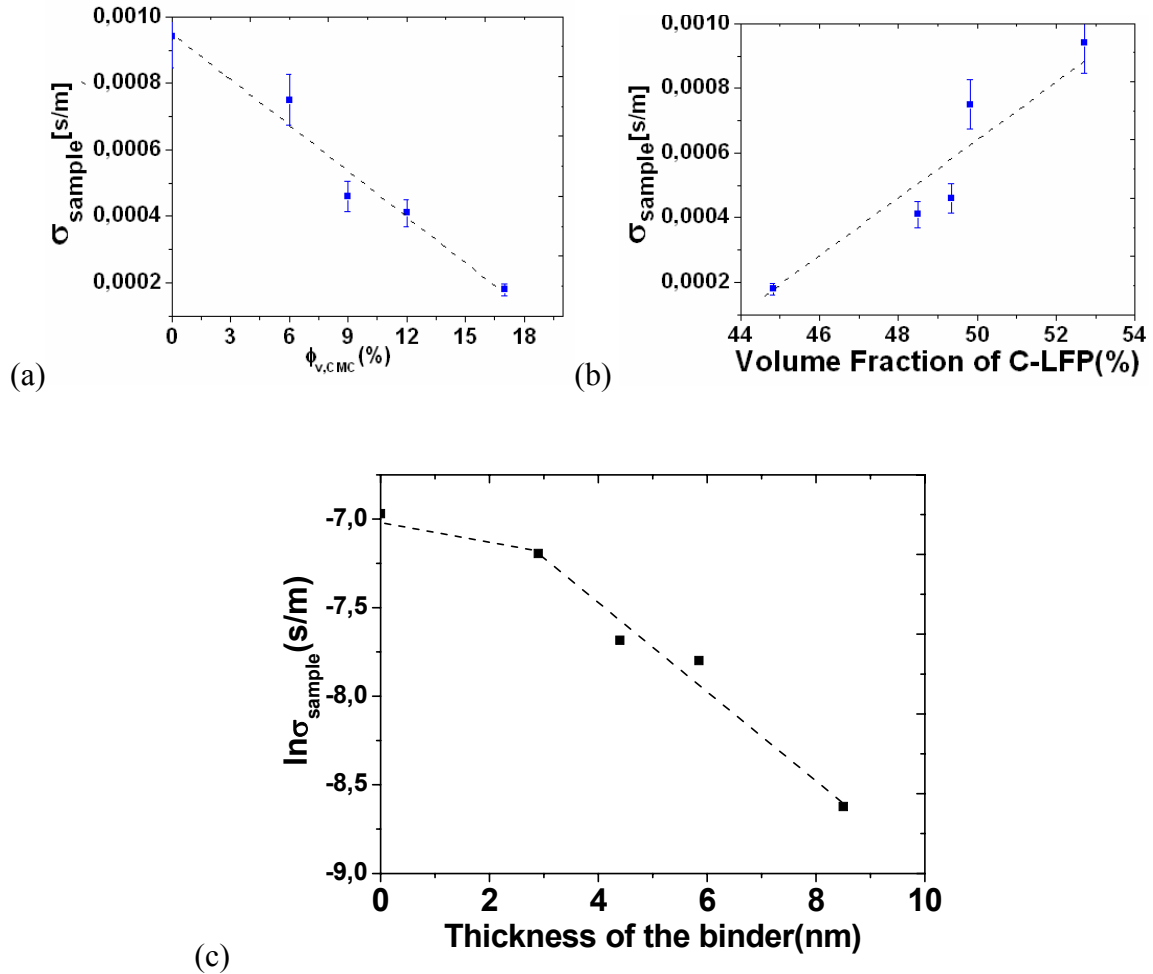


Figure 19. The evolution of the effective sample conductivity (a) as function of the binder loading and (b) as a function of the volume fraction of the active material at RT. (c) The quasi-exponential evolution of the sample conductivity as function of the binder thickness.

The activation energy related to charge displacement in the sample scale is also observed to increase from 0.14 to 0.25eV (Figure 20) in the range of composition C0-C15, as the result of an increase in the binder gap thickness.

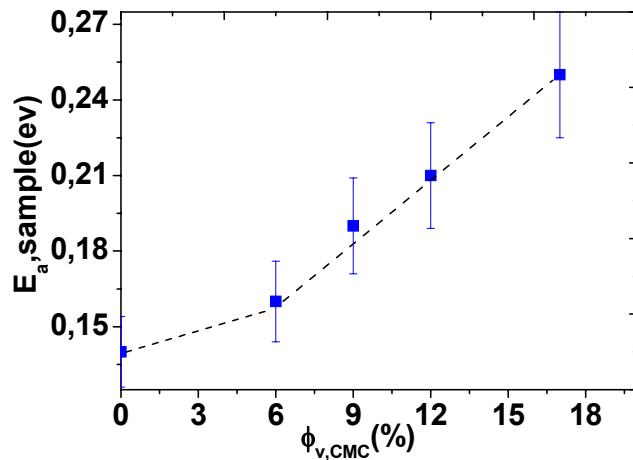


Figure 20. The evolution of the sample scale activation energy as a function of the CMC loading.

It has to be remembered that a parameter K_S which characterizes the conduction bottlenecks or inter-cluster contact qualities has been introduced in the second chapter (See Eq. 3.5 in Table 1 of this chapter). Again, we have applied the concept to probe the role of the binder in the electrodes considered. As the result, a parameter K_S is calculated for all the samples. Noting the prerequisite (postulate) we have established in chapter 2, the ratio of the sample and the effective cluster conductivity values will provide the parameter K_S . For this relationship to hold the activation energies for the two scales should be sufficiently similar (close), which is the case (see Table 3). Figure 21a indicates that the calculated values drop with an increase in binder loading.

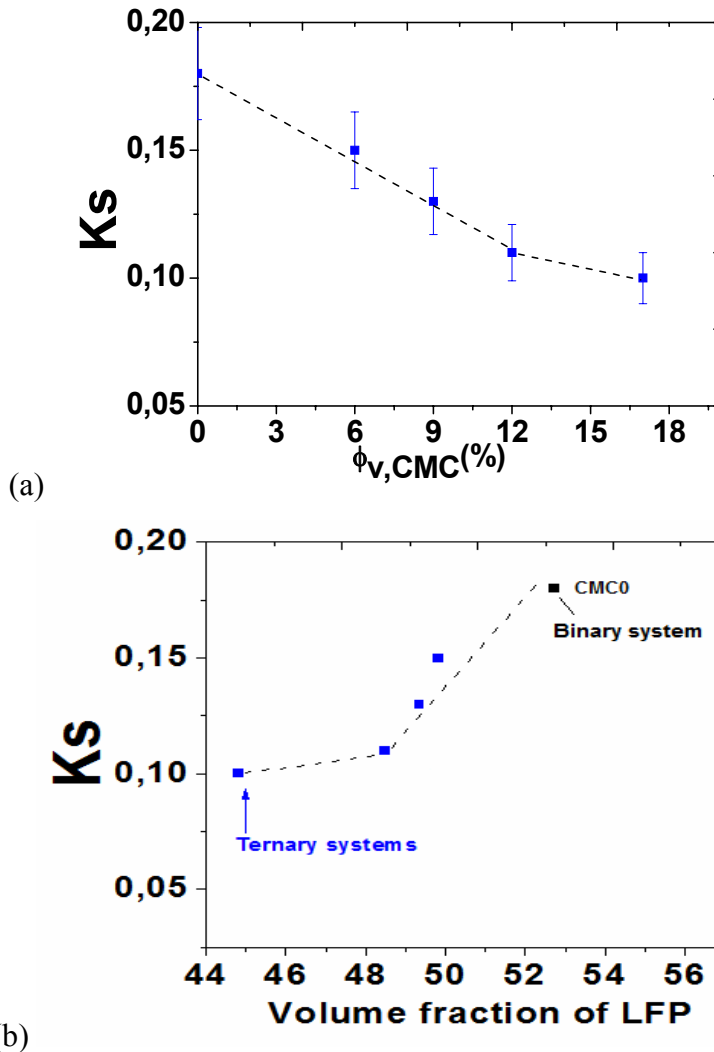


Figure 21. The parameter K_s (a) as a function of: (a) the CMC loading and (b) the volume fraction of the C-LFP for the binary (CMC0) and ternary samples.

It implies that the inter-cluster contacts deteriorate. This finding is in line with the previous assertions of the role of the binder in the sample and inter-cluster conductivity. However, it is worth mentioning that, the evolution of the values of the parameter K_s are not big given the range of CMC loading (17 % in volume) considered. On the other hand the comparison of the ternary and the binary systems is shown in figure 21b.

It is thus important to compare the two conductivity prefactors of the sample (σ_{0S}) and of the cluster (σ_{0Cl}). Figure 22 shows the sample conductivity prefactor σ_{0S} with respect to the cluster conductivity prefactor σ_{0Cl} .

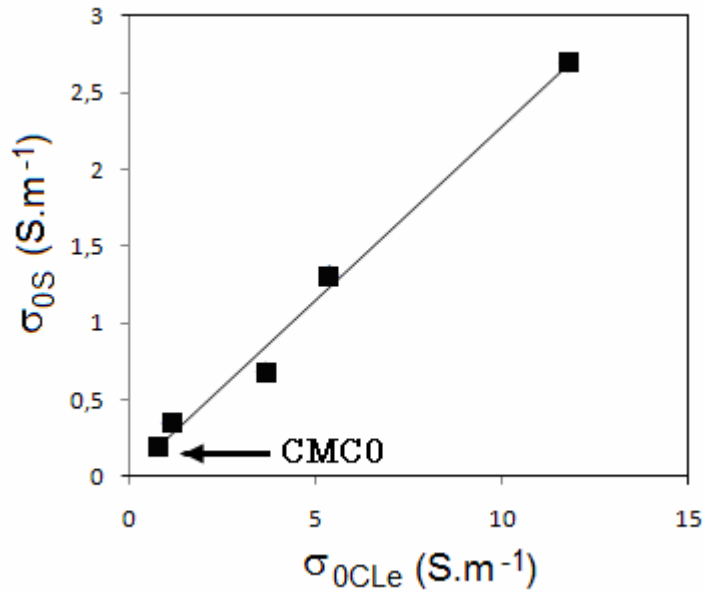


Figure 22. Sample conductivity prefactor σ_{0S} with respect to the cluster conductivity prefactor σ_{0CLe} for ternary and binary (CMC0) systems (ball milled powders)

The linear correlation between these two parameters is given by:

$$\sigma_{0S} \approx f\sigma_{0CLe} \quad (3.12)$$

The slope f of about 0.23 (i.e. between 1/5 and 1/4) is surprisingly independent of the binder. It would thus only depend on the connectivity of the clusters and thus on: a) the morphology of the clusters; b) cluster size distribution; c) compaction of the sample. To visualize the significance of f , it would be necessary to synthesize monodisperse powders constituted of spherical particles in order to determine its value as well as its relation with the particles coordination number. Nevertheless, coming back to Eq. 5 which relates σ_S to σ_{0CLe} , with Eq. 3.12 it comes

$$K_s = f \exp\left(-\frac{\Delta E}{kT}\right) \quad (3.13)$$

where $\Delta E = (E_S - E_{CL})$ is only dependent of the gap thickness w and generally increases with the binder loading (See Table 4). Overall, this equation is an important step in the development of a new technique to characterize the inter-cluster contacts and its role in the

sample conductivity. The role of the conductive additives, molecular junctions, densification as well as polymeric binders can possibly be monitored using the technique.

2.7. Analysis of the binder effect on the interface sample/current collector

Although extrinsic to the sample, the sample/current collector interface was briefly studied as this parameter is important in electrochemical application. Figure 23a shows the evolution of the incremental resistivity $\Delta\rho_1$ which corresponds to the resistance of the sample/current collector interface. The pseudo-exponential evolution of the parameters as a function of the CMC loading is observed, as expected due to the increase in the thickness of the binder layer at the surface of the C-LFP clusters. The activation energy for charge transfer at the interface is calculated for all the samples from the temperature dependence of conductivity data. The results presented in Figure 23b shows the expected rise of the activation energy with the binder loading. The activation energy associated with $\Delta\rho_1$ is higher (~0.05eV) than the one of $\Delta\rho_2$ (Figure 18c) due to the supplementary barrier at the interface.

On the other hand, the relaxation frequency D2 corresponds to the space charge accumulation in the same current collector interface. This is in a way dependent in the type and composition of the sample. Hence, the addition of binder is expected to affect the relaxation frequencies of this domain reducing the frequency significantly due to the addition of a more capacitive component in the porosity (increasing the relaxation width). This is evidenced in Figure 24a in which a drop in relaxation frequency is observed. This could largely be related to the increasing amount of binder at the interface. However at 18v% it looks like it stabilized most likely due to the saturation at the interface. Figure 24b on the other hand demonstrates the expected rise of the activation energy related to the relaxation at the sample/Ag interface (D2).

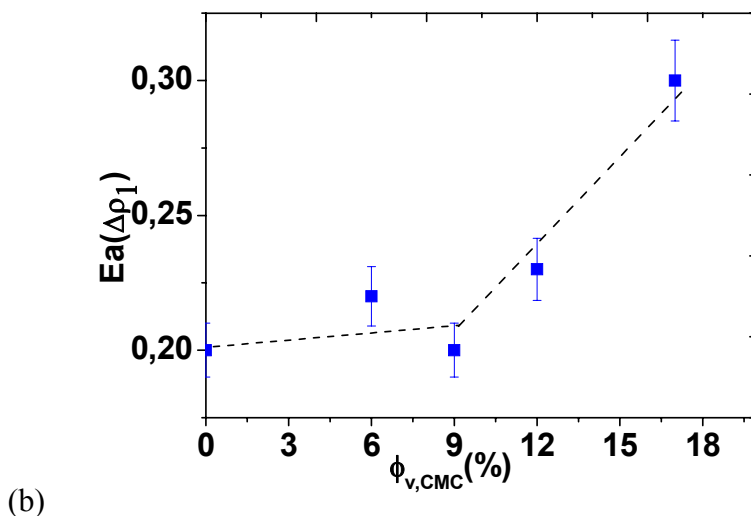
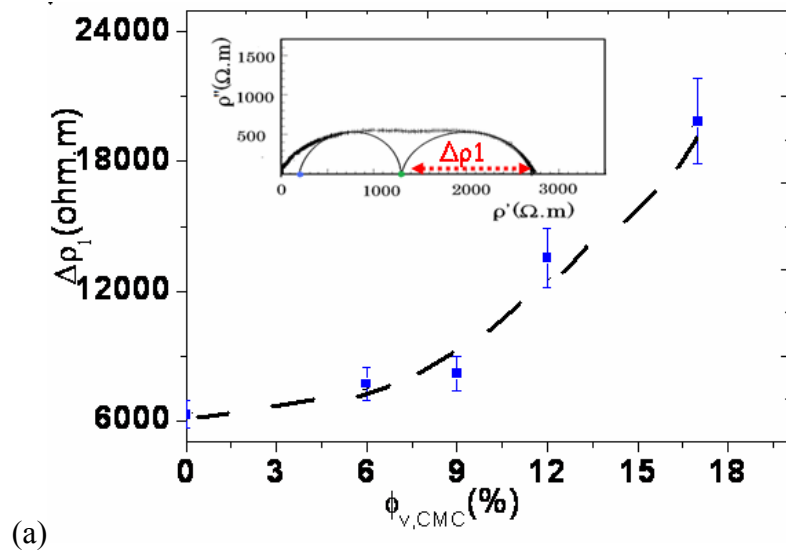


Figure 23.(a) The evolution of the incremental resistance ($\Delta\rho_1$) which corresponds to the interface resistance as a function of the CMC loading. In the complex permittivity plot (inserted) the parameter ($\Delta\rho_1$) is indicated.(b)the activation of $\Delta\rho_1$ as a function of the binder loading.

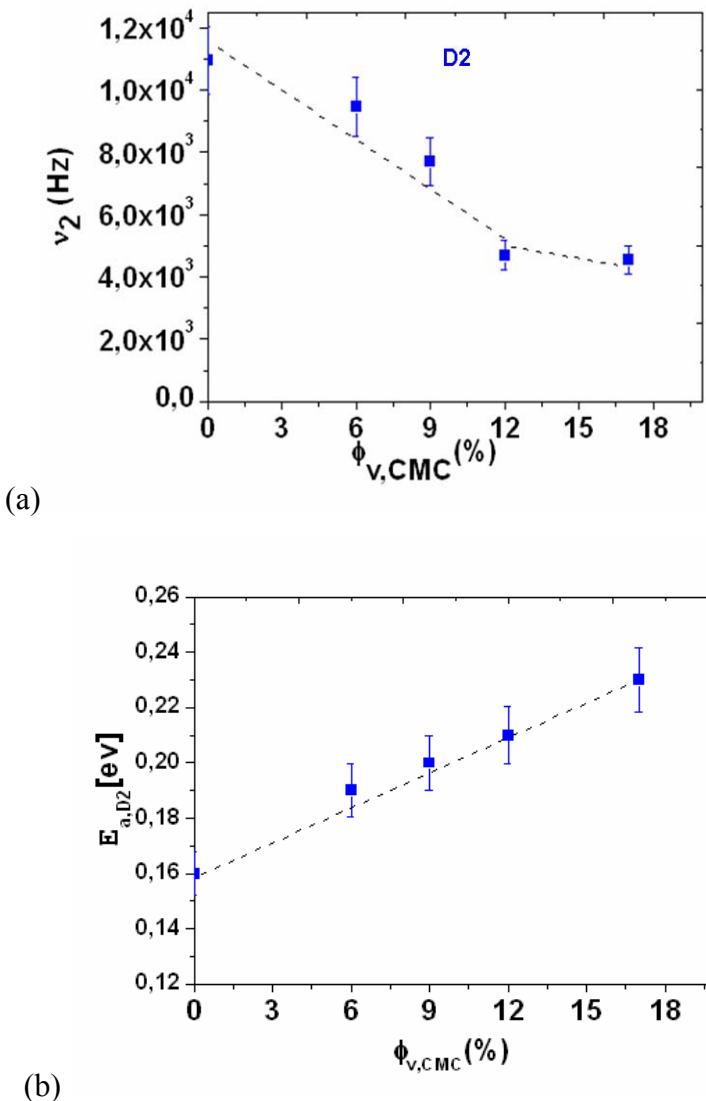
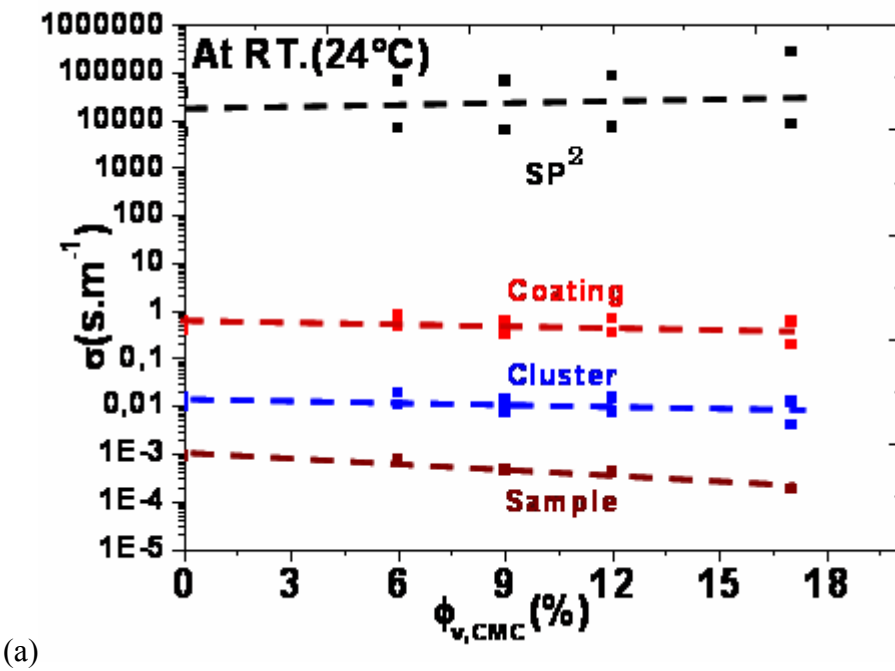


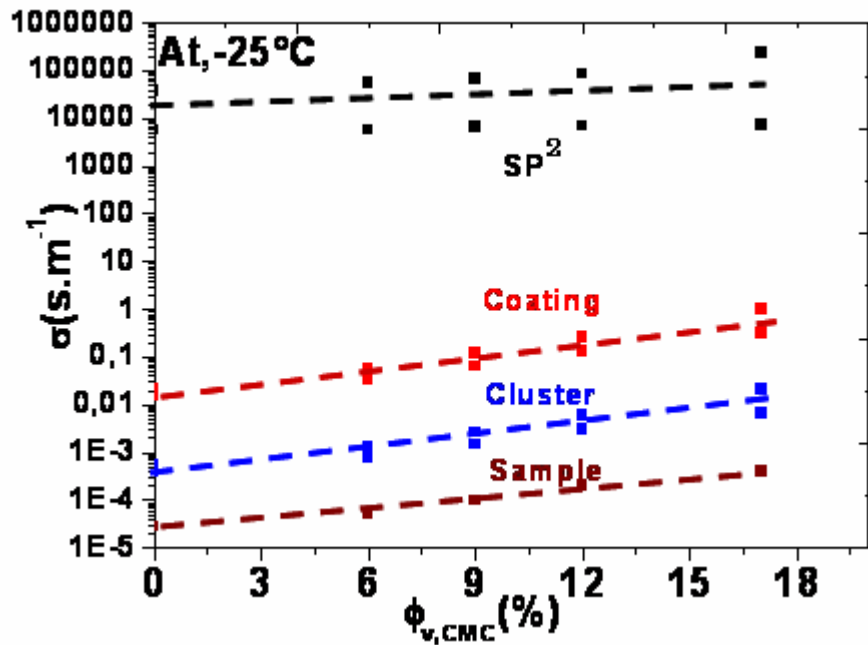
Figure 24. (a) The evolution of the relaxation frequency for the relaxation domain D2 with the binder loading at RT. (b) The evolution of the activation energy for the relaxation domain D2 with the binder loading.

2.8. The true conductivities at the different scales of the C-LiFePO₄/CMC composites

The absolute value of the sp², coating and cluster conductivities are calculated using appropriate relationships presented Table-1 (Eq. 3.6-3.8). The calculated lower and upper limit values at room temperature (24°C), and at -25°C for each composition, as well as the sample conductivities are presented in Figures 25a and 25b, respectively.



(a)



(b)

Figure 25. The evolution of the true or real conductivity (lower and upper limits) as a function of the binder loading, at all scales (a) at RT, (b) at -25°C.

All quantities are more or less independent of the binder loading at room temperature (24°C). However, a significant drop in the true conductivities of the scales other than the sp^2 domain is observed at -25°C compared to room temperature values. This is expected as the conductivity at this scales are thermally activated. With **a drop in** temperature the mobility of electrons decreases which will in turn affect the conductivities at the respective scales. This drop in conductivity might explain the poor electrochemical performance of C-LiFePO₄ lithium batteries at low temperatures.

It also looks like that there is an increase in true conductivities (coating, cluster and sample) with the binder loading at lower temperature. This increase would result from the decrease of the mean hopping distance R, which dominates the resulting increase in activation energy for an hopping at low temperature due to the increase in the binder loading.

3. Conclusion

Following the electrical measurements on the ternary systems we have discussed the electrical properties at the surface and interface level of the particles/clusters due to the interaction with the binder (CMC).

First of all, the existence of an interaction between the amorphous carbon coating surface and the CMC binder is demonstrated and explained. This interaction is shown to affect the electrical properties of the coating and the cluster scales. The establishment of (non-covalent) bonds between CMC and the carbon coating results in the decrease of the hopping distance and in the increase of the potential barrier for hopping. Using the values measured with BDS and the equation of Mott and Davies for hopping of electrons between localized sites, [102] we calculated a reasonable value of the hopping distance in the range of 5.5-8 nm.

We have also showed that, in comparison to the smaller scales, the binder significantly affects the larger scales like the sample and the interface. The pseudo-exponential drop of the conductivity at the sample which origins at the inter-clusters were found to be in agreement with reported works in which an exponential tunnelling law was proposed for $\text{Li}_{1+x}\text{V}_3\text{O}_8$ -based composite electrodes with a percolated network of carbon black/binder. [134]

The true conductivities were calculated. Decreasing the temperature from 25 to -25°C results in a large drop of conductivity that could explain the peculiar poor performance of C-LiFePO₄ at low temperature. Although adding the binder does not modify the true conductivity at room temperature, the interaction with CMC and the lowering of hopping distances results in a conductivity enhancement at low temperature.

Finally, combining Eq. 3.9 and 3.13 it is possible to propose a general equation

$$\sigma_s = f \exp\left(-\frac{E_s - E_{CL}}{kT}\right) \left(\frac{d - d_c}{1 - d_c}\right)^u \frac{2\phi_{cc}}{3} \sigma_{sp^2} \exp\left(-\frac{E_{CL}}{kT}\right) \quad (3.14)$$

detailling the dependence of the sample conductivity with E_{CL} the activation energy for hopping between sp² coordinated carbon atoms in the coating, σ_{sp^2} the true sp² domains conductivity, Φ_{cc} the coating volume fraction in the cluster, d the volume fraction of the clusters, d_c the percolation threshold ($0.10 < d_c < 0.40$ in 3D systems), u a critical exponent ($1.65 < u < 2$ in 3D Systems), $E_s - E_{CL}$ which is only dependent of the gap thickness w , and f which only depends on the connectivity of the clusters.

General Conclusion and perspectives

Lithium ion batteries are one of the most popular types of device for electrochemical storage toward the development of electrical transports and the use of renewable energies among many applications. New active materials, their smart formulation with additives to tailor more efficient composites, the development of new processes to design new electrode architecture are on going both in the industry and academia. The electronic conductivity of the composite electrodes is one of the most important properties with respect to the electrochemical performance. However, although lithium ion batteries have been commercialized more than 20 years ago, this property is still poorly understood, due to their complex multi-scaled architectures, lack of suitable measuring technique, and also maybe an insufficient multi-disciplinary approach.

In this work, we tried to bring a more fundamental understanding of this critical property, benefitting from brought together physicians of the LCMCP and LGEP (for the measurements and their interpretations), solid state chemists of UMICORE (for the synthesis of model materials), and material scientists of IMN (for the material characterizations and formulation know-how). To achieve our goal, we have also used an original but pertinent technique, the broadband dielectric spectroscopy (BDS), which is well-known for ionic conductors and polymers but much less used for electronic conductors. We have applied this technique to the study of nanocomposites prepared from the most important active material for lithium batteries, cluster of LiFePO₄ particles, coated in a core shell morphology with an amorphous carbon coating of few nanometers thick, formulated with an increasingly popular binder, carboxymethyl cellulose. Our objective was to extract the electronic conductivity of this nanocomposite at all the scales of its architecture (from inter atomic distances to macroscopic lengths), with the aim of identifying the limiting parameters and move on to systematic and rational manufacturing, Processing and engineering practices for the better.

The variation of the electronic conductivity at all scales of a LiFePO₄ composites as function of the particle size; quantity and quality of coating, binder loading and so on were studied. Binary systems (LiFePO₄ with its carbon coating) were studied first to establish the fundamental knowhow on the electrical properties of the different scales and the existing correlation between the scales of a compacted powder. Then ternary systems were studied (LiFePO₄/carbon coating/CMC binder) in which we explained the role of the binder and scales affected due to the introduction of the binder.

The results obtained in this work demonstrate that the BDS can distinguish the different types of electronic transfers involved in the different scales of the material architecture. These phenomena occur from interatomic to macroscopic sizes with the influence of the morphology of the different constituents at these scales. In summary, considering a composite material composed of an active material (e.g. LiFePO₄) and a conductive agent (e.g. carbon coating), when the frequency increases, different kinds of polarizations, giving rise to dielectric relaxations, appear in following order: a) Space-charge polarization (low-frequency range) due to the interface between the sample and the conductive metallic layer deposited on it; b) Polarization of C-LiFePO₄ clusters (micronic and/or submicronic scales) due to the existence of resistive junctions between them; c) Electron hopping between sp² domains (nanometric scale) within the carbon coating around the LiFePO₄ particles.

The conductivity and permittivity of the composites measured are effective parameters since they are functions of the relative concentration of the different phases. Using the Brick Layer Model and the General Effective Medium theory, it was possible to give some orders of magnitude for the true values of the conductivity at the different scales of the material, i.e. macroscopic, cluster, coating and sp² domain levels. Moreover, the true permittivity value of LiFePO₄ has been, for the first time, experimentally obtained and the values are in good agreements with expected ones.

We have thus established an empirical expression to describe the sample conductivity with respect to that of the smaller level (coherence length of sp² domains) that allows to identify and quantify all the limitations. The major drop in conductivity is due to the presence of sp³ discontinuities in the coating that result in a loss of ~10³ when going from the sp² domains to the coating scale. Although the carbon volume in the C-LiFePO₄ cluster is very low (less than 5v%), the loss is only a factor of ~10 when going from the coating to the cluster scale. Inter-cluster junctions result in another conductivity loss of ~10. The high activation energy for electrons transport associated with the sp³ discontinuities result in a

large decrease of the conductivity with decreasing temperature, which is a weakness of the C-LiFePO₄ material.

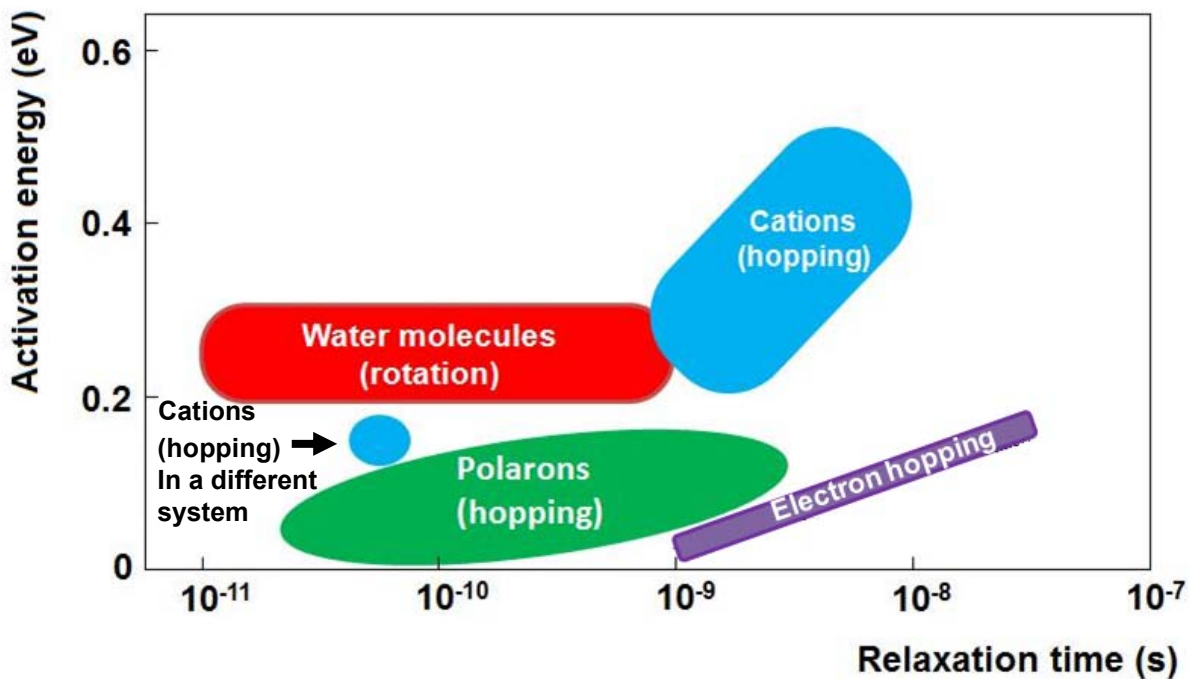
Furthermore, the ternary systems (LiFePO₄/carbon coating/binder) have been studied following the same procedure. The influence of the binder from the macro up to the nanoscales has been studied. At the macro scale, the binder is shown to affect the dc conductivity as expected and in agreement with previous work of Guy et al [Erreur ! Signet non défini]. The conductivity mechanisms at this scale are shown to follow a tunnelling/hopping law in which an exponential relationship between the conductivity and the polymer loading was observed. Moreover, the electrostatic interaction between the binder and the carbon coating was shown to induce new trapping centres for electrons at the cluster/coating surface. These new trapping centres reduce the hopping distance and this distance (a few nanometers) could be estimated. On another hand, the activation energy for hopping is increased by the electrostatic bonds between the binder and the carbon coating

From a broad fundamental view, several works [26,28,29,32,135,136,137] as well as this manuscript demonstrated the relationship between the relaxation frequency and the corresponding activation energy of different phenomena, as determined with the BDS. Figure 1 below summarizes the findings and demonstrates the sensitivity of the technique with respect to different processes.

[135]. S. Berthumeyrie, J.-C. Badot, J.-P. Pereira-Ramos, O. Dubrunfaut, S. Bach, and Ph. Vermaut, *J. Phys. Chem. C*, 114 (2010) 19803

[136]. J.C. Badot and N. Baffier, *J. Mater. Chem.*, 2 (1992) 1167

[137]. B. Rotenberg, A. Cadène, J.-F. Dufrêche, S. Durand-Vidal, J.-C. Badot, and P. Turq, *J. Phys. Chem. B*, 109 (2005) 15548



In summary, this work provided a new approach towards fundamental understanding of the electrical properties of composites for lithium ion batteries. It also gave a new perspective on the quantitative relationships existing between the different scales. These relationships offer the opportunity to pin point the limiting scales and conductivity mechanisms. Which in turn will be instrumental to make adjustments on the whole process of the electrode material synthesis, processing, manufacturing, engineering and so on for the objective of addressing the inherent conductivity problems in the studied material.

In the foreseeable future, making correlations of the findings with electrochemical properties is a top priority to assess the extent of validity. The study of the quaternary systems ($\text{LiFePO}_4/\text{carbon coating/conductive additives/binder}$) will also be a step forward in a complete understanding of the conductivity mechanisms involving all the components of a conventional lithium ion battery cathode. The role of molecular grafting on the conductivity of the systems will also be studied. Finally all this information would enable the interpretation of results that would be acquired using *operando* cell. The latter will enable the acquisition of electrochemical and BDS data at the same time. With all this in mind, the job that has been done is an important step in the right direction towards achieving a more comprehensive and reliable understanding of electrical properties in relation with the electrochemical performance of a cell.

Appendices

Appendix 1: Material characterizations

Additional techniques were utilized to characterize the as received materials. Some of the results which are not discussed in the main part of this manuscript are roughly summarized.

Characterisation techniques used:

- XPS
- XRD
- TEM

1. XPS (x-ray photoelectron spectroscopy)

XPS measurements have been performed to quantify the %sp² in coating of our samples. The table below summarizes the results obtained for the two different batches of materials received. Surprisingly a difference is observed for the samples in the two batches.

Table 1. XPS measurements results of the as received samples showing the %SP² of two different batches.

Sample	Batch °1 (%sp ²)	Batch °2 (%sp ²)
LFP	-----	-----
CLPF1	64	64
CLFP2	52	62
CLFP3	70	60

2. XRD

The stability of the sample with the ball milling step is verified using the XRD measurements. The superposition of the acquisition before and after BL of the powder in NMP is shown below, which shows no modification of the sample.

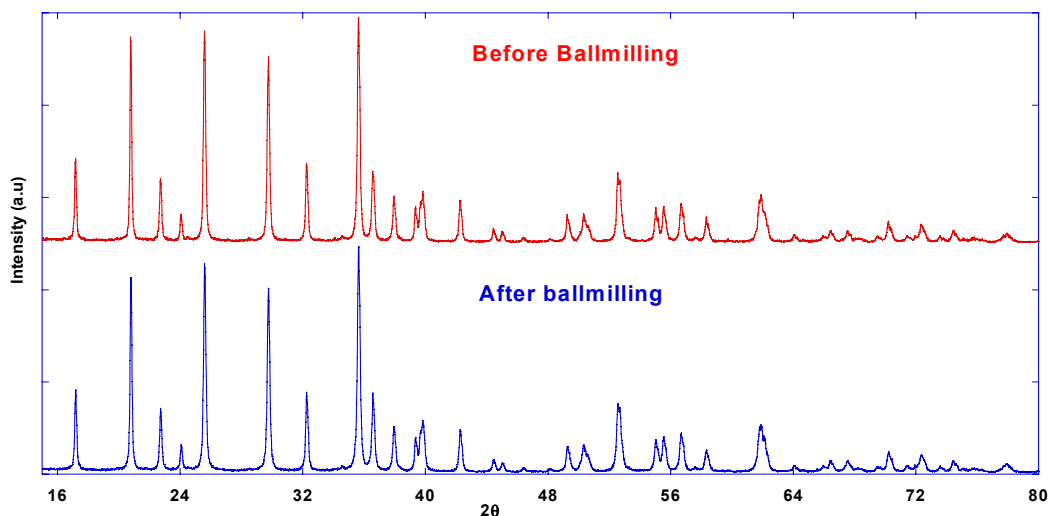


Figure 1. The x-ray diffraction (XRD) results before and after ball milling demonstrating structural stability of the sample up upon ball milling.

3. TEM (transmission electron microscopy)

TEM measurements carried out on the coated samples before and after ball milling showed varied results. Generally a slight compaction (densification) on the sample is observed upon ball milling. The table below summarizes the averaged value of the thickness before and after a ball milling.

Table 3. Average coating thickness of the different samples from TEM.

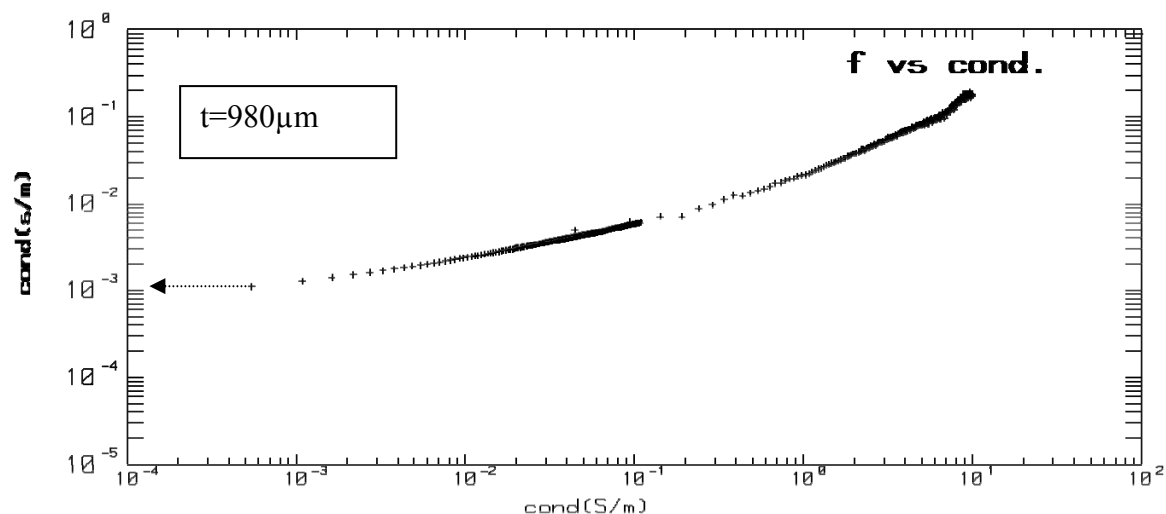
sample	Av.coating thickness (NBL) in nm	Av. coating thickness (BL) in nm
LFP	-	-
LFPC2	2.75	1.50
CLFP3	4.60	3.00
CLFP1	3.00	3.00

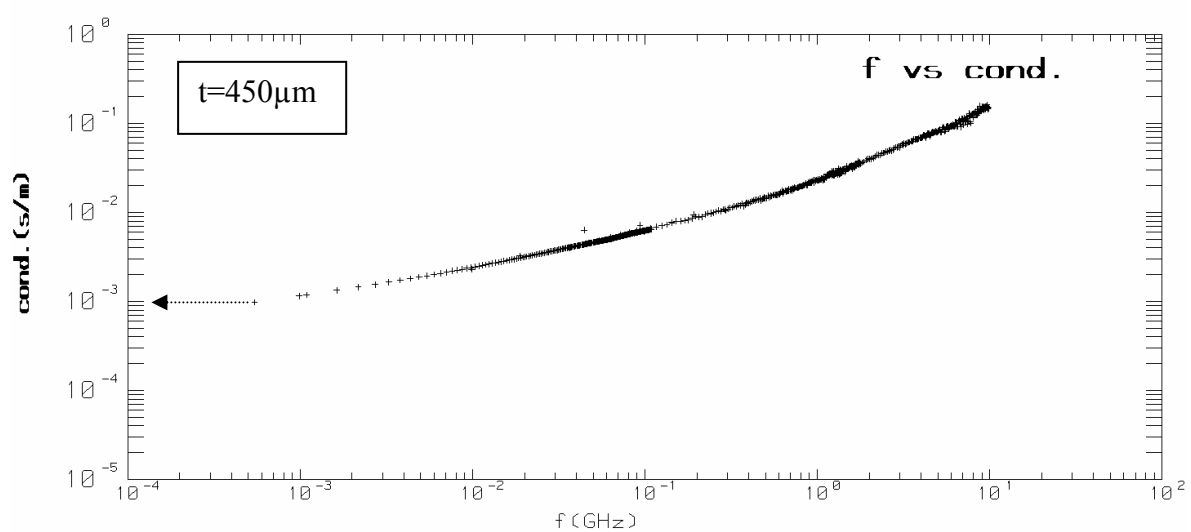
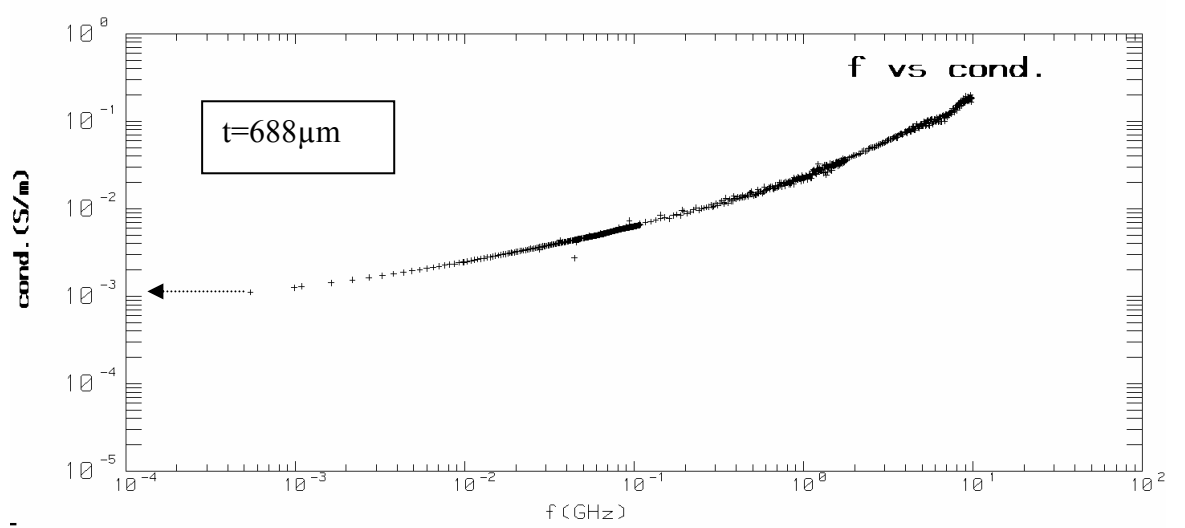
NBL*- non ballmilled sample BL* ballmilled sample

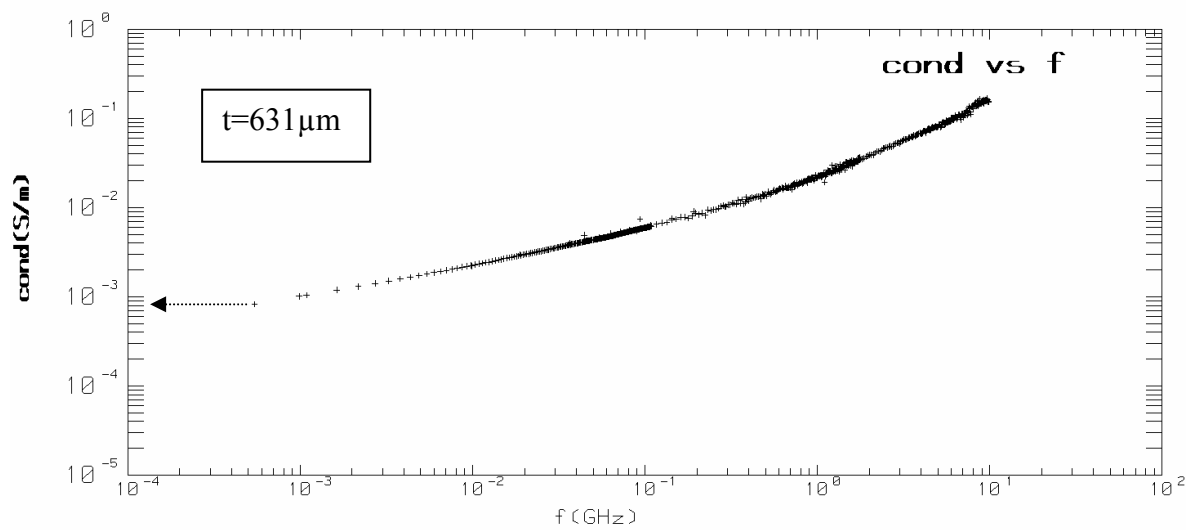
Appendix 2: Effect of the sample thickness on the reproducibility and measured parameters

Verification of the effect of thickness on the calculated permittivity and reproducibility of the measurements were carried out. Samples ranging in thickness from $400\mu\text{m}$ - $900\mu\text{m}$ were used for the purpose. The results found showed that there is little or no difference what so ever in the calculated conductivity as well as the reproducibility of measurements. The Figures below show the representative plot of the conductivity as a function of the frequency based on which comparisons are made for different thickness. The extracted conductivity for the various thicknesses is given in the table below. The standard deviation in the values of the conductivity is found to be 1.1×10^{-4} . These results should rule out any doubts about a significant possible influence of different thickness of samples in the measurements.

Figure 2. The frequency dependence of conductivity displaying the thickness independence of the response.







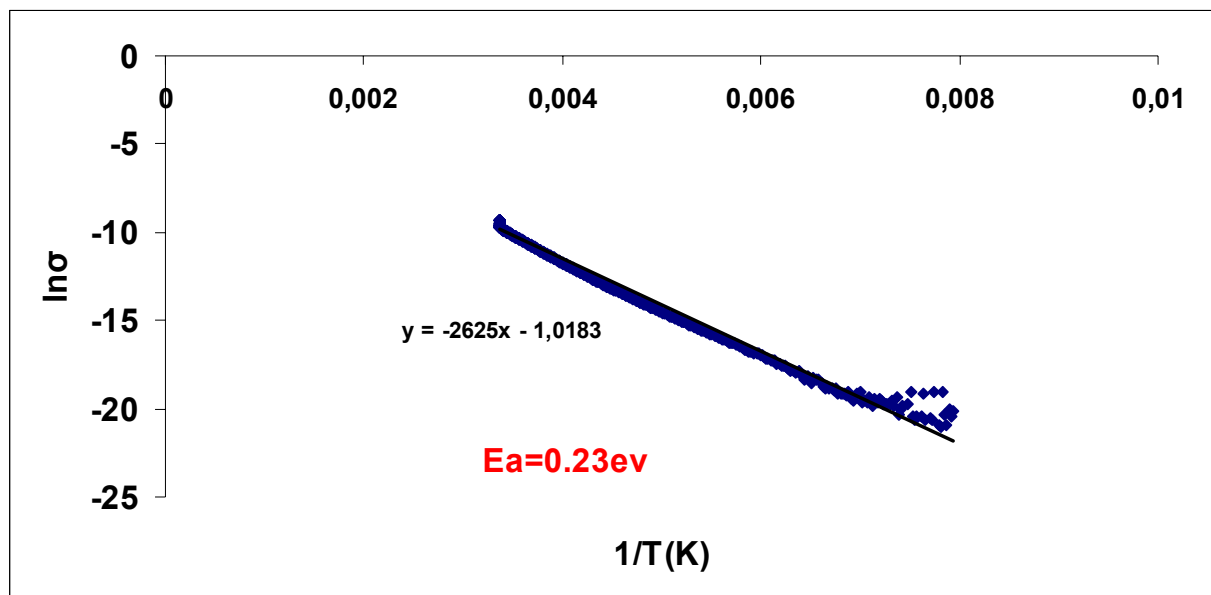
Samples	Cluster conductivity (S/m)
CLFP3-1	3.2×10^{-3}
CLFPP-2	3.0×10^{-3}
CLFPP-3	3.1×10^{-3}
CLFPP-4	3.3×10^{-3}

Appendix 3: DC conductivity measurements as a function of the temperature using a four probes technique.

DC measurement was also performed in a four probe set up. The results show a similar evolution of temperature dependence with conductivity. The result for the CLFP2 is shown below. Nearly similar activation energies were found with the four probes (0.23eV) and the BDS (0.19 eV, see Table 2 in 3) techniques.

Figure 3. (a)The temperature dependence of conductivity using the data from four probe DC measurements. (b) The corresponding image of the set up.

(a)



(b)



RESUME

Mécanisme de conductivité à plusieurs échelles dans les matériaux composites C-LiFePO₄ utilisés en batterie au lithium.

La spectroscopie diélectrique à large bande ou BDS ($40 - 10^{10}$ Hz) a permis de caractériser les propriétés électriques de nanocomposites utilisés comme électrodes de batteries au lithium. La BDS peut distinguer les différents mécanismes de transports électroniques aux différentes échelles du composite (distances interatomiques à dimensions macroscopiques) et révéler l'influence de sa morphologie. Ce composite est constitué de particules de LiFePO₄ enrobées d'une couche de carbone amorphe (nm), et agglomérées en clusters. Le liant polymère carboxymethylcellulose (CMC) entoure les clusters. Les échantillons, pressés sous forme de pastilles, sont mis dans un guide coaxial. Les échantillons sont couverts de laque d'argent afin de réaliser de bons contacts avec le guide coaxial. Quand la fréquence augmente, différentes polarisations apparaissent: i) polarisation de charge d'espace à l'interface entre l'échantillon et la laque d'argent; ii) polarisation des clusters de C-LiFePO₄; iii) sauts d'électrons entre les domaines graphitiques de carbone sp² dans la couche de C. Comme la conductivité et la permittivité mesurées sont des valeurs effectives dépendant des concentrations relatives des phases, le modèle '*brick-layer*' et la théorie générale des milieux effectifs ont été utilisés afin de calculer leurs vraies valeurs. Lorsque le CMC est ajouté, les propriétés électriques sont modifiées. L'adsorption du polymère à la surface des particules et l'établissement de liaisons électrostatiques avec la couche de C forment des pièges à électrons supplémentaires dans l'enrobage de C. La couche de CMC forme une barrière résistive qui accroît les résistances de contact entre les clusters.

Mots Clés: conductivité, résistivité, permittivité, diélectrique, carbone, électronique

ABSTRACT

Measurement of the electronic conductivity at all scales of the positive composite electrode of Lithium ion batteries

The broadband dielectric spectroscopy (BDS) ($40 - 10^{10}$ Hz) was used to characterize the electrical properties of nanocomposites used as an electrode in lithium batteries. The BDS can distinguish the different mechanisms of electronic transport at different scales of the composite, from the interatomic to the macroscopic dimensions. It also reveals the influence of morphology. The studied composites consist of grains of LiFePO₄ coated with a layer (nm) amorphous carbon, agglomerated into clusters. The polymer binder carboxymethyl cellulose (CMC) coats the clusters. For measurement, the sample is prepared in the form of a pellet (mm) thick. Contacts are made with a silver paint. With increasing frequency, different polarizations appear: i) space charge polarization at the interface between the sample and the silver paint ii) polarization of the clusters of C-LiFePO₄ iii) electron hopping between graphitic areas of sp² carbon in the layer of C. The Conductivity and permittivity are effective values that depend on relative concentrations of the phases, using the '*brick-layer*' model and the general effective medium theory, we calculated the true (real) values. When CMC is added, the electrical properties are changed. Adsorption of polymer on the surface of the grains and the establishment of electrostatic bonds with the carbon layer act as an additional charge traps in the carbon coating. At the point of contact between the clusters, the CMC layer forms a resistive barrier, which significantly increases the contact resistance between the clusters.

Key words: conductivity, resistivity, permittivity, dielectric, carbon, electronic